

Copyright
by
Jason F. Ventrella
2002

The Dissertation Committee for Jason F. Ventrella
certifies that this is the approved version of the following dissertation:

**A Numerical Treatment of Spin- $\frac{1}{2}$ Fields Coupled to
Gravity**

Committee:

Matthew William Choptuik, Supervisor

Philip J. Morrison, Supervisor

Rafael de la Llave

Willy Fischler

Richard Matzner

**A Numerical Treatment of Spin- $\frac{1}{2}$ Fields Coupled to
Gravity**

by

Jason F. Ventrella, B.S.

DISSERTATION

Presented to the Faculty of the Graduate School of
The University of Texas at Austin
in Partial Fulfillment
of the Requirements
for the Degree of

DOCTOR OF PHILOSOPHY

THE UNIVERSITY OF TEXAS AT AUSTIN

December 2002

To my family.

Acknowledgments

I thank my supervisor, Matthew Choptuik, for his help and guidance over the years. I would also like to thank him for making it possible for me to be a visiting student at the University of British Columbia.

I thank Philip J. Morrison for agreeing to be my co-supervisor and for taking time to answer my questions.

I thank everyone in the UBC and UT Austin numerical relativity groups for many helpful conversations over the years. I particularly would like to thank Luis Lehner who always took the time to answer my myriad questions. I have greatly benefitted from his patience and interest in my graduate career.

I sincerely thank my family and friends for always believing in me and for giving me so much support over the years.

I would like to acknowledge financial support from the National Science Foundation grant PHY9722068 and from a grant from the Natural Sciences and Engineering Research Council of Canada (NSERC). Much of the computations in this work were performed on the `vn.physics.ubc.ca` Beowulf cluster which was funded by the Canadian Foundation for Innovation, with operations support from NSERC and the Canadian Institute for Advanced Research.

A Numerical Treatment of Spin- $\frac{1}{2}$ Fields Coupled to Gravity

Publication No. _____

Jason F. Ventrella, Ph.D.

The University of Texas at Austin, 2002

Supervisors: Matthew William Choptuik
Philip J. Morrison

This dissertation presents the numerical solution and investigation of spin- $\frac{1}{2}$ fields coupled to gravity (Einstein-Dirac system). The primary focus is on the behavior at the threshold of black hole formation.

A spherically symmetric system of massive spin- $\frac{1}{2}$ fields in a singlet spinor state is studied and shown to exhibit both unstable and stable solutions. The unstable solutions correspond to the threshold between black hole collapse and dispersal. There are a continuum of stable solutions that are solitonic in nature. These tended to oscillate and approach the stable, static solutions that we found through independent techniques.

A spherically symmetric system is constructed from massless spin- $\frac{1}{2}$ fields by using spinor harmonics for their angular part and taking an incoherent sum of their individual stress tensors. The result is a spherically symmetric system with no net spin-angular momentum. Instead the system feels the effect of a “spin-angular momentum barrier.”

The strength of the barrier is controlled by the spin-angular momentum quantum number, l . The lowest value of $l = \frac{1}{2}$ corresponds to two counter-rotating shells. In this case, black hole formation occurs at infinitesimal mass (Type II). This new, continuously self-similar solution is found by solving the Einstein-massless-Dirac system of nonlinear partial differential equations. A self-similar ansatz is then taken which reduces the partial differential equations to a set of ordinary differential equations. These new equations are solved and the solution of the PDEs are shown to agree with the solution of the ODEs.

The Einstein-massless-Dirac system of PDEs is then solved for other values of l . As l is increased, the scaling exponent, λ of the Type II solutions is shown to decrease.

The final chapter describes a new two-dimensional, axisymmetric code which uses a combination of harmonic coordinates and Chebyshev pseudospectral collocation methods to solve Einstein's equations. This evolution code is a hybrid of finite-difference and spectral techniques— the temporal derivatives are approximated by finite-difference operators while the spatial derivatives are found using spectral methods. The constraint equations are solved using a purely spectral nonlinear elliptic solver which uses the Newton-Kantorovich method.

Table of Contents

Acknowledgments	v
Abstract	vi
List of Tables	xi
List of Figures	xii
Chapter 1. Introduction	1
1.1 Layout	3
1.2 Notation and Conventions	5
Chapter 2. Theoretical Background	7
2.1 Gravity as Curvature	7
2.1.1 Curvature	8
2.2 Solving Einstein's Equations	12
2.2.1 3 + 1 ADM Formulation	13
Chapter 3. Numerical Methods	19
3.1 Finite-Difference Methods	19
3.1.1 Stability	21
3.1.2 Truncation Error	24
3.2 Spectral Methods	27
3.2.1 Chebyshev Basis and Collocation Grid	28
3.2.2 Spatial Derivatives	29
3.2.2.1 Fast Fourier Transform	29
3.2.2.2 Finding Derivatives	30
3.2.3 Nonlinear Hyperbolic (or Parabolic) Equations	30
3.2.4 $2h$ Waves and Aliasing	32

3.2.5	Elliptic Equations	33
3.2.6	Spectral Methods in Higher Dimensions	36
Chapter 4.	Einstein-Dirac System	38
4.1	Introduction	38
4.1.1	Equations of Motion	39
4.1.1.1	The Dirac Operator	40
4.1.2	Initial conditions	45
4.1.2.1	Centered Gaussian	45
4.1.2.2	Propagating Gaussian	45
4.1.3	Boundary conditions	48
4.1.4	Static solutions	49
4.1.5	Code description	58
4.1.6	Code testing	58
4.2	Data and results	61
4.2.1	Moderate mass regime ($m = 0.534$)	61
4.2.2	Low mass regime ($m = 0.250$)	66
Chapter 5.	Einstein-Massless-Dirac System	68
5.1	Introduction	68
5.2	Formalism	70
5.2.1	Representation	72
5.2.2	Equations of Motion	74
5.2.3	Geometry	76
5.3	Numerics and Results	78
5.4	Self-Similar Ansatz	83
5.5	Shooting Method and Results	86
5.6	Comparisons of Solutions	88
5.7	Conclusions	92

Chapter 6. Einstein-Massless-Dirac System for any l	93
6.1 Introduction	93
6.1.1 Equations of Motion for any l	93
6.1.2 Geometry for any l	94
6.2 Numerics and Results	95
6.3 Conclusions	104
Chapter 7. Harmonic Coordinates and the Axisymmetric Einstein Equations	105
7.1 Harmonic Coordinates	105
7.2 Solving the System	107
Chapter 8. Conclusions	111
Appendix	113
Appendix A. Numerical Implementation	114
A.1 Computer implementation	114
A.1.1 Finite differences	114
Bibliography	119
Vita	122

List of Tables

3.1	Some of the many finite-difference expressions are summarized below.	22
3.2	The first few Chebyshev basis functions.	28
6.1	Results for various values of l	100

List of Figures

2.1	(Top) A vector is parallel transported around a circle and back to the original point, P , in flat, Euclidean geometry. It remains unchanged. (Bottom) a vector is parallel transported on the surface of a curved manifold (a 2-sphere) along a closed path back to the original point, P . It undergoes a rotation.	11
2.2	Diagram of the 3 + 1 decomposition of the spacetime manifold into spacelike hypersurfaces.	16
3.1	Diagram of Courant stability for an explicit finite-difference update scheme. The continuum equation being approximated has a characteristic structure represented by a shaded domain of dependence above. In the stable case (left) the time step, Δt , has been chosen such that the FD domain of dependence uncompasses that of the continuum system. In the unstable case (right) the time step, Δt , has been chosen to be too large which means that a portion of the continuum domain of dependence is excluded in the FD update. This exclusion results in an unstable evolution.	23
4.1	Three sample static solutions of the Einstein-Dirac field. . . .	53
4.2	Plot of the binding energy $ m - \omega$, showing spiral structures. This figure is reprinted from [12].	54
4.3	The two static solutions corresponding to $m = 0.534$. The solution shown in bold is a stable solution with $\omega = 0.503$, and is the same solution shown in Fig. 4.1. The other solution is unstable, with $\omega = 0.398$	55
4.4	This is a convergence test with the function, $d\hat{p}/dr$, the spatial derivative of the probability density. The system (with $m = 0.534$) is solved on a uniform grid at three different levels of discretization: $\Delta r = h, 2h$, and $4h$. The solid line is $4(d\hat{p}/dr _{2h} - d\hat{p}/dr _h)$ and the triangles show $d\hat{p}/dr _{4h} - d\hat{p}/dr _{2h}$. Our discrete solution converges to the continuum solution with $O(h^2)$ accuracy. We display the convergence test here at a single time.	60
4.5	A plot of the maximum value of $2M/r$ vs. time for a marginally subcritical evolution displaying Zitterbewegung.	63

4.6	Logarithmic scaling of the time to form a black hole near the critical parameter for $m = 0.534$. The slope of the fitted line is -4.8 ± 0.0007 (the quoted uncertainty only represents uncertainty in the linear fit).	65
4.7	Scaling behavior of the black hole mass near the critical parameter for $m = 0.25$. The slope of the fitted line is 0.27. This scaling of the mass is characteristic of Type II critical behavior.	67
5.1	Plot of the \ln of black hole mass vs. the \ln of $(p - p^*)$. The scaling exponent is $\lambda = 0.257$ (the third significant figure is uncertain) for the gaussian family. As one tunes arbitrarily close to the critical parameter, p^* , a black hole of arbitrarily small mass is formed indicative of a Type II critical solution. Note the absence of oscillations about the fit line which would be present if $a(t, r)$ were discretely self-similar.	82
5.2	Scale invariant quantities (functions of $x = -r/t$) reproducing themselves at smaller and smaller temporal and spatial scales (logarithmically) in accordance with continuous self-similarity.	83
5.3	The metric variable, $a(t, r)$, for a slightly supercritical evolution overlaid with the solution to the ODEs vs. $\ln(r)$. The frames are output logarithmically in central proper time. The function's peak reaches a value of approximately 1.6 and remains there as the solution continuously repeats itself on smaller and smaller scales.	89
5.4	The quantity $F_1(t, r)$ for a slightly supercritical evolution and the solution found from the ODEs vs. $\ln(r)$. The frames are output logarithmically in central proper time. The function oscillates and discretely repeats itself on smaller and smaller scales. A factor of $1/\sqrt{r}$ has been introduced to remove the scale dependence.	91
6.1	Plot of the \ln of black hole mass vs. the \ln of $(p - p^*)$ for $l = 1/2$, $l = 3/2$, and $l = 5/2$. The scaling exponents are $\lambda = 0.257$, 0.081, and 0.03, respectively. As one tunes arbitrarily close to the critical parameter, p^* , a black hole of arbitrarily small mass is formed indicative of a Type II critical solution. All of these solutions display continuous self-similarity. The y -intercepts have been adjusted so that all three lines can be plotted together.	97

6.2	Plot of the \ln of black hole mass scaling exponent, λ , vs. the spin-angular momentum quantum number l . We have used the half-odd integer values $l = 1/2, 3/2, 5/2$, and $11/2$. In addition to these, we have also used the <i>integer</i> values $l = 1$ and 2 . Although the spinor harmonics which are used for the angular parts of the spinors are only defined for half-odd integer values of l , there is no reason why the field equations cannot be solved for arbitrary values. A linear fit of the data yields a slope of -0.9 ± 0.008 (the uncertainty represents uncertainty in the linear fit). However, the results at this stage are too preliminary to draw any conclusions. The value of the scaling exponent does decrease as l is increased, but the precise functional relationship has yet to be determined.	99
6.3	A comparison of $2M/r$ for three slightly supercritical evolutions. From left to right the solutions correspond to $l = 7/2, 9/2$, and $11/2$. In each case, the solution begins an inward implosion which is delayed for a time by the spin-angular momentum barrier. Systems with higher l have a stronger barrier which increases the time of delay before collapse.	101
6.4	Plot of $2M/r$ for a slightly super-critical evolution with $l = 13/2$. The value of $2M/r$ persists at approximately 0.79 from $t = 33$ to $t = 220$ before ultimately collapsing towards black hole formation. The amplitude is not constant but oscillates about 0.79 at the order of 10^{-3}	102
6.5	Plot of the time to form a black hole vs. the \ln of $(p - p^*)$ for $l = 13/2$. The slope is -7.63 . As one tunes arbitrarily close to the critical parameter, p^* , it takes longer and longer to form a black hole.	103
7.1	A plot of the natural log of the l_2 -norm of the difference of the pre-iterate and post-iterate values vs. the iteration number for the pseudospectral constraint solver.	109

Chapter 1

Introduction

The classical theory of general relativity was formulated by Albert Einstein in 1915. Up to this time, gravity was believed to be a force that acted at a distance. It was believed to have an infinite speed of propagation. One of the most striking features of the general theory of relativity is that it combines the two seemingly separate concepts of space and time into one: *spacetime*. Gravity is a result of the curvature of spacetime. This makes gravity a local phenomenon which is described by the geometry of the spacetime manifold. Einstein's equations (2.1) relate the curvature of spacetime to mass-energy. For a dynamical solution, each of these affects the other: the manifold curves in response to mass-energy while the evolution of the mass-energy changes in response to the new geometry through which it moves. Dynamical solutions are of particular interest since they are especially challenging to find. They involve complicated systems of nonlinear partial differential equations which, in general, must be solved numerically.

One of the most interesting conjectures in the theory of general relativity is that mass-energy can gravitationally collapse to form a black hole. The black hole is a region of such an incredibly strong spacetime curvature that not even light can escape. It is said to be causally disconnected from the rest of the universe. These objects are interesting but perhaps even more fascinating is the dynamic study of their formation, a particular aspect of which is the

investigation of the very *threshold* of black hole formation. The interesting behavior at this threshold was first discovered by Choptuik [8]. The question being investigated was: “Does a black hole form at finite mass (Type I behavior) or can the smallest black hole formed be of arbitrarily small mass (Type II behavior)?” The original model used to investigate this question was a spherically symmetric, massless scalar field minimally coupled to gravity. Initial data consisting of a pulse of scalar field was parameterized by a single quantity, p . This parameter could represent the amplitude of the pulse, its width, or even its distance to the origin (this pulse was typically a gaussian function of the radius, r , which in spherical symmetry represents an entire spherical shell of scalar field). The parameter p controlled the initial amount of mass-energy in the spacetime. For simplicity, we will define p so that increasing it means increasing the initial amount of mass-energy. When p is sufficiently increased the evolution results in the formation of a black hole. The control parameter can also be given a lower value that causes the scalar field to evolve to some other end state which is not a black hole. This other scenario could be a static solution, an oscillating solution, or in the case of the massless scalar field, the pulse could simply disperse to spatial infinity leaving behind flat spacetime. When a value of the parameter is found which results in black hole formation we say that it is *supercritical*. When a value is found which does not produce a black hole (but produces the other end state) it is called *subcritical*. The parameter p is then tuned until its critical value p^* is found. This critical value is such that a small positive perturbation will result in gravitational collapse while a small negative perturbation will result in the other end state. In probing the threshold of black hole formation Choptuik found that there is a power law scaling for masses of the black holes formed. Tuning arbitrarily close to p^* means that black holes of arbitrarily small mass could be created. Another

feature of these threshold solutions is that the scaling exponent for this power law was universal. The same exponent was found regardless of the family of initial data or which parameter was used. This surprising result can be explained through perturbation analysis in which the critical solution is shown to have a single unstable mode. The two competing end states (black hole formation or not) are the end points resulting from the evolution of this one unstable mode [16]. Therefore by “tuning away” this mode one is left with the critical solution. When p is tuned arbitrarily close to the critical parameter, p^* , the critical solution will persist for an arbitrarily long time. All of this interesting behavior falls under the classification of *critical phenomena*.

1.1 Layout

The primary focus of this thesis will be the study of critical phenomena at the threshold of black hole formation for spin- $\frac{1}{2}$ fields coupled to gravity in spherical symmetry. We diverge from this topic in Chapter 7 when we discuss preliminary work on a two-dimensional, axisymmetric code to solve Einstein’s equations in harmonic coordinates.

The layout of this thesis is as follows: There will be a brief introduction to general relativity in Chapter 2 as well as a discussion of the 3+1 ADM formulation of Einstein’s equations. Chapter 3 is a brief discussion of numerical techniques including the finite-difference method of solving differential equations. The stability of evolution equations, the use of dissipation operators, and truncation error will also be discussed. A section is included on Chebyshev pseudospectral collocation methods since they are in the two-dimensional, axisymmetric code in Chapter 7.

The massive Einstein-Dirac system is investigated in Chapter 4. Here

the formalism for the curved space Dirac equation is not discussed in much detail, but is merely presented following previous work by Finster, et al [12]. A much more detailed (and canonical) treatment is given in Chapter 5 when the massless case is derived from first principles. There are a number of solutions in the massive case but these are not presented in full detail. The solution of interest is the Type II critical solution. This solution provides motivation for the massless investigation in subsequent chapters.

In Chapter 5 we give a detailed study of the Einstein-massless-Dirac system. A technique for solving the system of partial differential equations is presented and a Type II critical solution is constructed. A self-similar ansatz is then taken which reduces the nonlinear partial differential equations to a set of ordinary differential equations. These new equations are solved and the self-similar ansatz is shown to agree with the solution generated from the PDEs.

The method used to derive the Einstein-massless-Dirac system in Chapter 5 leads to an investigation of a model in which the strength of the “spin-angular momentum barrier” can be increased. This is discussed in Chapter 6.

In Chapter 7, an introduction to harmonic coordinates is given and the reduced Einstein’s equations in such coordinates are derived. A description is given of a new two-dimensional, axisymmetric code which uses a combination of harmonic coordinates and Chebyshev pseudospectral collocation methods to solve Einstein’s equations with a scalar field as the matter source. The evolution code is a hybrid of finite-difference and spectral techniques— the temporal derivatives are approximated by finite-difference operators while the spatial derivatives are found using spectral methods. The constraint equations are solved using a purely spectral nonlinear elliptic solver which uses the

Newton-Kantorovich method. This work is very preliminary and the current state is discussed as well as the future plans.

1.2 Notation and Conventions

The following notation and conventions are used in this work:

- Although spin- $\frac{1}{2}$ fields are studied in this work, the MTW [7] convention is, for the most part, used for the signature of the spacetime metric: $(-, +, +, +)$. A different signature is used in Chapter 4.
- Units are such that $G = c = \hbar = 1$.
- Greek letters are used for *spacetime* indices and run from 0 to 3.
- The Latin alphabet is used for *spatial* indices and run from 1 to 3.
- The Einstein summation convention is used for repeated indices in both cases. $A^\mu B_\mu = A^0 B_0 + A^1 B_1 + A^2 B_2 + A^3 B_3$.
- The totally symmetric parts of tensors are written as $T_{(\mu\nu)} = \frac{1}{2} (T_{\mu\nu} + T_{\nu\mu})$.
- The totally antisymmetric parts tensors are written as $T_{[\mu\nu]} = \frac{1}{2} (T_{\mu\nu} - T_{\nu\mu})$.
- Partial derivatives are denoted,

$$\partial_\mu \equiv \frac{\partial}{\partial x^\mu}.$$

- The covariant derivative is denoted, ∇_μ , and is compatible with the spacetime metric. It is sometimes written as a semi-colon on an index: $\nabla_\mu T_\nu \equiv T_{\nu;\mu}$.

- The spinor covariant derivative is also represented by ∇_μ but it will be clear which derivative operator is being used by whether or not it is operating on a quantity with spin.
- Spinor affine connections are written as Γ_μ .
- γ^μ are the curved space gamma matrices while $\tilde{\gamma}^\mu$ are the flatspace Cartesian gamma matrices.
- The order of accuracy will be shown with: $O(h^2)$.
- GR: General Relativity.
- PDE: Partial Differential Equation.
- ODE: Ordinary Differential Equation.
- FD: Finite Difference.
- CN: Crank-Nicholson.
- CFL: Courant-Friedrichs-Lewy.
- PSC: PseudoSpectral Collocation.
- FFT: Fast Fourier Transform.

Chapter 2

Theoretical Background

2.1 Gravity as Curvature

In our everyday lives we seem to perceive space and time as separate entities. However in the general theory of relativity, (GR), they are actually part of the same thing: *spacetime*. This can be thought of as a 4-dimensional Lorentzian manifold, and its curvature produces what we call gravitational effects. This is very different from the Newtonian theory which treats gravity as a force emanating from massive objects at infinite speed. In that theory, gravity is a force which acts instantaneously and at a distance from a center of attraction. This idea of curvature is one of the defining characteristics of GR. It is significant because it means that gravity is a local phenomenon. In other words, the Earth orbits the Sun because the mass-energy of the Sun has produced a curvature in the geometry of spacetime and the path which the Earth follows is the result of it travelling through the curved manifold. Thus the path of the Earth is determined by the region of the curved manifold through which it is currently passing. It is essentially in free fall and its path is a “straight line” in this geometry.

Thus, in order to study gravity, we need a way to describe the spacetime manifold’s geometry and calculate its curvature. This is the realm of differential geometry and it leads us to define a metric tensor on our manifold. In a coordinate system, the components of the metric, $g_{\mu\nu}$, can be viewed as a

4×4 symmetric matrix. Although we are now unifying the concepts of space and time, we still treat time as somewhat different from space. Therefore our metric will have a Lorentzian signature, $(-, +, +, +)$.

The heart of GR is Einstein's equations,

$$G_{\mu\nu} = 8\pi T_{\mu\nu}, \tag{2.1}$$

which relate the curvature of the spacetime geometry (represented here as the Einstein tensor, $G_{\mu\nu}$) to the distribution of mass-energy (stress-energy tensor, $T_{\mu\nu}$). Note that the plural equation(s) is used since (2.1) is a set of 10 equations. Both tensors are taken to be symmetric.

At this point, the necessity for Einstein's equations hasn't been shown. Neither has a need for a geometric interpretation of gravity. Such motivations can be found in any book on GR [26], [7]. We will assume all of this and merely show: how to find curvature, how this relates to the metric, and how this is related to mass-energy through Einstein's equations. So far, all we have is a basic summary of the theory: a Lorentzian metric and Einstein's equations. Now let us see how it all fits together.

2.1.1 Curvature

The local description of gravity discussed above requires a curved manifold to describe spacetime. The difficulty with a curved geometry is that most of our intuition is based on flat, Euclidean geometry. When things are flat, a vector at any point in spacetime can be compared to a vector at any other point. When the geometry is curved, we no longer have this luxury. If we compare two vectors by parallel transporting (see [26]) the first one to the position of the second we find that the result is completely dependent on the

path which was taken. This can be easily verified by using the equation of parallel transport,

$$t^\mu \nabla_\mu v^\nu = 0, \quad (2.2)$$

where t^μ is the tangent vector to the path and v^ν is the vector being transported. The derivative operator in (2.2) is defined as:

$$\nabla_\mu v^\nu = \partial_\mu v^\nu + \Gamma^\nu_{\mu\sigma} v^\sigma \quad (2.3)$$

with $\Gamma^\nu_{\mu\sigma}$ the connection coefficients. As frustrating as this path dependent change in vectors is, it is something that must be accepted. We can, however, ensure that the length of the vector remains unchanged under parallel transport. To do this, we need to define a derivative operator which is compatible with the metric

$$\nabla_\lambda g_{\mu\nu} = 0. \quad (2.4)$$

This yields the *Christoffel* connection, defined to be

$$\Gamma^\nu_{\mu\sigma} = \frac{1}{2} g^{\nu\lambda} (\partial_\mu g_{\sigma\lambda} + \partial_\sigma g_{\lambda\mu} - \partial_\lambda g_{\mu\sigma}) \quad (2.5)$$

for a coordinate basis. Note that this does *not* obey the tensor transformation law for a change in coordinates:

$$T^\sigma_{\mu\nu} = \frac{\partial x^\sigma}{\partial \tilde{x}^\alpha} \frac{\partial \tilde{x}^\beta}{\partial x^\mu} \frac{\partial \tilde{x}^\lambda}{\partial x^\nu} \tilde{T}^\alpha_{\beta\lambda}. \quad (2.6)$$

Indices of tensors and even non-tensors are lowered and raised with the metric and the inverse metric, $g^{\lambda\sigma}$, respectively.

$$T_{\sigma\mu\nu} = g_{\sigma\lambda} T^\lambda_{\mu\nu}$$

$$T^\lambda_{\mu\nu} = g^{\sigma\lambda} T_{\sigma\mu\nu}$$

Where

$$g^{\sigma\lambda}g_{\sigma\nu} = \delta^{\sigma}_{\nu}$$

and δ^{σ}_{ν} is the Kronecker delta.

Now that we have defined a covariant derivative, we are ready to define what we mean by curvature. Let us parallel transport a vector according to equation (2.2) along a closed path back to its original position P . If the manifold is curved, then the vector will undergo a rotation (see Fig. 2.1).

The amount that the vector has changed will be a measure of the curvature at point P . This leads to the definition of the Riemann curvature tensor:

$$R_{\mu\nu\sigma}{}^{\lambda}\omega_{\lambda} = (\nabla_{\mu}\nabla_{\nu} - \nabla_{\nu}\nabla_{\mu})\omega_{\sigma}. \quad (2.7)$$

In terms of the Christoffel symbols we have:

$$R_{\mu\nu\sigma}{}^{\lambda} = \partial_{\nu}\Gamma^{\lambda}_{\mu\sigma} - \partial_{\mu}\Gamma^{\lambda}_{\nu\sigma} + \Gamma^{\alpha}_{\mu\sigma}\Gamma^{\lambda}_{\alpha\nu} - \Gamma^{\alpha}_{\nu\sigma}\Gamma^{\lambda}_{\alpha\mu}. \quad (2.8)$$

This tensor obeys the following relationships:

$$R_{\mu\nu\sigma}{}^{\lambda} = -R_{\nu\mu\sigma}{}^{\lambda}, \quad (2.9)$$

$$R_{[\mu\nu\sigma]}{}^{\lambda} = 0, \quad (2.10)$$

$$R_{\mu\nu\sigma\lambda} = -R_{\mu\nu\lambda\sigma}, \quad (2.11)$$

and the Bianchi identity,

$$\nabla_{[\mu}R_{\nu\sigma]\lambda}{}^{\gamma} = 0. \quad (2.12)$$

The importance of this last identity will become clear shortly.

We now have the means to measure curvature through the Riemann tensor, which can be computed from the metric that we have defined on our

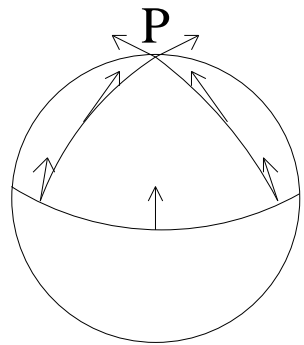
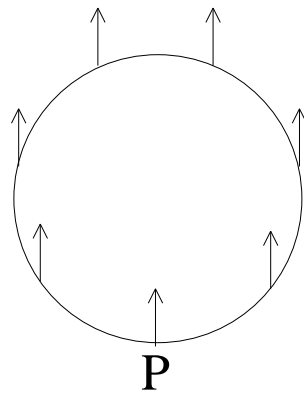


Figure 2.1: (Top) A vector is parallel transported around a circle and back to the original point, P , in flat, Euclidean geometry. It remains unchanged. (Bottom) a vector is parallel transported on the surface of a curved manifold (a 2-sphere) along a closed path back to the original point, P . It undergoes a rotation.

spacetime manifold. Let us now relate what we have to Einstein's equations. To do this, we must define a new tensor by contracting the second and fourth indices of the Riemann tensor

$$R_{\mu\sigma} = R_{\mu\nu\sigma}{}^{\nu}. \quad (2.13)$$

This is the Ricci tensor and it can be contracted with the inverse metric to yield the Ricci scalar

$$R = g^{\mu\sigma} R_{\mu\sigma} = R_{\mu}{}^{\mu}. \quad (2.14)$$

The Einstein tensor can now be defined,

$$G_{\mu\nu} \equiv R_{\mu\nu} - \frac{1}{2}g_{\mu\nu}R. \quad (2.15)$$

But why relate the *Einstein* tensor to the stress-energy tensor? Well, the stress-energy tensor obeys local energy conservation:

$$\nabla_{\mu} T^{\mu\nu} = 0. \quad (2.16)$$

So what is needed is a tensor which not only contains the information for the curvature of the spacetime manifold but also has zero divergence. The importance of the Bianchi identity (2.12) is now clear because it leads to the necessary property,

$$\nabla_{\mu} G^{\mu\nu} = 0. \quad (2.17)$$

2.2 Solving Einstein's Equations

Solving Einstein's equations (2.1) means finding the metric of the spacetime manifold. A closer look at the Einstein tensor shows that there are equations involving second order time derivatives of the metric ($G_{\mu\nu}$ contains first

order derivatives of the Christoffel connections which themselves contain first order derivatives of the metric). The system can be thought of (very loosely) as wave equations. A second order wave equation for the metric would require initial data consisting of the metric at the initial time as well as its first time derivative. Can this initial data be freely specified? Let us take a closer look at the divergence of the Einstein tensor to see. We have:

$$\partial_0 G^{0\nu} = -\partial_i G^{i\nu} - \Gamma^\alpha_{\alpha\beta} G^{\beta\nu} - \Gamma^\nu_{\alpha\beta} G^{\alpha\beta}. \quad (2.18)$$

The right hand side of the equation cannot contain third order time derivatives of the metric. The Christoffel connections contain single time derivatives while the Einstein tensor will have single time derivatives of the connections (so there will be at most second order time derivatives of the metric). For this to hold for the left hand side, the $G^{0\nu}$ components must involve at most first order time derivatives of the metric. This means that the 4 equations given by

$$G_{0\nu} = 8\pi T_{0\nu} \quad (2.19)$$

relate the metric components and their first time derivatives to each other. They are not evolution equations but rather equations of constraint. Initial data cannot be completely freely specified, therefore, but must obey (2.19).

2.2.1 3 + 1 ADM Formulation

Given initial data which satisfy the constraints, we can use Einstein's equations to evolve the metric in time. As long as the initial data specified at the initial time on a spacelike hypersurface is complete (all of the spatial components of the metric and their first time derivatives must be given as initial data), all future values of the metric can be determined. Such a deterministic spacetime is called *globally hyperbolic*. In such a case, the entire

spacetime manifold can be foliated with spacelike hypersurfaces. There are several formulations that adopt this approach, but we will limit the current discussion to the ADM (Arnowitt, Deser, and Misner) formulation [22] of Einstein's equations. There are many references on this subject, such as [27] and [9]. In this $3 + 1$ decomposition of the spacetime manifold, \mathcal{M} , each of the spacelike hypersurfaces is defined by $t = \text{constant}$ where t , the time, can be viewed as a scalar field. A future-directed vector field, n^μ , which is orthogonal to the spacelike hypersurfaces can be used to define a projection tensor

$$\perp^\mu{}_\nu \equiv \delta^\mu{}_\nu + n^\mu n_\nu \quad (2.20)$$

that is used to find the spatial parts of tensors by projecting them onto the hypersurface. Applying this to the metric of the spacetime yields the spatial metric of the hypersurface

$$\gamma_{ij} = g_{ij} + n_i n_j. \quad (2.21)$$

(Recall that Latin indices range over the spatial values 1, 2, 3). The contravariant form of the spatial metric is

$$\gamma^{ij} = g^{ij} + n^i n^j \quad (2.22)$$

while the mixed form is simply the projection tensor. Now that we have a spatial metric, we can define covariant differentiation on the hypersurface

$$D_i \equiv \perp^\mu{}_i \nabla_\mu \quad (2.23)$$

where the spatial derivative operator is compatible with the spatial metric

$$D_i \gamma_{jk} = 0. \quad (2.24)$$

The Riemann curvature tensor for the hypersurface can be found by using the spatial metric, γ_{ij} , in expressions analogous to those given previously for the 4-dimensional case. Besides the notion of intrinsic curvature, there is also the notion of an extrinsic curvature, K_{ij} , which is the description of how each of the hypersurfaces is embedded in the spacetime manifold. It is defined as

$$K_{ij} = -\perp^\mu{}_i \perp^\nu{}_j \nabla_\mu n_\nu. \quad (2.25)$$

The extrinsic curvature can also be written in terms of the Lie derivative with respect to the normal vector field, n^μ :

$$K_{ij} = -\frac{1}{2} \mathcal{L}_n \gamma_{ij}. \quad (2.26)$$

The extrinsic curvature is a purely spatial, symmetric tensor and is effectively a time derivative of the spatial metric. It will be used to cast Einstein's equations in first order form (in time).

Now that we have discussed the hypersurfaces and the embedding, let us discuss how coordinates on the hypersurfaces are related. A lapse function, α and a shift vector β^i are needed to do this. The lapse is a measure of proper time for an observer moving normal to the hypersurfaces. The covariant form of the normal vector written explicitly in terms of the lapse is:

$$n_\mu = (-\alpha, 0, 0, 0). \quad (2.27)$$

The shift describes the change in x^i , the spatial coordinates, from one hypersurface to the next (see Fig. 2.2). The spacetime metric can be written in terms of these quantities as

$$ds^2 = -\alpha^2 dt^2 + \gamma_{ij} (dx^i + \beta^i dt) (dx^j + \beta^j dt). \quad (2.28)$$

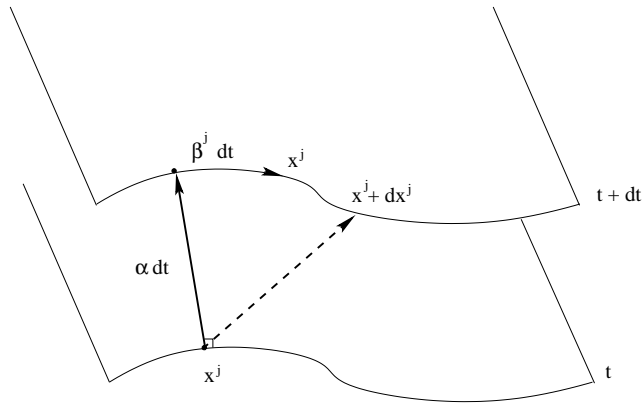


Figure 2.2: Diagram of the 3 + 1 decomposition of the spacetime manifold into spacelike hypersurfaces.

Now that the spacetime geometry has been split into spacelike hypersurfaces and we have described how coordinates on these hypersurfaces relate to each other, we are ready to split Einstein's equations. This is done in similar fashion by projecting tensors onto the hypersurfaces and along the normal vector n^μ . The requisite projections of the stress-energy tensor are:

$$\rho \equiv T_{\mu\nu} n^\mu n^\nu \tag{2.29}$$

$$j^\mu \equiv -\perp^\mu{}_\nu T^{\sigma\nu} n_\sigma \tag{2.30}$$

$$S_{\mu\nu} \equiv \perp^\sigma{}_\mu \perp^\lambda{}_\nu T_{\sigma\lambda} \quad (2.31)$$

Here ρ is the local energy density, j^μ is the momentum density, and $S_{\mu\nu}$ is the spatial stress tensor as measured by observers moving normally to the hypersurface. The energy and momentum densities are needed for the constraint equations. The *Hamiltonian constraint* is given by:

$$\mathcal{R} + K^2 - K^i{}_j K^j{}_i = 16\pi\rho \quad (2.32)$$

where \mathcal{R} is the trace of the spatial Ricci tensor

$$\mathcal{R} \equiv \gamma_{ij} \mathcal{R}^{ij} \quad (2.33)$$

and K is the trace of the extrinsic curvature tensor:

$$K \equiv \gamma_{ij} K^{ij}. \quad (2.34)$$

The *momentum constraint* is:

$$D_j K_i{}^j - D_i K = 8\pi j_i \quad (2.35)$$

The evolution equations of the spatial metric and the extrinsic curvature take the form:

$$\partial_t \gamma_{ij} = -2\alpha K_{ij} + D_i \beta_j + D_j \beta_i \quad (2.36)$$

$$\begin{aligned} \partial_t K_{ij} = & \mathcal{L}_\beta K_{ij} - D_i D_j \alpha + \alpha \left(\mathcal{R}_{ij} + K K_{ij} - 2K_{im} K^m{}_j \right. \\ & \left. - 8\pi \left(S_{ij} - \frac{1}{2} \gamma_{ij} (S - \rho) \right) \right) \end{aligned} \quad (2.37)$$

where S is the trace of the spatial stress tensor

$$S \equiv \gamma_{ij} S^{ij}. \quad (2.38)$$

Now that we have the ADM form of Einstein's equations, we are ready to solve them. Initial data that satisfies the constraints is specified on a spacelike hypersurface at the initial time and the evolution equations can then be used to evolve γ_{ij} and K_{ij} . This is called a free evolution. The Bianchi identity ensures that the constraints are preserved throughout the evolution. Another method is to evolve some components of γ_{ij} and K_{ij} and then solve the constraints at each time step for the remaining components. This is referred to as a constrained evolution.

Chapter 3

Numerical Methods

This chapter gives an introduction to the numerical implementation of differential equations via finite-difference methods. Various derivative operators will be defined and their associated error will be explained. Difference schemes for time dependent evolution equations will be discussed as will the stability properties of the schemes. We will then show how the numerical solution is checked for convergence to the continuum solution that it approximates. Finally, we show how to quantify the difference solution's truncation error.

The geometric tensor language of general relativity is both beautiful and powerful. One of its advantages is that some calculations can be performed in a coordinate independent fashion. Unfortunately, if we are actually to solve Einstein's equations, we must define a coordinate system. When this is done, we have a set of nonlinear partial differential equations (PDEs) whose solution will require the use of numerical analysis. This is typical of many nonlinear PDEs. Only in the rarest of cases can closed form solutions be found.

3.1 Finite-Difference Methods

One method for numerically solving a differential equation is to use finite-difference approximations. The idea is to define a numerical grid of coordinate points. It is at these points that the values of the functions and

the derivatives in the differential equation are defined. In this way, the entire equation is discretized. Most importantly, the continuous derivative operators can be replaced by algebraic ones.

In order to define examples of discrete derivative operators, first consider the Taylor expansion of a function:

$$f(x+h) = f(x) + f'(x)h + \frac{1}{2!}f''(x)h^2 + \dots \quad (3.1)$$

where the primes (\prime) denote the continuous derivative of the function with respect to x and h is the grid spacing. Solving for the derivative gives:

$$f'(x) = \frac{f(x+h) - f(x)}{h} + O(h). \quad (3.2)$$

This approximation is first order accurate in h . At leading order, the discrete approximation differs from its continuous counterpart by this error term. This is a very crucial point which will be discussed in depth later. For now, let us derive a more accurate derivative. We Taylor expand our function in the other direction:

$$f(x-h) = f(x) + f'(x)(-h) + \frac{1}{2!}f''(x)(-h)^2 + \dots \quad (3.3)$$

Subtracting (3.3) from (3.1) causes the second derivative terms to cancel. Solving for the first derivative gives:

$$f'(x) = \frac{f(x+h) - f(x-h)}{2h} + O(h^2). \quad (3.4)$$

Thus this difference expansion has $O(h^2)$ accuracy when it is centered at x . This procedure can be continued to find finite-difference operators of different orders of accuracy. It can also be used to find FD operators which approximate higher derivatives. A brief summary of some of the possible FD operators are given in Table 3.1.

3.1.1 Stability

One of the most challenging tasks when solving a hyperbolic equation numerically is achieving a stable evolution. Once the equation is discretized, it often contains far richer solutions than the continuum equation. Some of these are high frequency modes which can grow with time. They are of no interest since they are not modes of the continuum solution. It is this solution, after all, which we are trying to find.

The continuum evolution equation has a characteristic structure which determines its past domain of dependence see Fig. 3.1. The discretized equation has its own domain of dependence. In order to have a stable evolution, the time step, Δt , must be chosen such that the FD domain of dependence uncompasses that of the continuum system. If the time step, Δt , is chosen to be too large, a portion of the continuum domain of dependence is excluded in the FD update. This exclusion results in an unstable evolution. This is the Courant stability condition. This condition is perhaps the most straightforward for determining stability for explicit FD schemes. It is a necessary condition in most instances, but it is often far from sufficient.

Table 3.1: Some of the many finite-difference expressions are summarized below.

<i>Derivative</i>	<i>Finite Difference Expressions</i>
$\partial_x f_j$	$= (f_{j+1} - f_j)/h + O(h)$
$\partial_x f_j$	$= (f_j - f_{j-1})/h + O(h)$
$\partial_x^2 f_j$	$= (f_j - 2f_{j+1} + f_{j+2})/h^2 + O(h)$
$\partial_x^2 f_j$	$= (f_j - 2f_{j-1} + f_{j-2})/h^2 + O(h)$
$\partial_x f_j$	$= (f_{j+1} - f_{j-1})/h + O(h^2)$
$\partial_x f_j$	$= (-3f_j + 4f_{j+1} - f_{j+2})/2h + O(h^2)$
$\partial_x f_j$	$= (3f_j - 4f_{j-1} + f_{j-2})/2h + O(h^2)$
$\partial_x^2 f_j$	$= (f_{j+1} - 2f_j + f_{j-1})/h^2 + O(h^2)$
$\partial_x^2 f_j$	$= (-f_{j+3} + 4f_{j+2} - 5f_{j+1} + 2f_j)/h^2 + O(h^2)$
$\partial_x^2 f_j$	$= (2f_j - 5f_{j-1} + 4f_{j-2} - f_{j-3})/h^2 + O(h^2)$
$\partial_x f_j$	$= (-f_{j+2} + 8f_{j+1} - 8f_{j-1} + f_{j-2})/12h + O(h^4)$
$\partial_x^2 f_j$	$= (-f_{j+2} + 16f_{j+1} - 30f_j + 16f_{j-1} - f_{j-2})/12h^2 + O(h^4)$

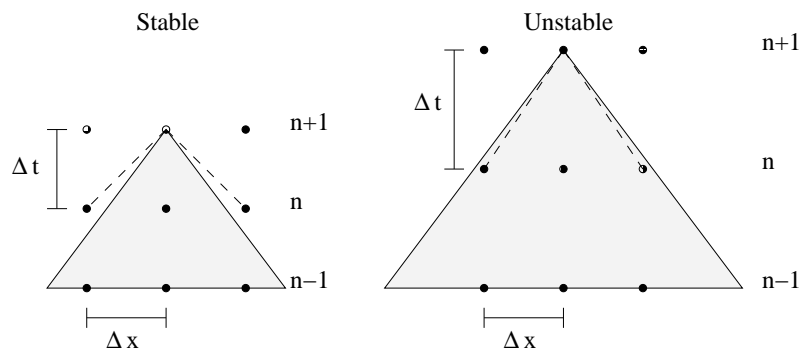


Figure 3.1: Diagram of Courant stability for an explicit finite-difference update scheme. The continuum equation being approximated has a characteristic structure represented by a shaded domain of dependence above. In the stable case (left) the time step, Δt , has been chosen such that the FD domain of dependence uncompasses that of the continuum system. In the unstable case (right) the time step, Δt , has been chosen to be too large which means that a portion of the continuum domain of dependence is excluded in the FD update. This exclusion results in an unstable evolution.

As a simple example of an evolution equation, let us take the advection equation:

$$\partial_t u = \partial_x u. \quad (3.5)$$

We can approximate this using an implicit Crank-Nicholson update scheme:

$$\frac{u_j^{n+1} - u_j^n}{\Delta t} = \frac{1}{2} \left(\frac{u_{j+1}^{n+1} - u_{j-1}^{n+1}}{2\Delta x} + \frac{u_{j+1}^n - u_{j-1}^n}{2\Delta x} \right) \quad (3.6)$$

where we have adopted a standard finite difference notation $u_j^n \equiv u(n\Delta t, j\Delta x)$. Notice that there are two second order accurate (in space) spatial derivatives on the right hand side. They are being averaged over two different time levels to produce a spatial derivative which is centered at the $n + 1/2$ time step. If the right hand side is being centered at this time step, then so is the left hand side. This makes the FD approximation of the time derivative second order accurate in time.

Implicit schemes like this are in general very stable. However, instabilities may still arise. One method to improve stability is to use dissipation operators. The specific form of these usually depends on the equation being solved and the type of discretization. One way of adding dissipation to the CN update scheme above is to add the term:

$$\frac{\epsilon}{16} [6u_j^n + u_{j+2}^n + u_{j-2}^n - 4(u_{j+2}^n - u_{j-2}^n)]$$

to the right hand side. The parameter ϵ is adjusted to control the damping of high frequency modes. Typical values for stability are $0 < \epsilon < 1$.

3.1.2 Truncation Error

This section closely follows lecture notes by Choptuik, [10].

Now that we have a stable scheme, we need to determine how accurate our solution is. In particular, we would like to know if our solution tends to the continuum solution in the limit where the grid spacing goes to zero, $h \rightarrow 0$. Let us write a continuum differential equation as:

$$Lu = f \tag{3.7}$$

where L is the differential operator of the system, f is some function, and u is the solution. The finite-differenced approximation (FDA) is:

$$\hat{L}\hat{u} = \hat{f}. \tag{3.8}$$

where \hat{f} is the function evaluated on the grid, \hat{u} is the discrete solution, and \hat{L} is the finite-differenced approximation to L .

The solution error is defined to be

$$\hat{e} \equiv u - \hat{u}. \tag{3.9}$$

It is common to make the *assumption of equal errors* in which we take the solution error to be of the same order as that of the truncation error, $\hat{\tau}$ which is defined to be:

$$\hat{\tau} \equiv \hat{L}u - \hat{f}. \tag{3.10}$$

Note that u is the solution to the *continuum* equation. As the name suggests, the truncation error is the result of truncating the number of terms in the approximation of the derivative operators like we did for equation (3.4). For an $O(h^2)$ approximation:

$$\hat{\tau} = h^2\tau_2 + h^4\tau_4 + \dots \tag{3.11}$$

where τ_2 and τ_4 , etc. are error functions which are independent of the grid spacing, h . The discrete solution, \hat{u} , in terms of the continuum solution, u is:

$$\hat{u} = u + h^2 e_2 + h^4 e_4 + \dots \quad (3.12)$$

This is the celebrated Richardson expansion and was known as early as 1910. The terms e_2 and e_4 are the second order and fourth order error functions, respectively. These functions are independent of the grid spacing, h . We are now ready to determine our error.

Suppose we have discrete solutions which, by assumption, are second order accurate. From (3.12) we have at mesh spacing, h :

$$\hat{u}^h = u + h^2 e_2 + \dots \quad (3.13)$$

while at mesh spacing $2h$ we have:

$$\hat{u}^{2h} = u + (2h)^2 e_2 + \dots \quad (3.14)$$

We can estimate the leading order solution error by subtracting these two solutions:

$$\hat{u}^{2h} - \hat{u}^h \approx 3h^2 e_2. \quad (3.15)$$

To leading order, this is 3 times the solution error for u^h . But how do we know that our approximation is $O(h^2)$ accurate? We can use an $O(h^2)$ discretization, but operationally we want to verify that we do indeed have this order of accuracy. Let us continue what we have started and subtract the discrete solutions \hat{u}^{4h} and \hat{u}^{2h} to get:

$$\hat{u}^{4h} - \hat{u}^{2h} \approx 12h^2 e_2. \quad (3.16)$$

This means that we will generally find:

$$Q^h \equiv \frac{\hat{u}^{4h} - \hat{u}^{2h}}{\hat{u}^{2h} - \hat{u}^h} = 4. \quad (3.17)$$

So the order of accuracy of a FDA can always be checked through this type of *convergence* check. An $O(h^2)$ accurate scheme should have a convergence factor, Q^h , that tends to 4 as $h \rightarrow 0$.

In summary, it is good to be able to find the truncation error of a discrete solution as in (3.15), but this does not verify that the order of accuracy is what it should be. A convergence check must always be performed to ensure that the system is being solved in a manner consistent with the approximation.

3.2 Spectral Methods

Spectral methods are a very accurate and efficient means of finding numerical solutions of differential equations [5]. The idea is to approximate the solution function as a sum of basis functions. There are a variety of different methods that fall under the classification of “spectral methods” (i.e. Tau, Galerkin, pseudospectral collocation). We will restrict discussion to the pseudospectral collocation (PSC) method. The *pseudospectral* methods use a set of grid points associated with the basis functions and employ interpolation; i.e. interpolation is used to convert the values of the function at the grid (collocation) points to the coefficients of the expansions. The other spectral methods use inner products (integration) to find the coefficients. One reason why we have chosen to use PSC is that the method can be used to solve nonlinear problems.

There are a variety of basis functions that one can use for the collocation method: Chebyshev, Fourier, Legendre, rational Chebyshev, Laguerre, Hermite, to name a few. We will only use the Chebyshev basis here. It has the advantage of being very well suited for solving most differential equations, and it allows one to use the FFT (Fast Fourier Transform) for interpolation

which makes it both fast and easy to implement in parallel. The symmetries of a problem or the domain on which it is to be solved often suggest which choice of basis is best suited for the situation. Chebyshev polynomials work for practically any symmetry.

3.2.1 Chebyshev Basis and Collocation Grid

Let us take a look at the method. The function is approximated as a series:

$$u_N(x) = \sum_{j=0}^N a_j T_j(x) \quad (3.18)$$

where $T_j(x)$ are the Chebyshev polynomials and N is the order at which the expansion is truncated. They are the solutions to:

$$(1 - x^2) \frac{d^2 T_j}{dx^2} - x \frac{dT_j}{dx} + j^2 T_j = 0. \quad (3.19)$$

This ODE is singular at $x = \pm 1$. The basis functions can be found from a 3-term recurrence relation.

$$T_{j+1}(x) = 2xT_j(x) - T_{j-1}(x) \quad , \quad T_0 = 1 \quad (3.20)$$

The first few functions are listed in Table 3.2.1. The grid points (collocation

Table 3.2: The first few Chebyshev basis functions.

<i>Chebyshev basis function</i>	<i>polynomial in x</i>
T_0	= 1
$T_1(x)$	= $2x$
$T_2(x)$	= $4x^2 - 1$
$T_3(x)$	= $8x^3 - 4x$

points) defined on the range $[-1, 1]$ are determined by:

$$x_j = \cos\left(j\frac{\pi}{N}\right) \quad ; \quad j = 0, \dots, N. \quad (3.21)$$

This is the Gauss-Lobatto or endpoints grid. The extrema of the Chebyshev polynomials occur at these grid points. Another grid, which omits the endpoints, is the Gauss-Chebyshev grid:

$$x_j = \cos\left[(2j-1)\frac{\pi}{2N}\right] \quad ; \quad j = 1, \dots, N. \quad (3.22)$$

The roots of the polynomials occur at these grid points. The choice of grid is one of preference, and we typically use the Gauss-Lobatto grid.

3.2.2 Spatial Derivatives

3.2.2.1 Fast Fourier Transform

Before discussing spatial derivatives, let us first look at the Chebyshev polynomials in a different coordinate system. Notice that under the coordinate transformation

$$x = \cos(\theta) \quad (3.23)$$

equation (3.19) becomes

$$\frac{d^2 T_j}{d\theta^2} + j^2 T_j = 0. \quad (3.24)$$

The solutions to this ODE are simply

$$T_j(\theta) = \cos(j\theta) \quad (3.25)$$

and, of course, these are just the Chebyshev polynomials. In the θ coordinates the grid points are now evenly spaced. Conditions are right for using a Fourier transform —specifically a Fast Cosine Transform (FCT).

3.2.2.2 Finding Derivatives

Since the Chebyshev basis functions are simply cosine functions when expressed in the θ coordinate system, the coefficients of the spectral expansion, (3.18), can be found by taking the cosine Fourier transform of the grid function. One may wonder why the coefficients of the expansion are even needed. They are necessary because they will be used to determine the spatial derivative of the function. This can be done in one of two ways: either the derivative of each of the *basis functions* in (3.18) can be evaluated, or the Chebyshev basis functions can be used but with new coefficients for the derivative's spectral expansion. The coefficients of $u_N(x)$ can be used to find the coefficients of $u'_N(x)$ through the following recurrence relation.

$$a'_{j-1} = 2ja_j + a'_{j+1} \quad , \quad a'_N = 0 \quad ; \quad j = N, N-1, \dots, 1 \quad (3.26)$$

we then have:

$$\frac{du_N}{dx} = \sum_{j=0}^N a'_j T_j(x) \quad (3.27)$$

As with the a_j 's, the coefficients for the derivative can now be Fourier transformed into grid values.

3.2.3 Nonlinear Hyperbolic (or Parabolic) Equations

In order to solve a differential equation numerically using a grid, one must be able to approximate the values of the functions as well as their derivatives at each of the grid points. In the last section we discussed how to take spatial derivatives. We are now ready to solve differential equations. We will begin with evolution equations since they are often easier to solve. The discussion is of hyperbolic systems in particular, but the method we outline is applicable to parabolic systems as well.

To approximate temporal derivatives we do not use a spectral expansion. Instead a finite-difference approximation is used:

$$\frac{u_j^{n+1} - u_j^n}{\Delta t} = F[x_j, u_j^{n+\frac{1}{2}}, (u'_j)^{n+\frac{1}{2}}] \quad (3.28)$$

The right hand side, $F[. . .]$, is some nonlinear functional. The time derivative is 2nd order accurate in the temporal discretization, h_t , but 4th order in spatial discretization, h_x . The spatial discretization, h_x , is taken to be the largest spacing of points which occurs at the center of our nonuniform grid

$$h_x \propto \frac{1}{N}. \quad (3.29)$$

The points cluster towards the ends of our grid where the spacing is:

$$\Delta x \propto \frac{1}{N^2}. \quad (3.30)$$

The temporal discretization is uniform and we have $h_t = \Delta t$. The temporal discretization is related to the *smallest* spatial discretization through the CFL condition:

$$\Delta t = \lambda \Delta x \quad (3.31)$$

The constant λ is known as the Courant factor. This relationship between the temporal and spatial grids is necessary whenever an explicit update scheme is used. The value of Δt needs to be small enough so that the evolution is stable. There are many update schemes which can be used, but we have had the most success with iterative Crank-Nicholson. The iterative implementation is explicit and is therefore governed by the CFL condition. One feature of this update scheme is that one can continue to iterate until the change in the future value of the function is below some tolerance. This predictor-corrector method allows one to obtain very accurate results although the truncation error will always be limited by the temporal derivative.

What one now needs in order to complete the solution algorithm are boundary conditions and initial data. The initial data is just the function defined on the grid points at the initial time. This grid function is then Fourier transformed, to determine the coefficients of its spectral expansion. These coefficients are used in 3.27 to get the coefficients of the derivative expansion. The derivative coefficients are then inverse Fourier transformed to yield grid values of the function's derivative. This enables us to evaluate the right hand side of our hyperbolic equation. Notice that this procedure applies equally well to linear and nonlinear equations.

Since the finite-differenced temporal derivative has the largest truncation error, it fixes the order of the accuracy:

$$u_N = u + \epsilon_2 \frac{1}{N^4} \tag{3.32}$$

where u_N is the spectral solution, u is the true solution to the continuum equation, and the last term in the equation is the truncation error. As N is increased the spectral solution approaches the true solution. Notice that the convergence is polynomial and not exponential.

3.2.4 $2h$ Waves and Aliasing

Instabilities can occur due to $2h$ waves, where h is the grid spacing (in θ coordinates). The waves with a wavelength of $2h$ are the highest frequency waves that can be represented on a grid. They are usually nonphysical numerical artifacts and should be eliminated for two reasons. First, because of their poor resolution they cannot be accurately represented even if they did correspond to some real physical phenomena. Second, they often lead to unstable evolutions since these modes often grow the fastest. This, in general, depends

on whether or not the implementation of the particular PDE has an amplification factor that is greater than 1 for these frequencies. If the amplification factor does exceed unity, then upon each successive update of the solution, the associated mode gets amplified and grows. It is also possible to have an amplification factor that amplifies *low* frequencies but experience shows that it is almost always growing high frequencies that are troublesome. Anyway, one way of causing these $2h$ waves is by violating the CFL condition. So the first thing to try when noticing $2h$ waves in a spectral evolution is to decrease the time step. If this does not remove the $2h$ modes, then either a dissipation operator must be introduced (or a hyperviscosity term) or the offending waves must be eliminated directly by setting the last coefficient of the expansion to zero. This latter method is very easy and should be done before attempting to modify the equation with dissipation operators.

Aliasing can also be caused by exciting the higher frequency modes of the expansion. In this case, the last third or half of the wave modes get excited, instead of just the highest frequency mode alone. The cause for aliasing error is different, however. In order to have an aliasing instability, one has to have a differential equation that is nonlinear or one that has non-constant coefficients. A term like: $xu(x)$ has powers of x outside of the truncation. These higher order terms will get represented by lower order terms. The effect is a cascade of higher wave numbers to lower ones.

3.2.5 Elliptic Equations

One can solve nonlinear, elliptic PDEs using spectral methods via relaxation. The basic idea is to specify a guess for the solution u^0 , solve for a correction to the function, δu^0 , which will determine the function at the next

iteration via:

$$u^1 = u^0 + \delta u^0. \tag{3.33}$$

Iterations are continued until the function converges to the solution of the nonlinear, elliptic PDE.

It might seem possible to use the Newton-Raphson method to linearize the problem and solve an algebraic equation for the update as is done in finite-difference methods. This will not work since spectral derivatives are not local algebraic combinations of the grid values of the function. In FD methods finding the variation of a derivative term with respect to the function is easy (for a 1st derivative it would just yield a $1/\Delta x$ term). One can try to form a similar term in a spectral method (perhaps by taking the ratio of the second derivative of the function to its first derivative). This always fails miserably. Even if the δu found in this way were correct, it is still being found locally using the grid values as the unknowns. The problem with finding the correction locally is that the next iteration would be the result of a point-by-point adjustment to the previous iterate. It should not come as too much of a surprise that this fails since correcting each grid point individually would probably cause the next iteration to have high frequency noise (spiky). This would get worse as global derivatives would be repeatedly taken of this sharp-featured function at every iteration.

For spectral methods one must use the Newton-Kantorovich method to linearize the PDE (which requires the use of Frechet derivatives). This produces a linear *differential* equation which must be solved for the correction term.

$$D_f R(u, u_x, \dots) = -R(u, u_x, \dots) \tag{3.34}$$

$D_f R(u, u_x, \dots)$ is the Frechet derivative of the residual:

$$D_f R(u, u_x, \dots) = \frac{\delta R}{\delta u} \delta u + \frac{\delta R}{\delta u_x} \delta u_x + \dots \quad (3.35)$$

In this last expression there are terms for the function, u , and each of its spatial derivatives that appear in the residual. Posing the problem in this way results in a linear system which is solved for the coefficients of the expansion for the correction, δu_c :

$$Ax = b \quad (3.36)$$

where A is a matrix whose elements are composed of combinations of the Chebyshev polynomials and their derivatives evaluated at the collocation points (the particular combination determined by the Frechet derivative of the residual). The vector x is the vector of the coefficients of the correction. Rows of A will be allocated for boundary conditions that need to be imposed for the *update*. The vector b will contain the appropriate number of boundary values and the negative residual of the full nonlinear PDE being solved.

The method for finding the spatial derivatives when posing the problem in this way is a little different than the algorithm described above for hyperbolic problems. Instead of using Chebyshev basis functions for the function's expansion *and* the derivative's expansion, and converting the function's coefficients into those for the derivative, one instead modifies the basis functions. The basis functions used for the derivative expansion are just the derivative of the Chebyshev polynomials.

$$\frac{du_N}{dx} = \sum_{j=0}^N a_j T'_j(x) \quad (3.37)$$

Taking the derivative in this way allows one to use the *same* coefficients for the function's expansion and the expansion for the derivative. Of course one

can always choose to evaluate spatial derivatives in this way (and some people prefer to) but we typically use the recurrence relations whenever possible. Thus we use the recurrence relations for evolution problems but not for the elliptic problems since working with the coefficients requires taking derivatives of the polynomials themselves.

The final solution of an elliptic problem solved in this way will have spectral accuracy. The number of basis functions, N , determines not only the resolution of the grid, but also the order of the truncation error.

$$u_N = u + \epsilon_N \frac{1}{N^N} \tag{3.38}$$

u_N is the spectral solution, u is the continuum solution, and the last term in the equation is the truncation error. As N is increased the spectral solution approaches the true solution. This is what is meant by exponential convergence of the spectral approximation.

This is the general idea behind solving nonlinear elliptic problems. However, elliptic problems are often very expensive to solve. The solution of the linear system requires $O(N_p^3)$ operations where N_p is the *total number of basis functions or grid points*. It is easy to see how quickly a problem like this can become intractable in higher dimensions. As a result, techniques such as domain decomposition and finite-difference preconditioning are often employed [5].

3.2.6 Spectral Methods in Higher Dimensions

Applying spectral methods in higher dimensions can be quite expensive if one takes a naive approach. However if care is taken, spectral methods remain a very accurate and efficient way to solve multi-dimensional PDEs.

For example, one spectral approximation in two-dimensions is:

$$f(x, y) = \sum_{m=0}^{M-1} \sum_{n=0}^{N-1} a_{mn} T_m(x) T_n(y). \quad (3.39)$$

The Chebyshev functions are used to form a tensor product basis. The collocation grid in this case is also a nonuniform tensor product grid. A naive evaluation of the above series would require $O(M^2 N^2)$ operations. This can be reduced to $O(MN^2) + O(M^2 N)$ by using the method of partial sums. In order to do this, the basis and the collocation grid must be tensor products. Since Chebyshev polynomials are being used the FFT will further increase efficiency to: $O(MN \log_2(N)) + O(MN \log_2(M))$. Another benefit of using the Chebyshev basis functions is that higher dimensional FFTs are naturally suited to parallelization.

Chapter 4

Einstein-Dirac System

4.1 Introduction

Much of this chapter is taken from a paper written with Douglas W. Schaefer, Daniel A. Steck, and Matthew W. Choptuik which is currently in preparation. This work was originally done as a project which was inspired by a paper written by Finster, Smoller, and Yau [12] presenting solutions for a static, massive Einstein-Dirac field. Our study is of the dynamic form of this system and it is not exhaustive. Several solutions are presented but the most important of these (for the purposes of this thesis) is the Type II critical solution which is found at the threshold of black hole formation as the mass is decreased. It is this solution which originally motivated the investigation of the massless system presented in subsequent chapters. Note: Throughout this chapter, we will use the metric signature $(+, -, -, -)$.

We investigate the dynamics of the massive Einstein-Dirac equation in spherical symmetry. Since a fermion's spin has an orientation in space, one fermion alone can not be treated as a spherically symmetric system. To preserve the symmetry, we investigate two fermions in a singlet spinor state, where the particles have opposite spin. This fermionic field is massive and can be thought of as representing two idealized neutrons, since we do not consider any coupling to the electromagnetic field. The system is a dynamic version of the model considered by Finster, Smoller, and Yau [12]. The fermion field is

treated as a classical field i.e. a non-quantum-mechanical object.

In this system, the dispersive nature of the massive field competes with the self-attraction resulting from the coupling to gravity. In trying to achieve a balance between these two forces, we observed both unstable and stable solutions. The unstable solutions correspond to the threshold between black hole collapse and dispersal. However, in accordance with the findings of [12], we also found a continuum of stable solutions that were solitonic in nature. These tended to oscillate and approach the stable, static solutions that we found through independent techniques.

4.1.1 Equations of Motion

In this section we present the equations of motion for the Dirac field and the spacetime geometry. We simply reproduce here what was done in [12], except we allow for a dynamic spacetime. It should be noted that there are many differences between the Finster, et al derivation and what is typically done in the literature [3]. In particular, the authors do not define a spinor affine connection and the components of the stress-energy tensor that they compute are complex, though subsequently, only the real parts of these components are used. We will follow a more canonical approach in subsequent chapters where we investigate the *massless* Einstein-Dirac system. For that case, we will derive the equations of motion from first principles.

The Einstein-Dirac equations are of the form

$$G_{\mu\nu} = 8\pi T_{\mu\nu} \tag{4.1}$$

$$(G - m)\Psi = 0, \tag{4.2}$$

where $T_{\mu\nu}$ is the stress-energy tensor of the field, G is the Dirac operator, and Ψ is the wavefunction of the fermion with mass m .

4.1.1.1 The Dirac Operator

The form of the Dirac equation (4.2) can be used in curved spacetime. The Dirac operator is defined to be

$$G = i\gamma^\mu(x)\frac{\partial}{\partial x^\mu} + B(x), \quad (4.3)$$

where $\gamma^\mu(x)$ ($\mu = 0, 1, 2, 3$) are the Dirac matrices in curved spacetime, and $B(x)$ is a matrix needed to make the Dirac operator covariant. It is essentially the sum of the matrices formed by the product of the Dirac matrices and the spinor affine connections (had they been defined). Both $\gamma^\mu(x)$ and $B(x)$ are 4×4 matrices that depend on the spacetime coordinate x . The Dirac matrices can be found from the relation

$$g^{\mu\nu}\mathbb{1} = \frac{1}{2}\{\gamma^\mu, \gamma^\nu\}, \quad (4.4)$$

where

$$\{\gamma^\mu, \gamma^\nu\} = \gamma^\mu\gamma^\nu + \gamma^\nu\gamma^\mu. \quad (4.5)$$

We now restrict attention to spherical symmetry, and to treat the geometry, we adopt polar/areal (PA) coordinates. Specifically, the line element is:

$$ds^2 = \alpha^2(t, r)dt^2 - a^2(t, r)dr^2 - r^2d\theta^2 - r^2\sin^2\theta d\phi^2, \quad (4.6)$$

with

$$\sqrt{-g} = \alpha ar^2 \sin\theta, \quad (4.7)$$

where α and a are positive functions. The γ -matrices from Minkowski spacetime $\tilde{\gamma}^\mu$ can be used as a basis for the Dirac matrices $\gamma'^{mu}(x)$:

$$\tilde{\gamma}^0 = \begin{pmatrix} \mathbb{1} & 0 \\ 0 & -\mathbb{1} \end{pmatrix}, \quad \tilde{\gamma}^i = \begin{pmatrix} 0 & \sigma^i \\ -\sigma^i & 0 \end{pmatrix}, \quad i = 1, 2, 3 \quad (4.8)$$

In these expressions, $\mathbb{1}$ is the 2×2 identity matrix, and the σ^i are the Pauli spin matrices. The curved spacetime Dirac matrices are thus

$$\gamma^t = \frac{1}{\alpha} \tilde{\gamma}^0 \quad (4.9)$$

$$\gamma^r = \frac{1}{a} (\tilde{\gamma}^1 \cos \theta + \tilde{\gamma}^2 \sin \theta \cos \phi + \tilde{\gamma}^3 \sin \theta \sin \phi) \quad (4.10)$$

$$\gamma^\theta = \frac{1}{r} (-\tilde{\gamma}^1 \sin \theta + \tilde{\gamma}^2 \cos \theta \cos \phi + \tilde{\gamma}^3 \cos \theta \sin \phi) \quad (4.11)$$

$$\gamma^\phi = \frac{1}{r \sin \theta} (-\tilde{\gamma}^2 \sin \phi + \tilde{\gamma}^3 \cos \phi). \quad (4.12)$$

This representation is chosen so that the angular dependence of the spinor agrees with the one predicted for the Dirac spinors in the hydrogen atom for zero angular momentum [23]. We take the form of $B(x)$ to be

$$B = \frac{i}{2} \gamma'^\mu{}_{;\mu} \quad (4.13)$$

as shown in [12].

Using the results (4.9)-(4.13), the full time-dependent form of the Dirac operator becomes

$$G = i\gamma^t \left(\partial_t - \frac{1}{2} \frac{\dot{a}}{a} \right) + i\gamma^r \left(\partial_r + \frac{(1-a)}{r} + \frac{1}{2} \frac{\alpha'}{\alpha} \right) + i\gamma^\theta \partial_\theta + i\gamma^\phi \partial_\phi. \quad (4.14)$$

We use as our wave functions

$$\Psi_b = \frac{1}{\sqrt{ar}} \begin{pmatrix} z_1(r, t) e_b \\ i\sigma^r z_2(r, t) e_b \end{pmatrix}, \quad (4.15)$$

where $b = 1, 2$, $e_1 = (1, 0)$, $e_2 = (0, 1)$, and the prefactor is chosen so that the equations of motion do not contain time derivatives of $a(t, r)$. We also note

that z_1 and z_2 are in general complex. When either of these wave functions Ψ_b defined in (4.15) is substituted into the Dirac equation (4.2), the angular dependence can be removed leaving an equation of motion which is only dependent on (t, r) . Also, the effective number of wave function components is reduced from four to two. Hence, we may take z_1 and z_2 to be the matter field variables, in terms of which the Dirac equation becomes

$$\begin{aligned}\partial_t z_1 + i\sqrt{\frac{\alpha}{a}}\partial_r\left(\sqrt{\frac{\alpha}{a}}z_2\right) + i\frac{\alpha}{r}z_2 + im\alpha z_1 &= 0 \\ \partial_t z_2 - i\sqrt{\frac{\alpha}{a}}\partial_r\left(\sqrt{\frac{\alpha}{a}}z_1\right) + i\frac{\alpha}{r}z_1 - im\alpha z_2 &= 0.\end{aligned}\tag{4.16}$$

Alternatively, in terms of the real and imaginary parts of the matter variables, we have

$$\begin{aligned}\partial_t \text{Re}z_1 - \sqrt{\frac{\alpha}{a}}\partial_r\left(\sqrt{\frac{\alpha}{a}}\text{Im}z_2\right) - \frac{\alpha}{r}\text{Im}z_2 - m\alpha\text{Im}z_1 &= 0 \\ \partial_t \text{Im}z_1 + \sqrt{\frac{\alpha}{a}}\partial_r\left(\sqrt{\frac{\alpha}{a}}\text{Re}z_2\right) + \frac{\alpha}{r}\text{Re}z_2 + m\alpha\text{Re}z_1 &= 0 \\ \partial_t \text{Re}z_2 + \sqrt{\frac{\alpha}{a}}\partial_r\left(\sqrt{\frac{\alpha}{a}}\text{Im}z_1\right) - \frac{\alpha}{r}\text{Im}z_1 + m\alpha\text{Im}z_2 &= 0 \\ \partial_t \text{Im}z_2 - \sqrt{\frac{\alpha}{a}}\partial_r\left(\sqrt{\frac{\alpha}{a}}\text{Re}z_1\right) + \frac{\alpha}{r}\text{Re}z_1 - m\alpha\text{Re}z_2 &= 0.\end{aligned}\tag{4.17}$$

The probability density, $P(t, r)$, can be written in terms of the matter variables as [12]

$$P(t, r) \propto 4\pi (|z_1|^2 + |z_2|^2),\tag{4.18}$$

and is subject to the normalization condition

$$\int_0^\infty P(t, r)dr = 1.\tag{4.19}$$

We take the stress-energy tensor for a spin- $\frac{1}{2}$ field in curved spacetime to be [12]

$$T_{\mu\nu} = \frac{1}{2} \sum_{a=1}^2 \text{Re} \left[\bar{\Psi}_a \left(i\gamma_\mu \frac{\partial}{\partial x^\nu} + i\gamma_\nu \frac{\partial}{\partial x^\mu} \right) \Psi_a \right], \quad (4.20)$$

where $\bar{\Psi} \equiv \Psi^\dagger \tilde{\gamma}^0$. In order to obtain equations for the geometric variables α and a we need some of the 3 + 1 quantities defined in Chapter 2. Specifically we have

$$\begin{aligned} \rho &= n^\mu n^\nu T_{\mu\nu} \\ S_j^i &= \gamma^{ik} S_{kj} = \gamma^{ik} T_{kj} \end{aligned} \quad (4.21)$$

It is straightforward to compute ρ :

$$\begin{aligned} \rho &= n^\mu n^\nu T_{\mu\nu} = \frac{1}{\alpha^2} \text{Re}[T_{tt}] \\ &= \frac{2}{\alpha a r^2} \text{Re} (i z_1^* \partial_t z_1 + i z_2^* \partial_t z_2). \end{aligned} \quad (4.22)$$

Substituting into the general Hamiltonian constraint in spherical symmetry and PA coordinates,

$$\frac{\partial_r a}{a} + \frac{a^2 - 1}{2r} - 4\pi r a^2 \rho = 0, \quad (4.23)$$

we obtain

$$\frac{\partial_r a}{a} + \frac{a^2 - 1}{2r} = \frac{8\pi}{r} \frac{a}{\alpha} \text{Re} (i z_1^* \partial_t z_1 + i z_2^* \partial_t z_2). \quad (4.24)$$

Using the matter equations of motion (4.16), to eliminate the time derivatives, we find

$$\frac{\partial_r a}{a} + \frac{a^2 - 1}{2r} = \frac{8\pi}{r} \text{Re} \left[z_1^* \partial_r z_2 - z_2^* \partial_r z_1 + \frac{2a}{r} z_1 z_2^* + m a (|z_1|^2 - |z_2|^2) \right]. \quad (4.25)$$

Finally, in terms of the real and imaginary components, the Hamiltonian constraint becomes

$$\begin{aligned}
\frac{\partial_r a}{a} + \frac{a^2 - 1}{2r} &= \frac{8\pi}{r} \left[\text{Re}z_1 (\partial_r \text{Re}z_2) + \text{Im}z_1 (\partial_r \text{Im}z_2) \right. \\
&\quad - \text{Re}z_2 (\partial_r \text{Re}z_1) - \text{Im}z_2 (\partial_r \text{Im}z_1) \\
&\quad + \frac{2a}{r} (\text{Re}z_1 \text{Re}z_2 + \text{Im}z_1 \text{Im}z_2) \\
&\quad \left. + ma ((\text{Re}z_1)^2 + (\text{Im}z_1)^2 - (\text{Re}z_2)^2 - (\text{Im}z_2)^2) \right].
\end{aligned} \tag{4.26}$$

Similarly, we must calculate the component S_r^r :

$$\begin{aligned}
S_r^r &= \gamma^{rk} \text{Re}[T_{kr}] \\
&= \frac{1}{a^2} \text{Re}[T_{rr}] \\
&= \frac{1}{a^2 r^2} \text{Re}(z_1^* \partial_r z_2 - z_2^* \partial_r z_1).
\end{aligned} \tag{4.27}$$

We can substitute this result into the general form for the slicing condition in spherical symmetry and PA coordinates,

$$\frac{\partial_r \alpha}{\alpha} - \frac{a^2 - 1}{2r} - 4\pi r a^2 S_r^r = 0, \tag{4.28}$$

which yields

$$\frac{\partial_r \alpha}{\alpha} - \frac{a^2 - 1}{2r} = \frac{8\pi}{r} \text{Re}(z_1^* \partial_r z_2 - z_2^* \partial_r z_1). \tag{4.29}$$

In terms of the real and imaginary components of the matter variables, the slicing condition is

$$\begin{aligned}
\frac{\partial_r \alpha}{\alpha} - \frac{a^2 - 1}{2r} &= \frac{8\pi}{r} \left[\text{Re}z_1 (\partial_r \text{Re}z_2) + \text{Im}z_1 (\partial_r \text{Im}z_2) \right. \\
&\quad \left. - \text{Re}z_2 (\partial_r \text{Re}z_1) - \text{Im}z_2 (\partial_r \text{Im}z_1) \right].
\end{aligned} \tag{4.30}$$

4.1.2 Initial conditions

4.1.2.1 Centered Gaussian

The initial data family we have used consists of a stationary Gaussian multiplied by r and centered at the origin:

$$\begin{aligned}\operatorname{Re}z_1 &= N r \exp\left(-\left(\frac{r}{2\delta}\right)^2\right) \\ \operatorname{Im}z_1 &= 0 \\ \operatorname{Re}z_2 &= 0 \\ \operatorname{Im}z_2 &= 0.\end{aligned}\tag{4.31}$$

This data family satisfies the regularity conditions (4.63) and has one free parameter, δ , in addition to m . The normalization constant N is determined by (4.19):

$$N = \left(\frac{1}{4\pi}\right)^{\frac{1}{2}} \left(\frac{1}{2\pi\delta^2}\right)^{\frac{1}{4}}.\tag{4.32}$$

4.1.2.2 Propagating Gaussian

In addition to the centered data family, we developed the means for producing either ingoing or outgoing spherical shells with a Gaussian wave packet cross-section. It should be noted, however, that all of the results presented in this chapter were generated using only the initially stationary data given in (4.31).

The propagating initial data family consists of Gaussian wave packets

$$\begin{aligned}
z_1 &= NA_1 \exp\left(-\left(\frac{(r-r_0)}{2\delta}\right)^2\right) \exp(-ikr) \\
z_2 &= NA_2 \exp\left(-\left(\frac{(r-r_0)}{2\delta}\right)^2\right) \exp(-i(kr + \phi)),
\end{aligned} \tag{4.33}$$

where the normalization N is given by equation (4.32). The phase difference ϕ was chosen to be $-\pi/2$ based on the the observation from initial simulations that the ingoing portion of the wave always exhibits this phase difference between z_1 and z_2 . The constants A_1 and A_2 depend on the initial momentum of the wave packet and are set to maximize the fraction of the wave packet that is ingoing. This is accomplished by assuming that the probability density P is initially ingoing and (neglecting dispersion) is of the form

$$P = P(r + vt). \tag{4.34}$$

Therefore, we need A_1 and A_2 to satisfy

$$v\partial_r P = \partial_t P. \tag{4.35}$$

By using (4.18) to eliminate P , differentiating, and dividing both sides by 8π , we obtain

$$\begin{aligned}
&v (\operatorname{Re}z_1 \partial_r \operatorname{Re}z_1 + \operatorname{Im}z_1 \partial_r \operatorname{Im}z_1 + \operatorname{Re}z_2 \partial_r \operatorname{Re}z_2 + \operatorname{Im}z_2 \partial_r \operatorname{Im}z_2) \\
&= \operatorname{Re}z_1 \partial_t \operatorname{Re}z_1 + \operatorname{Im}z_1 \partial_t \operatorname{Im}z_1 + \operatorname{Re}z_2 \partial_t \operatorname{Re}z_2 + \operatorname{Im}z_2 \partial_t \operatorname{Im}z_2.
\end{aligned} \tag{4.36}$$

We then use the evolution equations (4.17) to eliminate the time derivative terms, while assuming flat spacetime ($a = \alpha = 1$), resulting in the condition

$$\begin{aligned}
& v (\operatorname{Re}z_1 \partial_r \operatorname{Re}z_1 + \operatorname{Im}z_1 \partial_r \operatorname{Im}z_1 + \operatorname{Re}z_2 \partial_r \operatorname{Re}z_2 + \operatorname{Im}z_2 \partial_r \operatorname{Im}z_2) \\
&= \operatorname{Re}z_1 \partial_r \operatorname{Im}z_2 - \operatorname{Im}z_1 \partial_r \operatorname{Re}z_2 - \operatorname{Re}z_2 \partial_r \operatorname{Im}z_1 + \operatorname{Im}z_2 \partial_r \operatorname{Re}z_1.
\end{aligned} \tag{4.37}$$

For our initial data, the phase relation $\phi = -\pi/2$ can be expressed as

$$\begin{aligned}
\operatorname{Re}z_2 &= -\left(\frac{A_2}{A_1}\right) \operatorname{Im}z_1 \\
\operatorname{Im}z_2 &= \left(\frac{A_2}{A_1}\right) \operatorname{Re}z_1.
\end{aligned} \tag{4.38}$$

Then substitution for $\operatorname{Re}z_2$ and $\operatorname{Im}z_2$ in (4.37) results in

$$v \left(1 + \left(\frac{A_2}{A_1} \right)^2 \right) = 2 \left(\frac{A_2}{A_1} \right), \tag{4.39}$$

in which all dependence on z_1 has cancelled. This quadratic equation in A_2/A_1 can then be solved to give

$$\frac{A_2}{A_1} = -\frac{1}{v} \pm \sqrt{\frac{1}{v^2} - 1}. \tag{4.40}$$

Taking the solution corresponding to the positive sign of the radical, this relation can be combined with the normalization requirement

$$\sqrt{A_1^2 + A_2^2} = 1 \tag{4.41}$$

to solve for the coefficients A_1 and A_2 :

$$\begin{aligned} A_1 &= \frac{v}{\sqrt{2(1 - \sqrt{1 - v^2})}} \\ A_2 &= \frac{\sqrt{1 - v^2} - 1}{\sqrt{2(1 - \sqrt{1 - v^2})}}. \end{aligned} \tag{4.42}$$

We tested these coefficients and found that they resulted in a wave that was almost entirely ingoing for large v . However, when the dispersion was fast relative to v (e.g. for small v) a significant portion of the initial wave packet was outgoing. This situation is expected due to the fact that our derivation of A_1 and A_2 for ingoing waves neglects the dispersion of the probability density. Also, by choosing a negative v , the coefficients given by (4.42) were found to be equally effective at producing outgoing waves.

4.1.3 Boundary conditions

We derive approximate radiation boundary conditions for the matter variables at the finite outer boundary R by first taking the limit of the evolution equations (4.16) as r approaches infinity:

$$\begin{aligned} \partial_t z_1 + i\partial_r z_2 + imz_1 &= 0 \\ \partial_t z_2 - i\partial_r z_1 - imz_2 &= 0. \end{aligned} \tag{4.43}$$

Taking the partial derivative of each equation with respect to time gives

$$\begin{aligned} \partial_{tt} z_1 + i\partial_{tr} z_2 + im\partial_t z_1 &= 0 \\ \partial_{tt} z_2 - i\partial_{tr} z_1 - im\partial_t z_2 &= 0. \end{aligned} \tag{4.44}$$

The third term of each of these equations can be eliminated by substitution of the corresponding time derivative from (4.43), and the second term of each

can be eliminated by substitution of the partial derivative with respect to r using the corresponding equation in (4.43). This procedure results in

$$\begin{aligned}\partial_{tt}z_1 - \partial_{rr}z_1 + m^2z_1 &= 0 \\ \partial_{tt}z_2 - \partial_{rr}z_2 + m^2z_2 &= 0.\end{aligned}\tag{4.45}$$

Therefore, at large r , the real and imaginary components of the matter variables each satisfy separate Klein-Gordon equations. If we neglect the m^2z_b ($b = 1, 2$) term in each equation, we are left with

$$\partial_{tt}z_b - \partial_{rr}z_b = 0.\tag{4.46}$$

The outward-propagating solution of (4.46) is

$$z_b(r, t) = g(r - t),\tag{4.47}$$

in which g is an arbitrary function. This solution also satisfies the first-order equations

$$\begin{aligned}\partial_t z_1 + \partial_r z_1 &= 0 \\ \partial_t z_2 + \partial_r z_2 &= 0,\end{aligned}\tag{4.48}$$

which serve as our approximate radiation boundary conditions. In practice, we have found that if the value of R is set large enough to include the bulk of the probability density, reflections from the outer boundary are negligible.

4.1.4 Static solutions

The static solutions of the Einstein-Dirac field were first studied in detail recently by Finster, Smoller, and Yau (FSY) [12]. The static solutions in this model result from a competition between gravitation and the dispersive nature of the massive wavepacket. The procedure followed by FSY is closely analagous to the procedure of Bartnik and McKinnon [1] for finding the static solutions in a spherically symmetric Einstein-Yang-Mills model.

For consistency with FSY, we use the metric variables T and A (instead of α and a), where

$$ds^2 = \frac{1}{T^2} dt^2 - \frac{1}{A} dr^2 - r^2 d\Omega^2. \quad (4.49)$$

Also, we use rescaled field variables z'_b ($b = 1, 2$) defined in terms of the previously defined field variables by

$$z'_b \equiv \sqrt{\frac{\sqrt{A}}{T}} z_b = \sqrt{\frac{\alpha}{a}} z_b \quad (4.50)$$

(we will drop the primes throughout the rest of this section). Then, in terms of the rescaled variables, the probability density becomes

$$P = 4\pi \frac{T}{\sqrt{A}} (|z_1|^2 + |z_2|^2). \quad (4.51)$$

We now adopt a static *ansatz* by factoring out a harmonic time dependence from both field variables:

$$z_b(r, t) = z_b(r) e^{-i\omega t}. \quad (4.52)$$

In this case, the dynamical equations (4.16-4.30) reduce to the static equations given by FSY:

$$\begin{aligned} \partial_r z_1 &= \frac{1}{r\sqrt{A}} z_1 - \frac{\omega T + m}{\sqrt{A}} z_2 \\ \partial_r z_2 &= \frac{\omega T - m}{\sqrt{A}} z_1 - \frac{1}{r\sqrt{A}} z_2 \\ \partial_r A &= \frac{1 - A}{r} - \frac{16\pi\omega T^2}{r} (z_1^2 + z_2^2) \\ \partial_r T &= \frac{T}{2rA} \left[A - 1 - 16\pi\omega T^2 (z_1^2 + z_2^2) + \frac{32\pi T}{r} z_1 z_2 + 16\pi m T (z_1^2 - z_2^2) \right]. \end{aligned} \quad (4.53)$$

Notice that all variables are time independent in these equations. Also, since all the coefficients in (4.53) are real, we may assume that z_1 and z_2 are real.

Because the static equations are singular at $r = 0$, we must begin the integration at some $r > 0$. Thus, we need regularity conditions for the variables at the origin, which we now derive. To begin, we assume that the variables are Taylor-expandable about $r = 0$:

$$\begin{aligned}
z_1(r) &= \alpha_0 + \alpha_1 r + \alpha_2 r^2 + \dots \\
z_2(r) &= \beta_0 + \beta_1 r + \beta_2 r^2 + \dots \\
A(r) &= A_0 + A_1 r + A_2 r^2 + \dots \\
T(r) &= T_0 + T_1 r + T_2 r^2 + \dots \quad .
\end{aligned}
\tag{4.54}$$

The regularity conditions follow by substituting these expansions into the radial equations (4.53) and requiring that the equations be satisfied at every order in r . The z_1 radial equation, at order r^{-1} gives immediately that

$$\alpha_0 = 0, \tag{4.55}$$

and the z_2 radial equation at order r^{-1} gives

$$\beta_0 = 0. \tag{4.56}$$

The equation for A at order r^0 gives

$$A_0 = 1, \tag{4.57}$$

so that at order r^0 , the z_1 equation becomes trivial, and the z_2 equation becomes

$$\beta_1 = 0. \tag{4.58}$$

Then at order r^1 , the equations for the geometric variables give

$$\begin{aligned}
A_1 &= 0 \\
T_1 &= 0,
\end{aligned}
\tag{4.59}$$

and the z_1 equation at order r^1 gives

$$\alpha_2 = 0. \tag{4.60}$$

The z_2 equation at order r^1 , on the other hand, gives

$$\beta_2 = \frac{1}{3}(\omega T_0 - m)\alpha_1. \tag{4.61}$$

Finally, at order r^2 , the equations for the geometric variables yield

$$\begin{aligned} A_2 &= -\frac{16}{3}\pi\omega T_0^2\alpha_1^2 \\ T_2 &= \frac{4}{3}\pi T_0^2\alpha_1^2(m - 2\omega T_0). \end{aligned} \tag{4.62}$$

In summary, we have the regularity conditions,

$$\begin{aligned} z_1(r) &= \alpha_1 r + O(r^3) \\ z_2(r) &= \frac{1}{3}(\omega T_0 - m)\alpha_1 r^2 + O(r^3) \\ A(r) &= 1 - \frac{16}{3}\pi\omega T_0^2\alpha_1^2 r^2 + O(r^3) \\ T(r) &= T_0 + \frac{4}{3}\pi T_0^2\alpha_1^2(m - 2\omega T_0) + O(r^3), \end{aligned} \tag{4.63}$$

where α_1 and T_0 are effectively free parameters. We use these equations to extend the solution to some finite $r > 0$ in order to begin the radial integration of eqs. (4.53). Notice that these equations are slightly different from those given in [12], but we found that both sets of regularity conditions give essentially identical solutions (with only slightly different parameter values).

In principle, to find static solutions, one must adjust the four parameters m , ω , T_0 , and α_1 until the integrated solution satisfies the three asymptotic

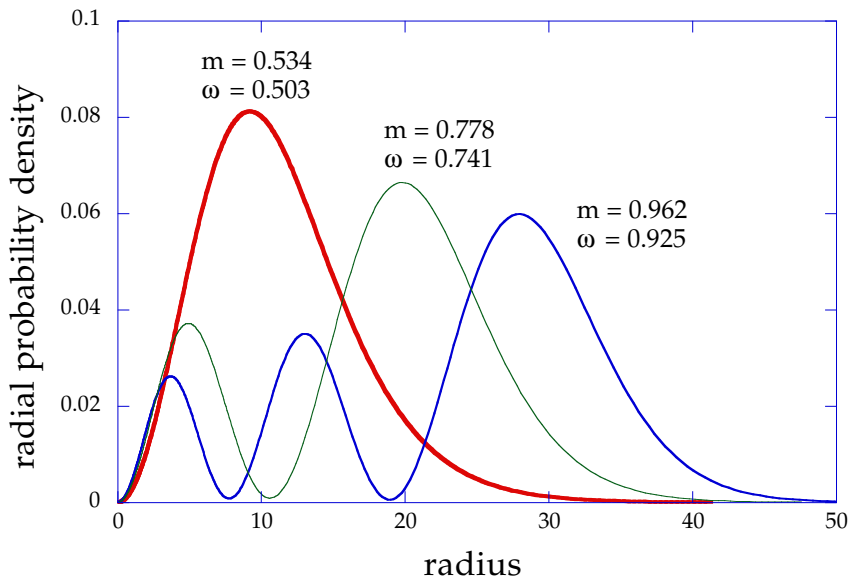


Figure 4.1: Three sample static solutions of the Einstein-Dirac field.

regularity conditions,

$$\begin{aligned}
 \lim_{r \rightarrow \infty} \int_0^r P(r') dr' &= 1 \\
 \lim_{r \rightarrow \infty} A(r) &= 1 \\
 \lim_{r \rightarrow \infty} T(r) &= 1.
 \end{aligned}
 \tag{4.64}$$

The first condition is, of course, the normalization condition. The second follows from requiring that the solution have finite ADM mass (recall that the mass aspect $m(t, r)$ is given by $2m/r = 1 - 1/a^2$). The third requirement is a consequence of requiring that the spacetime be asymptotically flat. However, it is in general quite difficult to perform a search in four parameters simultaneously, so FSY employed a *rescaling* approach to simplify the search. This

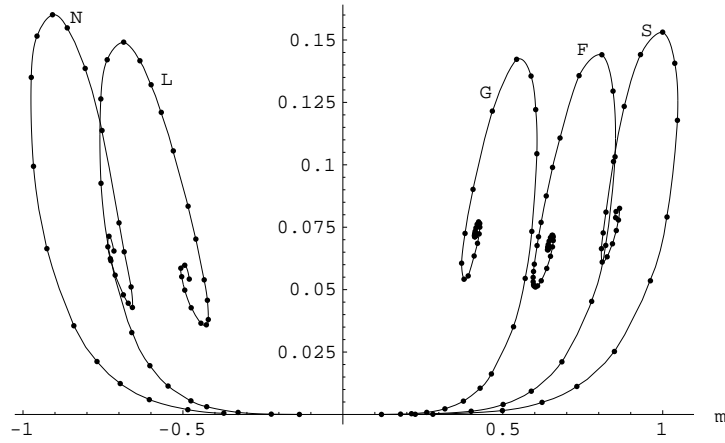


Figure 4.2: Plot of the binding energy $|m| - \omega$, showing spiral structures. This figure is reprinted from [12].

procedure essentially amounts to replacing (4.64) by the weaker conditions,

$$\begin{aligned}
 \lim_{r \rightarrow \infty} \int_0^r P(r') dr' &< \infty \\
 \lim_{r \rightarrow \infty} A(r) &= 1 \\
 \lim_{r \rightarrow \infty} T(r) &< \infty,
 \end{aligned}
 \tag{4.65}$$

and assuming arbitrary (but fixed) values for m and T_0 of 1. Then the rescaling parameters,

$$\begin{aligned}
 \lambda &= \lim_{r \rightarrow \infty} \int_0^r P(r') dr' \\
 \tau &= \lim_{r \rightarrow \infty} T(r)
 \end{aligned}
 \tag{4.66}$$

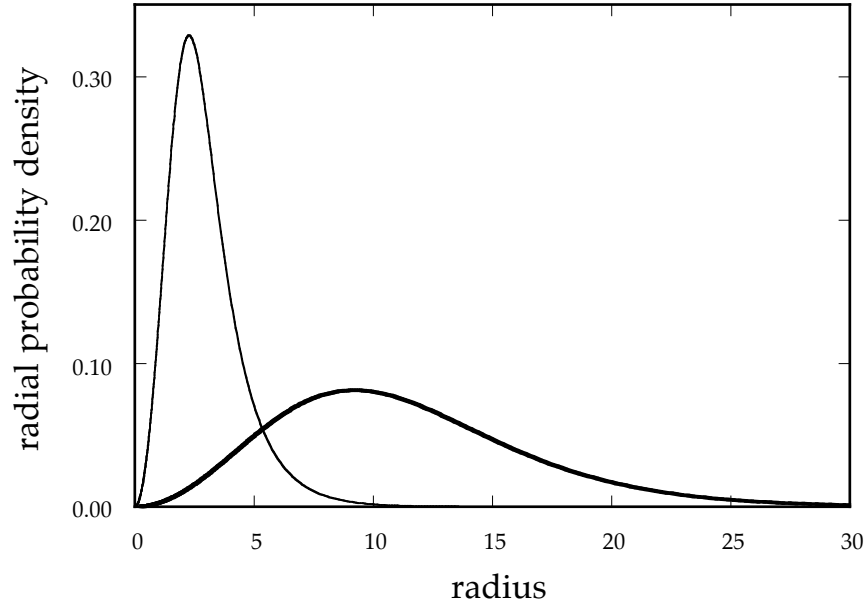


Figure 4.3: The two static solutions corresponding to $m = 0.534$. The solution shown in bold is a stable solution with $\omega = 0.503$, and is the same solution shown in Fig. 4.1. The other solution is unstable, with $\omega = 0.398$.

can be used to define rescaled functions

$$\begin{aligned}
 \tilde{z}_1(r) &\equiv \sqrt{\frac{\tau}{\lambda}} z_1(\lambda r) \\
 \tilde{z}_2(r) &\equiv \sqrt{\frac{\tau}{\lambda}} z_2(\lambda r) \\
 \tilde{A}(r) &\equiv A(\lambda r) \\
 \tilde{T}(r) &\equiv \tau^{-1} T(\lambda r).
 \end{aligned} \tag{4.67}$$

It can then be shown that these rescaled variables satisfy the proper constraints

(4.64), with the scaled parameters

$$\begin{aligned}\tilde{m} &\equiv \lambda m \\ \tilde{\omega} &\equiv \lambda \tau \omega.\end{aligned}\tag{4.68}$$

Hence, these rescaled solutions correspond to physically reasonable solutions. This rescaling procedure is essential to finding these solutions, because it effectively reduces the problem of finding static solutions to a parameter search in only one parameter.

In practice, the value of α_1 is set to some value, and then the value of ω is adjusted until the conditions (4.65) are satisfied. This can be conveniently accomplished by monitoring one of the matter variables and adjusting ω until it is forced to zero at large r (on either side of the critical parameter value, the variable will tend to go to positive or negative infinity, so this technique lends itself well to a bisection search). Because the matter content of the field drops to zero at large r , the three (weak) conditions are automatically satisfied. Generally speaking, at each value of α_1 , there is a discrete infinity of solutions that can be indexed by the number of zero-crossings in the matter variables. Notice that in this rescaling procedure, α_1 appears as a free parameter, so it can be used to generate a continuous infinity of solutions.

The probability densities of some sample static solutions are shown in Fig. 4.1, corresponding to $\alpha_1 = 0.02$ (before rescaling). The “ground state” solution (the one-peak distribution) corresponds to an unscaled ω of about 1.071 and scaled parameters $m = 0.534$ and $\omega = 0.503$. The “first excited state” solution (two-peaked distribution) corresponds to an unscaled ω of about 1.095 and scaled parameters $m = 0.778$ and $\omega = 0.741$. Finally, the “second excited state” solution (three-peaked distribution) corresponds to an unscaled ω of about 1.107 and scaled parameters $m = 0.962$ and $\omega = 0.924$. One side effect

of using the rescaling procedure is that it is somewhat difficult to predict what mass or frequency the solution will have, so if one desires a solution with a particular mass (for example, to compare with a dynamical simulation), then it is necessary to do a search in α_1 until the desired rescaled mass is found.

Fig. 4.2 is a plot reprinted from [12] that shows the “binding energy” $|m| - \omega$ for the solutions. In the plot, the curves corresponding to the ground, first excited, and second excited states are labelled by G, F, and S, respectively, whereas L and N label the corresponding *negative* mass states. FSY found that the binding energy is always positive, so that the solutions correspond to bound states. Additionally, they observe that any particular state exists over only a bounded interval of mass, and that the binding energy curves exhibit a self-similar spiral structure that appears to approach a limit point. FSY also carried out a stability analysis of the solutions, and their results can be summarized in Fig. 4.2 as follows: if the spiral curves are viewed as parameterized by α_1 beginning at the origin and initially travelling away from the origin, then the solutions are stable when the curve is moving away from the origin (along the m axis), and they are unstable otherwise (e.g. the small mass solutions are stable).

Fig. 4.3 shows the two solutions corresponding to $m = 0.534$. From Fig. 4.2, it is clear that one of these solutions is stable, whereas the other is unstable. The stable solution is shown in bold, and is the same as the ground state solution plotted in Fig. 4.1. The other solution is the unstable static solution. Note that to find this unstable static solution, it was necessary to have the automatic bisection-search code described below in order to quickly find static solutions; to find the other solution corresponding to the specific mass $m = 0.534$, it was necessary to adjust the parameter α_1 until the rescaled

mass of the resulting static solution had the correct value.

4.1.5 Code description

Our static-solution solver consists of three FORTRAN programs. The first uses the LSODA ODE solver (which is one component of the Lawrence Livermore National Laboratory ODEPACK package) to integrate the radial differential equations (4.53), using the “starting” procedure described above. When this program successfully integrates the equations to the user-specified final radius, it outputs the scaling parameters λ and τ . The rescaling of parameters is then performed by the second program which takes these rescaling parameters as input, integrates the equations again, and writes the rescaled solution to standard output. The final program is effectively a combination of the above two “manual” programs, which allows the user to specify two boundaries for ω . This program then performs a bisection search by monitoring the sign of z_1 at the final integration time in order to force z_1 to zero at large r . To perform the bisection properly, the program takes an integer “polarity” input of either 1 or -1 that can invert the decision strategy for the bisection. After the bisection is completed, the program computes the rescaling parameters, dumps the scaled solution to standard output, and prints the unscaled and scaled parameters to standard error.

4.1.6 Code testing

Prior to making our “production runs,” we convergence tested the unigrid code by performing one run, using the nonpropagating “centered” initial data (4.31), at each of three levels of discretization, $\Delta r = h, 2h$, and $4h$. The value of δ was chosen to produce a subcritical evolution. We evaluated

the convergence of the numerical solution by plotting $d\hat{p}/dr|_{4h} - d\hat{p}/dr|_{2h}$ and merging this plot with a plot of $4(d\hat{p}/dr|_{2h} - d\hat{p}/dr|_h)$. The variable P is the probability density defined earlier (4.18). As expected, the two waveforms coincided throughout the evolution as seen in Fig. 4.4. This shows that our discrete solution converges to the continuum solution with $O(h^2)$ accuracy.

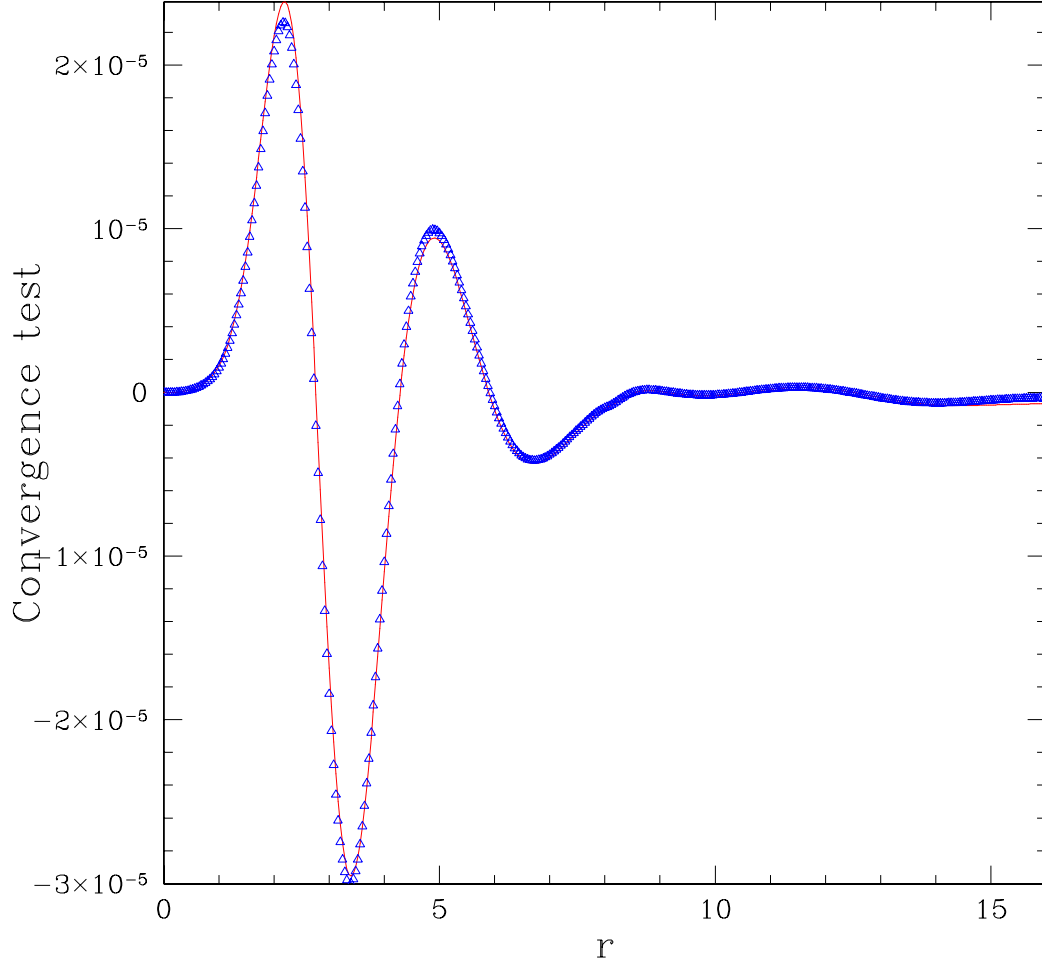


Figure 4.4: This is a convergence test with the function, $d\hat{p}/dr$, the spatial derivative of the probability density. The system (with $m = 0.534$) is solved on a uniform grid at three different levels of discretization: $\Delta r = h, 2h$, and $4h$. The solid line is $4(d\hat{p}/dr|_{2h} - d\hat{p}/dr|_h)$ and the triangles show $d\hat{p}/dr|_{4h} - d\hat{p}/dr|_{2h}$. Our discrete solution converges to the continuum solution with $O(h^2)$ accuracy. We display the convergence test here at a single time.

4.2 Data and results

Although we described two types of initial data families above, we were successful in obtaining meaningful results only while using the stationary centered data family. This is because all attempts to use propagating initial data apparently violated the regularity conditions (4.63) severely enough to cause significant unphysical oscillations of the geometric variables near the origin. To avoid this problem it is necessary to make both the real and imaginary components of z_1 *odd* with respect to the origin, while making the real and imaginary components of z_2 *even* with respect to the origin. This must be done while simultaneously preserving the phase relationship needed to produce propagating waves (4.33), which requires that $\text{Re}z_1$ and $\text{Im}z_2$ be in phase while $\text{Im}z_1$ leads both by $\pi/2$ and $\text{Re}z_2$ lags both by $\pi/2$. We tried several approaches to solving this problem, including manipulation of the two inner-most grid points, but without success. We also considered using Bessel functions multiplied by powers of r , which meet all the requirements above, but which do not asymptote to the same power of r at large r . Fortunately, the initially stationary data family produced a wealth of critical points and stable solutions for us to study. Such regularity and phase issues were not a problem for the reformulated, massless case presented in Chapter 5.

4.2.1 Moderate mass regime ($m = 0.534$)

In the $m = 0.534$ case there are two static solutions, one stable and one unstable, as shown in Fig. 4.3. Near the critical parameter value we observed a logarithmic scaling for the time it took to form a black hole.

In the marginally supercritical case (where $\delta^* - \delta \approx 10^{-15}$), the wave packet is an unstable, oscillating solution that persists for some time and then

suddenly collapses to form a black hole. The unstable, oscillating solution appears to be similar to the unstable, static solution found by the static solver. In the marginally subcritical case (where $\delta - \delta^* \approx 10^{-15}$), the wave packet again persists near the same oscillating, unstable solution for some time, but then suddenly disperses.

In both of these cases, another characteristic of the Dirac field is evident: *Zitterbewegung* (literally, “quivering motion”), which is apparent as a fast jittering motion that appears along with the slower motion of the wave packet. This jittering motion is a result of the interference between the positive and negative energy components of the wave packet [4]. A plot of the maximum value of $2M/r$ over time for the marginally subcritical evolution displaying these oscillations is shown in Fig. 4.5. This exponent is presumably the inverse Lyapunov exponent of the single unstable mode of the critical solution.

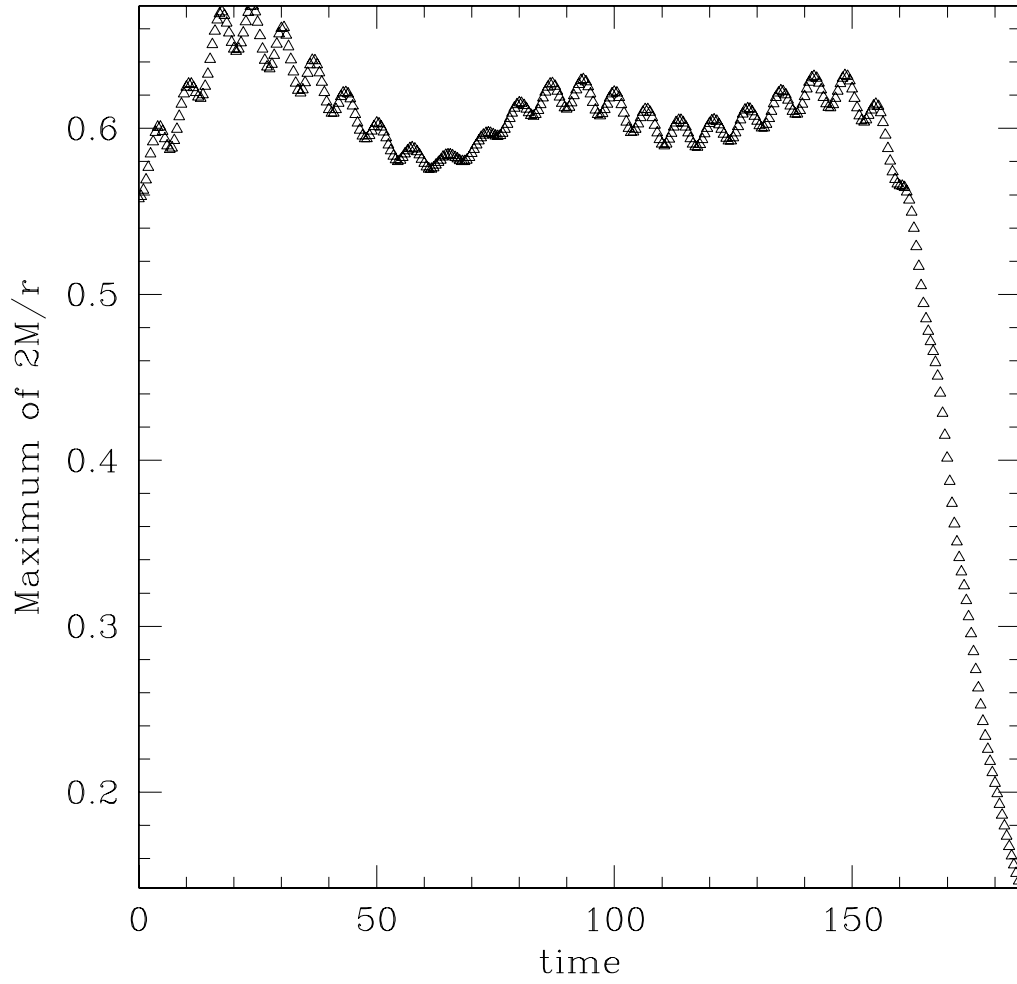


Figure 4.5: A plot of the maximum value of $2M/r$ vs. time for a marginally subcritical evolution displaying *Zitterbewegung*.

We also observed scaling behavior in the time to form a black hole. For this observation we measured the proper time for an observer at infinity from the initial state until the simulation halted just before black hole formation. Our results are displayed in Fig. 4.6, showing logarithmic scaling of the formation time. The fitted slope in this case was -4.8 ± 0.0007 (where the quoted uncertainty only represents uncertainty in the linear fit).

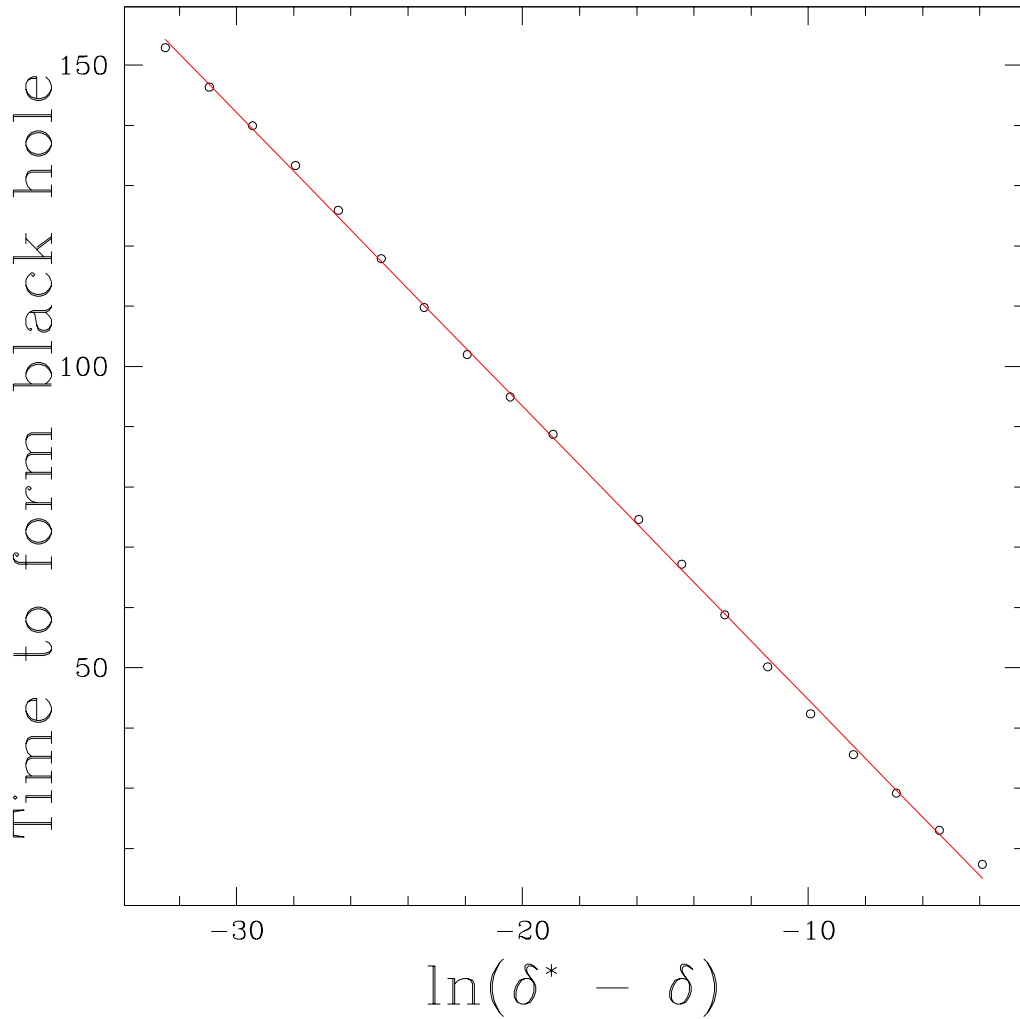


Figure 4.6: Logarithmic scaling of the time to form a black hole near the critical parameter for $m = 0.534$. The slope of the fitted line is -4.8 ± 0.0007 (the quoted uncertainty only represents uncertainty in the linear fit).

4.2.2 Low mass regime ($m = 0.250$)

We first consider the initial family (4.31) in the small-mass regime, with $m = 0.25$. As is evident from Fig. 4.2, there is only one stable, static solution in this case. The absence of unstable static solutions suggests that the critical behavior will be Type II, and indeed this is what we observe. There is a scaling behavior of the black hole mass as a function of $\delta^* - \delta$, shown in Fig. 4.7. We observe power-law scaling, as expected for Type II behavior.

$$M_{bh} \propto |\delta^* - \delta|^\lambda. \quad (4.69)$$

Our measured exponent is 0.27. We measured the mass in the usual way by measuring the radius R_{BH} where the “black hole” function $2M/r$ crossed some threshold near 1 (typically 0.99), and using $2M/r = 1$.

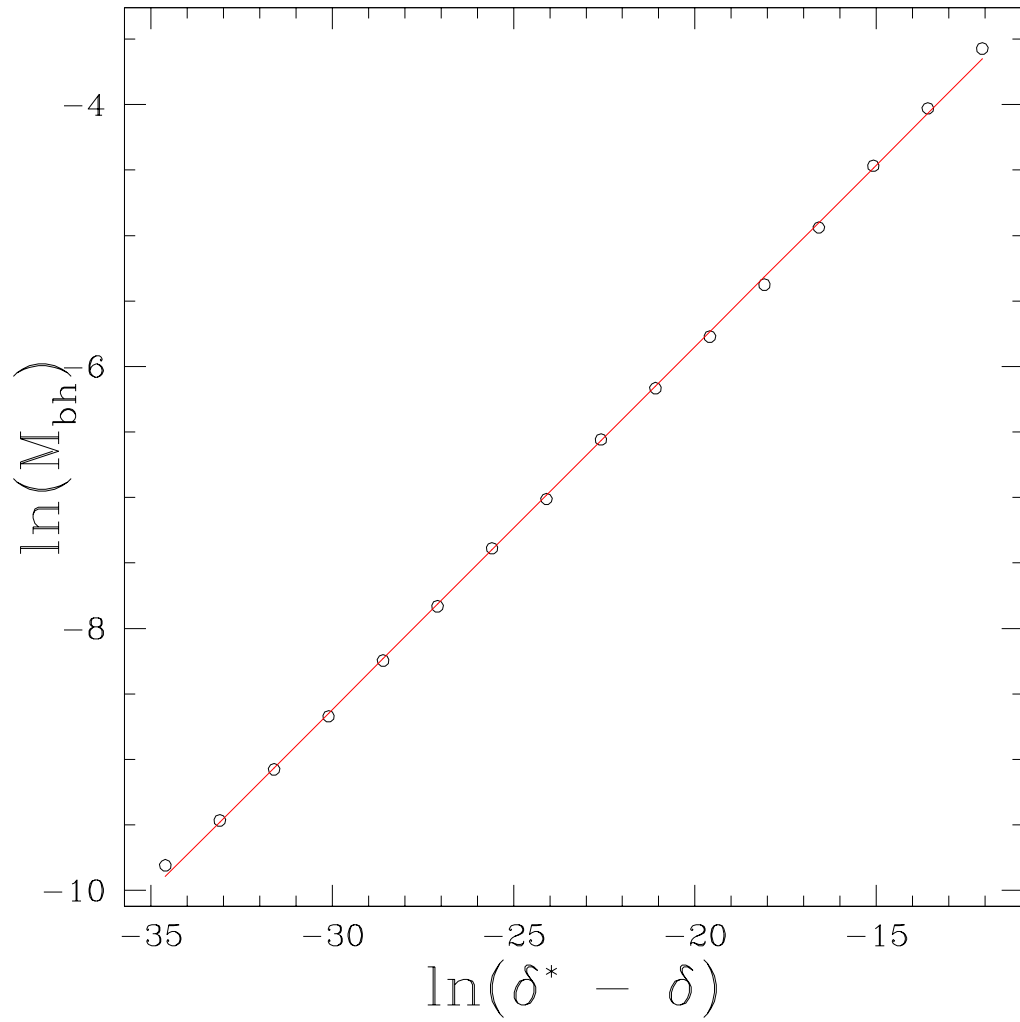


Figure 4.7: Scaling behavior of the black hole mass near the critical parameter for $m = 0.25$. The slope of the fitted line is 0.27. This scaling of the mass is characteristic of Type II critical behavior.

Chapter 5

Einstein-Massless-Dirac System

5.1 Introduction

In Chapter 4 it was shown that there is interesting behavior at the threshold of black hole formation for the massive Einstein-Dirac system as the mass of the field is decreased. There is a scaling law (see Fig. 4.7) for the black hole mass, M_{bh} , similar to the one first discovered by Choptuik [8]. In the original investigation by Choptuik, the model used to investigate the behavior at the threshold of black hole formation was a spherically symmetric, massless scalar field minimally coupled to gravity. Initial data consisting of a pulse of scalar field was parameterized by a single quantity, p . This parameter could represent the amplitude of the pulse (this pulse could be a gaussian function of the radius, r , which in spherical symmetry represents an entire spherical shell of scalar field). The parameter p controls the initial amount of mass-energy in the spacetime. For simplicity, we will define p so that increasing it means increasing the initial amount of mass-energy. When it is sufficiently increased the evolution results in the formation of a black hole. It can also be given a lower value that causes the scalar field to evolve to some other end state which is not a black hole. For the massless system, this other scenario is a dispersal to spatial infinity leaving behind flat spacetime. When a value of the parameter is found which results in black hole formation we say that it is *supercritical*. When a value is found which doesn't produce a black hole (but

produces the other end state) it is called *subcritical*. The parameter p is then tuned until its critical value p^* is found. This critical value is such that a small positive perturbation will result in gravitational collapse while a small negative perturbation will result in the other end state. In probing the threshold of black hole formation Choptuik found that there is a power law scaling for length scales. Tuning arbitrarily close to p^* means that black holes of arbitrarily small mass could be created. Another feature of these threshold solutions is that the scaling exponent for this power law is universal. The same exponent will be found regardless of the family of initial data or which parameter is used. This amazing result can be explained through perturbation analysis in which the critical solution is shown to have a single unstable mode. The two competing end states (black hole formation or not) are this one unstable mode. Therefore by “tuning away” this mode one is left with the critical solution. When p is tuned arbitrarily close to the critical parameter, p^* , the critical solution will persist for an arbitrarily long time. All of this interesting behavior falls under the classification of *critical phenomena*.

Since then, other systems have been studied for critical phenomena such as collapsing gravitational waves, perfect fluids, Yang-Mills fields, massive and complex scalar fields, scalar fields in anti-de Sitter spacetime (for a review see [16]) and collisionless matter [20]. We will be investigating another field model, namely massless spin- $\frac{1}{2}$ fields coupled to gravity.

The chapter is organized as follows: a brief introduction to spinors is given followed by the derivation of the equations of motion and the Einstein equations for the metric components. The numerical method used for solving the partial differential equations (PDEs) is discussed as well as the results found. Next a self-similar ansatz is taken and a change of coordinates

is performed on the system to reduce the PDEs to a set of ordinary differential equations (ODEs). The shooting method used to solve this new set of equations is discussed and the results are compared to those found from the PDEs.

5.2 Formalism

We consider a spherically symmetric system of spin- $\frac{1}{2}$ fields. Since the distribution of the field's mass-energy is spherically symmetric, so is the spacetime geometry it produces. We again using the ADM formalism and express the metric in polar-areal coordinates.

$$ds^2 = -\alpha(t, r)^2 dt^2 + a(t, r)^2 dr^2 + r^2 d\theta^2 + r^2 \sin^2 \theta d\phi^2. \quad (5.1)$$

Before discussing how we will separate the radial and angular dependences in our system and form a spin singlet, let us begin with a brief introduction to spinors (see [6], [25], and [3]). The evolution of a massless, spin- $\frac{1}{2}$ field coupled to gravity is governed by the curved space Dirac equation:

$$\gamma^\mu \nabla_\mu \psi = 0. \quad (5.2)$$

The curved space γ -matrices, γ^μ , are determined by:

$$g^{\mu\nu} \mathbb{1} = \frac{1}{2} \{\gamma^\mu, \gamma^\nu\} \quad (5.3)$$

where $\mathbb{1}$ is the 4×4 identity matrix and $g^{\mu\nu}$ is the inverse metric. In flat spacetime, we have:

$$\eta^{ab} \mathbb{1} = \frac{1}{2} \{\tilde{\gamma}^a, \tilde{\gamma}^b\}. \quad (5.4)$$

A particular choice of $\tilde{\gamma}^a$ which satisfy (5.4) in our signature $(-, +, +, +)$ is:

$$\tilde{\gamma}^0 = i \begin{pmatrix} \mathbb{1} & 0 \\ 0 & -\mathbb{1} \end{pmatrix}, \quad \tilde{\gamma}^j = i \begin{pmatrix} 0 & \sigma^j \\ -\sigma^j & 0 \end{pmatrix}. \quad (5.5)$$

The index $j = 1, 2, 3$ and the σ^j :

$$\sigma^1 = \begin{pmatrix} 0 & 1 \\ 1 & 0 \end{pmatrix}, \sigma^2 = \begin{pmatrix} 0 & -i \\ i & 0 \end{pmatrix}, \sigma^3 = \begin{pmatrix} 1 & 0 \\ 0 & -1 \end{pmatrix}, \quad (5.6)$$

are the Pauli spin matrices. The general γ -matrices are related to their flat, cartesian counterparts by

$$\gamma^\mu = V_a{}^\mu \tilde{\gamma}^a \quad (5.7)$$

where there is an implied summation over the “flat”, Latin index a . The $V_a{}^\mu$ are called vierbein.

The derivative operator in equation (5.2) is a *spinor* covariant derivative with spinor affine connections, Γ_μ . It acts in the following way on spinors,

$$\nabla_\mu \psi = \left(\frac{\partial}{\partial x^\mu} - \Gamma_\mu \right) \psi, \quad (5.8)$$

and γ -matrices,

$$\nabla_\mu \gamma^\nu = \frac{\partial}{\partial x^\mu} \gamma^\nu + \Gamma^\nu{}_{\mu\lambda} \gamma^\lambda - \Gamma_\mu \gamma^\nu + \gamma^\nu \Gamma_\mu. \quad (5.9)$$

However, it reduces to the usual covariant derivative when acting on tensors.

We choose the spinor connections to obey

$$\nabla_\mu \gamma^\nu = 0. \quad (5.10)$$

They take the form

$$\Gamma_\mu = -\frac{1}{8} [\tilde{\gamma}^a, \tilde{\gamma}^b] V_a{}^\nu \nabla_\mu V_{b\nu}. \quad (5.11)$$

When taking the covariant derivative of the vierbein above, only one Christoffel connection appears since there is only one curved, tensor index.

5.2.1 Representation

Now that we have chosen the form of our metric (5.1), we are ready to find a set of γ -matrices that satisfy equation (5.3). We choose as our representation:

$$\begin{aligned}\gamma^t &= \frac{\tilde{\gamma}^0}{\alpha}, & \gamma^r &= \frac{\tilde{\gamma}^3}{a}, \\ \gamma^\theta &= \frac{\tilde{\gamma}^2}{r}, & \gamma^\phi &= \frac{\tilde{\gamma}^1}{r \sin \theta}.\end{aligned}\tag{5.12}$$

This yields the following spinor connections:

$$\begin{aligned}\Gamma_t &= \frac{1}{2} \frac{\alpha'}{a} \tilde{\gamma}^0 \tilde{\gamma}^3 \\ \Gamma_r &= \frac{1}{2} \frac{\dot{a}}{\alpha} \tilde{\gamma}^0 \tilde{\gamma}^3 \\ \Gamma_\theta &= \frac{1}{2} \frac{1}{a} \tilde{\gamma}^3 \tilde{\gamma}^2 \\ \Gamma_\phi &= \frac{1}{2} \frac{\sin \theta}{a} \tilde{\gamma}^3 \tilde{\gamma}^1 + \frac{1}{2} \cos \theta \tilde{\gamma}^2 \tilde{\gamma}^1.\end{aligned}\tag{5.13}$$

Note that we have complete freedom to choose any set of γ^μ we wish provided they satisfy equation (5.3). Our specific choice is made so that the Dirac equation can be easily separated into radial and angular equations.

Before separating the equation, let us first simplify matters by using the fact that we are dealing with a massless spin- $\frac{1}{2}$ field. Mathematically, such fields have a particular chirality (circular polarization). We will adopt left-handed chirality which is expressed as:

$$(\mathbb{1} - i\gamma^5) \psi = 0\tag{5.14}$$

where γ^5 is defined by

$$\gamma^5 \equiv \tilde{\gamma}^0 \tilde{\gamma}^1 \tilde{\gamma}^2 \tilde{\gamma}^3.\tag{5.15}$$

Equation (5.14) can be satisfied by taking

$$\psi = \begin{pmatrix} \psi_1(t, r, \theta, \phi) \\ \psi_2(t, r, \theta, \phi) \\ \psi_1(t, r, \theta, \phi) \\ \psi_2(t, r, \theta, \phi) \end{pmatrix}. \quad (5.16)$$

Substituting this spinor into equation (5.2) yields two identical sets of equations each coupling the spinor components, ψ_1 and ψ_2 . We, of course, only need to solve one set of equations for these variables so we are left with two equations instead of the original four.

We will now perform a separation of variables on the spinor components:

$$\begin{pmatrix} \psi_1(t, r, \theta, \phi) \\ \psi_2(t, r, \theta, \phi) \end{pmatrix} = \frac{1}{r\sqrt{a(t, r)}} \begin{pmatrix} F(t, r)H_1(\theta, \phi) \\ G(t, r)H_2(\theta, \phi) \end{pmatrix}. \quad (5.17)$$

These new variables and a convenient choice of representation (5.12) allow the Dirac equation to be separated into a part that depends on (t, r) and a part that depends on (θ, ϕ) :

$$\frac{ir}{\alpha} \begin{pmatrix} \dot{F}/G \\ \dot{G}/F \end{pmatrix} + \frac{ir}{2} \frac{a'}{a^2} \begin{pmatrix} -F/G \\ G/F \end{pmatrix} + \frac{ir}{a} \begin{pmatrix} F'/G \\ G'/F \end{pmatrix} + \frac{ir}{2} \frac{\alpha'}{\alpha a} \begin{pmatrix} F/G \\ -G/F \end{pmatrix} \quad (5.18)$$

$$+ \frac{i}{\sin \theta} \begin{pmatrix} H_{2,\phi}/H_1 \\ H_{1,\phi}/H_2 \end{pmatrix} + \begin{pmatrix} H_{2,\theta}/H_1 \\ -H_{1,\theta}/H_2 \end{pmatrix} + \frac{1}{2} \cot \theta \begin{pmatrix} H_2/H_1 \\ -H_1/H_2 \end{pmatrix} = 0.$$

Although the factor involving r and $a(t, r)$ in (5.17) is not necessary for this separation of variables, it has simplified things by removing some terms in equation (5.18). Of particular importance is the elimination of a time derivative of $a(t, r)$ which would make the solution of our system more complicated.

Let us look at our separated equation. Since any change in θ or ϕ cannot change the value of the (t, r) part of (5.18), the (θ, ϕ) part must be a constant.

At this point, if our goal was to simply remove the angular dependence from the Dirac equation, we would be done. By replacing the angular part of (5.18) by a constant we would be restricting ourselves to some spinor that is an eigenfunction of the angular operators in the Dirac equation. In fact only one of its eigenvalues, rather than the precise form of the angular eigenfunction, would need to be known. However, our goal is not only to eliminate the angular dependence of our equation of motion, but also to have a matter source which generates a spherically symmetric spacetime. An individual spinor is *not* a spherically symmetric object (it always has a spin-angular momentum which breaks this symmetry) and therefore cannot by itself produce such a spacetime. What we require are multiple spinors where all the individual spin-angular momenta counterbalance each other so the system has no net spin. We will use two spinors, for simplicity, but any even number of the appropriate spinors will do. The spherically symmetric stress-energy tensor for the system, $T_{\mu\nu}$, is found from the sum of the stress-energy tensors of the individual spinor fields [24].

$$T_{\mu\nu} = T_{\mu\nu}^+ + T_{\mu\nu}^- \quad (5.19)$$

Evaluating the right hand side of equation (5.19) *does* require the angular eigenfunctions which we will now compute.

5.2.2 Equations of Motion

Setting the angular part of equation (5.18) equal to a constant, n , gives:

$$\left[-\frac{i}{\sin\theta} \frac{\partial}{\partial\phi} - \frac{\partial}{\partial\theta} - \frac{1}{2} \cot\theta \right] H_2 = -nH_1 \quad (5.20)$$

$$\left[\frac{i}{\sin\theta} \frac{\partial}{\partial\phi} - \frac{\partial}{\partial\theta} - \frac{1}{2} \cot\theta \right] H_1 = nH_2. \quad (5.21)$$

We have multiplied (5.20) by $-H_1$ and (5.21) by H_2 so that the terms in brackets are the raising and lowering operators, \eth (eth) and \ethbar (ethbar), respectively. These operators act on spin weighted spherical harmonics (see [21] and [14]) in the following way:

$$\eth({}_s Y_{lm}) = \sqrt{(l-s)(l+s+1)}({}_{s+1} Y_{lm}) \quad (5.22)$$

$$\ethbar({}_s Y_{lm}) = -\sqrt{(l+s)(l-s+1)}({}_{s-1} Y_{lm}). \quad (5.23)$$

Our functions H_1 and H_2 have the spin weights $s = \pm\frac{1}{2}$:

$$H_1(\theta, \phi) = {}_{\frac{1}{2}} Y_{lm}(\theta, \phi) \quad (5.24)$$

$$H_2(\theta, \phi) = {}_{-\frac{1}{2}} Y_{lm}(\theta, \phi). \quad (5.25)$$

We do not need to solve equations (5.20) and (5.21) in generality; i.e. for any values of l or m . To form a spin singlet, all we require is one spinor constructed from ${}_{\frac{1}{2}} Y_{\frac{1}{2}\frac{1}{2}}$, ${}_{\frac{1}{2}} Y_{\frac{1}{2}-\frac{1}{2}}$ and one spinor from ${}_{-\frac{1}{2}} Y_{\frac{1}{2}\frac{1}{2}}$, ${}_{-\frac{1}{2}} Y_{\frac{1}{2}-\frac{1}{2}}$. We can find these spinor harmonics by taking advantage of the fact that the right hand sides of (5.22) and (5.23) vanish for $l = s$ and $l = -s$, respectively. This uncoupled set of first order differential equations has the solutions:

$$\begin{aligned} {}_{\frac{1}{2}} Y_{\frac{1}{2}\frac{1}{2}} &= \frac{1}{\sqrt{2\pi}} e^{i\phi/2} \sin \frac{\theta}{2} \\ {}_{\frac{1}{2}} Y_{\frac{1}{2}-\frac{1}{2}} &= \frac{1}{\sqrt{2\pi}} e^{-i\phi/2} \cos \frac{\theta}{2} \\ {}_{-\frac{1}{2}} Y_{\frac{1}{2}\frac{1}{2}} &= \frac{1}{\sqrt{2\pi}} e^{i\phi/2} \cos \frac{\theta}{2} \\ {}_{-\frac{1}{2}} Y_{\frac{1}{2}-\frac{1}{2}} &= -\frac{1}{\sqrt{2\pi}} e^{-i\phi/2} \sin \frac{\theta}{2} \end{aligned} \quad (5.26)$$

for our desired values of s, l , and m . We have for our two spinor fields:

$$\psi^+ = \frac{1}{2\sqrt{\pi}} \frac{e^{i\phi/2}}{r\sqrt{a(t,r)}} \begin{pmatrix} F(t,r) \sin(\theta/2) \\ G(t,r) \cos(\theta/2) \\ F(t,r) \sin(\theta/2) \\ G(t,r) \cos(\theta/2) \end{pmatrix} \quad (5.27)$$

$$\psi^- = \frac{1}{2\sqrt{\pi}} \frac{e^{-i\phi/2}}{r\sqrt{a(t,r)}} \begin{pmatrix} F(t,r) \cos(\theta/2) \\ -G(t,r) \sin(\theta/2) \\ F(t,r) \cos(\theta/2) \\ -G(t,r) \sin(\theta/2) \end{pmatrix}. \quad (5.28)$$

Our radial equations of motion now take the form:

$$\dot{F}_1 = -\sqrt{\frac{\alpha}{a}} \partial_r \left(\sqrt{\frac{\alpha}{a}} F_1 \right) + \frac{\alpha}{r} G_2 \quad (5.29)$$

$$\dot{G}_1 = \sqrt{\frac{\alpha}{a}} \partial_r \left(\sqrt{\frac{\alpha}{a}} G_1 \right) + \frac{\alpha}{r} F_2 \quad (5.30)$$

$$\dot{F}_2 = -\sqrt{\frac{\alpha}{a}} \partial_r \left(\sqrt{\frac{\alpha}{a}} F_2 \right) - \frac{\alpha}{r} G_1 \quad (5.31)$$

$$\dot{G}_2 = \sqrt{\frac{\alpha}{a}} \partial_r \left(\sqrt{\frac{\alpha}{a}} G_2 \right) - \frac{\alpha}{r} F_1 \quad (5.32)$$

where we have written the complex functions in terms of real functions, $F = F_1 + iF_2$ and $G = G_1 + iG_2$. Notice that this is the same radial equation found in Chapter 4 in the limit where m tends to 0 and the following identification is made:

$$\begin{aligned} F_1 + G_2 &= \operatorname{Re} z_1 \\ G_2 - F_1 &= \operatorname{Im} z_2 \\ F_2 - G_1 &= \operatorname{Im} z_1 \\ F_2 + G_1 &= \operatorname{Re} z_2 \end{aligned} \quad (5.33)$$

5.2.3 Geometry

Although the spinors (5.27) and (5.28) both yield the same radial equations of motion (5.29)-(5.32), they have different stress-energy tensors. We

calculate the stress-tensor for each field individually using:

$$T_{\mu\nu} = -\frac{1}{2} [\bar{\psi} \gamma_{(\mu} \nabla_{\nu)} \psi - (\nabla_{(\mu} \bar{\psi}) \gamma_{\nu)} \psi] \quad (5.34)$$

where the Dirac adjoint of ψ is defined as:

$$\bar{\psi} = \psi^\dagger A$$

and A is the Hermitizing matrix. This matrix is needed so that real-valued expressions (such as the current density or in this case the stress-energy tensor) can be computed using the complex-valued spinors. It is chosen so that both A and $iA\gamma^\mu$ are Hermitian. We will take $A = -i\tilde{\gamma}^0$.

Computing $T_{\mu\nu}$ for each spinor (5.27),(5.28) and summing them (5.19) yields the spherically symmetric stress-energy tensor:

$$\begin{aligned} T_{tt} &= \frac{\alpha}{2\pi r^2 a} \left(\dot{F}_1 F_2 - F_1 \dot{F}_2 + \dot{G}_1 G_2 - G_1 \dot{G}_2 \right) \\ T_{tr} &= \frac{1}{4\pi r^2} \left[F_1 \dot{F}_2 - \dot{F}_1 F_2 + \dot{G}_1 G_2 - G_1 \dot{G}_2 + \frac{\alpha}{a} (F_1' F_2 - F_1 F_2' + G_1' G_2 - G_1 G_2') \right] \\ T_{rr} &= \frac{1}{2\pi r^2} (F_1 F_2' - F_1' F_2 + G_1' G_2 - G_1 G_2') \\ T_{\theta\theta} &= \frac{1}{2\pi r a} (F_1 G_1 + F_2 G_2) \\ T_{\phi\phi} &= \frac{\sin^2 \theta}{2\pi r a} (F_1 G_1 + F_2 G_2). \end{aligned} \quad (5.35)$$

Contracting the stress-energy tensor gives:

$$T_\mu{}^\mu = 0 \quad (5.36)$$

which is expected since the massless Dirac system is conformally invariant. Now that we have a stress-energy tensor that will generate a spherically symmetric spacetime, we are ready to write down Einstein's equations which will be solved for α and a .

Due to our choice of coordinates, a sufficient set of Einstein's equations to fix α and a are the Hamiltonian constraint and the slicing condition. The *Hamiltonian constraint* is:

$$\frac{a'}{a} + \frac{a^2 - 1}{2r} = \frac{2}{r^2} (2aF_1G_1 + 2aF_2G_2 + rF_1F_2' - rF_1'F_2 + rG_1'G_2 - rG_1G_2') \quad (5.37)$$

and is treated as an equation for a . We note that the *momentum constraint*:

$$\dot{a} = \frac{2\alpha}{r} (F_1'F_2 - F_1F_2' + G_1'G_2 - G_1G_2'). \quad (5.38)$$

also yields an equation for a (an evolution equation) that we will use as a means to check the consistency of our equations. In both equations (5.37) and (5.38), time derivatives of F 's and G 's have been replaced using the equations of motion (5.29)-(5.32).

The slicing condition, which fixes α , is derived from the evolution equation for K^θ_θ and the fact that for polar slicing

$$K = K^i_i = K^r_r + 2K^\theta_\theta = K^r_r$$

since $K^\theta_\theta = 0$. To maintain $K^\theta_\theta = 0$ for all time, we impose $\dot{K}^\theta_\theta = 0$, this then yields:

$$\frac{\alpha'}{\alpha} - \frac{a^2 - 1}{2r} = \frac{2}{r} (F_1F_2' - F_1'F_2 + G_1'G_2 - G_1G_2'). \quad (5.39)$$

5.3 Numerics and Results

The above equations of motion were solved using a Crank-Nicholson update scheme, standard $O(h^2)$ spatial derivatives, and Berger-Oliger style adaptive mesh refinement (see [2]). To achieve stability, high frequency modes

were damped using Kreiss-Oliger dissipation [19]. At $r = 0$, the following regularity conditions were enforced:

$$\begin{aligned}
F_1(t, 0) &= 0 \\
F_2(t, 0) &= 0 \\
G_1(t, 0) &= 0 \\
G_2(t, 0) &= 0.
\end{aligned}
\tag{5.40}$$

An outgoing wave condition was used as the outer boundary condition for these fields.

$$\begin{aligned}
\partial_t F_1 &= -\partial_r F_1 \\
\partial_t F_2 &= -\partial_r F_2 \\
\partial_t G_1 &= -\partial_r G_1 \\
\partial_t G_2 &= -\partial_r G_2.
\end{aligned}
\tag{5.41}$$

We also have

$$a(t, 0) = 1. \tag{5.42}$$

which follows from the demand of regularity (local flatness) at $r = 0$. At each time step, the Hamiltonian constraint is integrated outwards using Newton's method. Before solving the slicing condition (5.39), we notice that our equations are invariant under rescalings of α . We will therefore use the fact that $\alpha = 1/a$ (this can be seen by comparing (5.1) to the Schwarzschild metric) to find α at the outer boundary and then integrate inwards. We could have simply chosen $\alpha(t, 0) = 1$ and integrated outwards, however, but (5.39) indicates that α is a monotonically increasing function. If we took $\alpha(t, 0) = 1$, then it could become quite large at the outer boundary. This would affect the characteristics of our hyperbolic equation of motion in this region and would

require a very small Courant factor in order to maintain stability. By first solving for a , then using it to find α at the outer boundary, we can integrate inwards to get a smaller α on the grid.

Two families of initial data were used: gaussians and kinks. In both cases, the initial data was such that the pulses were initially ingoing and had positive energy by construction.

$$F_1 = 0$$

$$F_2 = 0$$

$$G_1 = p * e^{-(r-r_0)^2/4*\delta^2}$$

$$G_2 = p * e^{-(r-r_0+\delta)^2/4*\delta^2}$$

Each family was characterized by a single parameter, p , which controlled whether the mass-energy of the system would collapse and form a black hole or if it would implode through the center ($r = 0$) and disperse to spatial infinity. As p is tuned to the threshold between collapse and dispersal, the unstable mode is “tuned away” to reveal a self-similar solution. The scale invariant quantity, a , displayed continuous self-similarity (CSS) which can be seen in Fig. 5.3. The Dirac fields were discretely self-similar (DSS) except for a reduction in amplitude which was due to a scale dependence of \sqrt{r} (see Fig. 5.4). The nature of this scale dependence will be shown explicitly in section 5.4.

This system exhibits a Type II critical solution which is characterized by the following universal scaling behavior for the black hole mass near criticality:

$$M_{bh} \propto |p - p^*|^\lambda. \tag{5.43}$$

The critical parameter, p^* , is the value of p at the threshold of black hole formation. As the tuning parameter, p , is tuned arbitrarily close to p^* , a black hole of arbitrarily small mass is formed. This can be seen from the data in Fig. 5.1. The scaling exponent, λ , is universal in that it is independent of the family of initial data. The system has a $\lambda = 0.257$ for the gaussian family and $\lambda = 0.258$ for the kink data. There is uncertainty in the third significant figure.

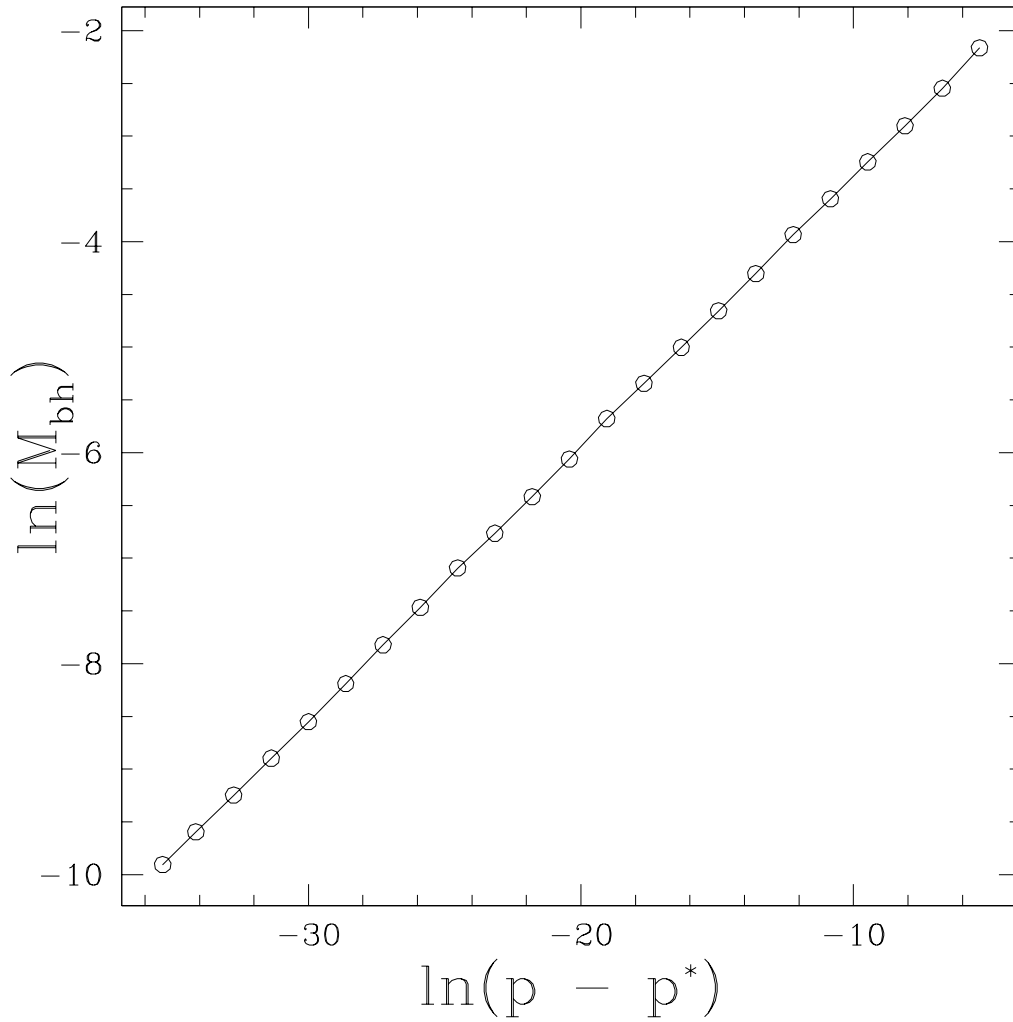


Figure 5.1: Plot of the \ln of black hole mass vs. the \ln of $(p - p^*)$. The scaling exponent is $\lambda = 0.257$ (the third significant figure is uncertain) for the gaussian family. As one tunes arbitrarily close to the critical parameter, p^* , a black hole of arbitrarily small mass is formed indicative of a Type II critical solution. Note the absence of oscillations about the fit line which would be present if $a(t, r)$ were discretely self-similar.

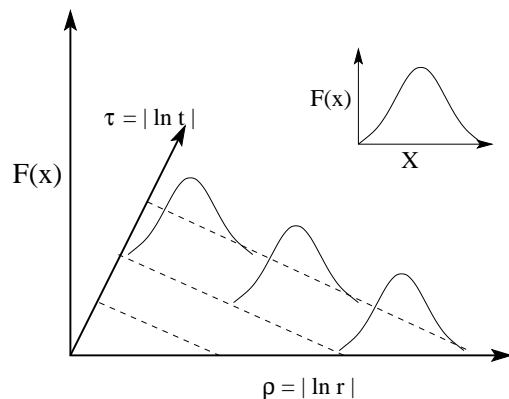


Figure 5.2: Scale invariant quantities (functions of $x = -r/t$) reproducing themselves at smaller and smaller temporal and spatial scales (logarithmically) in accordance with continuous self-similarity.

5.4 Self-Similar Ansatz

As we have seen from the solution of our PDEs, near criticality scale invariant quantities reproduce themselves at smaller and smaller scales in accordance with self-similarity (an illustration of this is given in Fig. 5.2).

Since these solutions have been shown to exist, it should be possible to apply a self-similar ansatz to our system *ab initio*, as was done for the collapse of a complex scalar field by Hirschmann and Eardley [17]. A self-

similar spacetime has a homothetic Killing vector, ξ , which obeys:

$$\mathcal{L}_\xi g_{\mu\nu} = 2g_{\mu\nu}. \quad (5.44)$$

Here the factor 2 is simply a matter of convention. We want to define coordinates, (τ, x) that are adapted to this self-similar symmetry. Defining τ to be adapted to the vector field ξ^μ means that in these coordinates, (5.44) can be written as:

$$\frac{\partial}{\partial \tau} g_{\mu\nu}(\tau, x) = 2g_{\mu\nu}(\tau, x). \quad (5.45)$$

Performing a separation of variables on the metric tensor and then solving (5.45) for the τ -dependent part yields:

$$g_{\mu\nu}(\tau, x) = e^{2\tau} \tilde{g}_{\mu\nu}(x) \quad (5.46)$$

where $\tilde{g}_{\mu\nu}(x)$ is the part of the metric that depends only on x . The equations defining the coordinate transformation from the original (t, r) to the adapted (τ, x) can be found by first solving (5.44) for the vector components ξ^μ in the original coordinates then seeing what relationship is consistent with the vector transformation law. The result is:

$$\tau = \ln \left| \frac{t^* - t}{L} \right|, \quad x = \frac{r}{t^* - t}. \quad (5.47)$$

The equations will take the same form for any value of the constant factor, L , which we set to 1. The time, t^* , is called the accumulation point. This is the time when the self-similar solution reaches the origin. It is convenient to take t to be the central proper time and rescale it so that $t^* = 0$. Writing our metric (5.1) in these coordinates, gives:

$$ds^2 = e^{2\tau} [(-\alpha(x)^2 + x^2 a(x)^2) d\tau^2 + 2xa(x)^2 d\tau dx + a(x)^2 dx^2 + x^2 d\theta^2 + x^2 \sin^2 \theta d\phi^2]. \quad (5.48)$$

The τ coordinate is timelike. The functions, α and a are functions of the spacelike coordinate x alone. This can be verified by comparing the right hand sides of (5.46) and (5.48).

In these coordinates, we take as our spinors (5.27),(5.28) the following:

$$\psi^+ = \frac{e^{-\tau}}{2\sqrt{\pi}} \frac{e^{i\phi/2}}{x\sqrt{a(x)}} \begin{pmatrix} F(\tau, x) \sin(\theta/2) \\ G(\tau, x) \cos(\theta/2) \\ F(\tau, x) \sin(\theta/2) \\ G(\tau, x) \cos(\theta/2) \end{pmatrix} \quad (5.49)$$

$$\psi^- = \frac{e^{-\tau}}{2\sqrt{\pi}} \frac{e^{-i\phi/2}}{x\sqrt{a(x)}} \begin{pmatrix} F(\tau, x) \cos(\theta/2) \\ -G(\tau, x) \sin(\theta/2) \\ F(\tau, x) \cos(\theta/2) \\ -G(\tau, x) \sin(\theta/2) \end{pmatrix}. \quad (5.50)$$

These were found by transforming the (t, r) parts of (5.27) and (5.28) as scalars.

In order to find spinor components that are only functions of x , we require knowledge of the τ dependence of our field quantities. This is found by performing the coordinate transformations on the equations of motion (5.29)-(5.32) and the geometric equations (5.37) and (5.39), and then ascertaining what τ dependence F and G have to produce a set of τ independent ODEs. We have for the exponential τ dependence:

$$\begin{aligned} F(\tau, x) &= e^{\tau/2} e^{i\omega\tau} x(P_1(x) + iP_2(x)) \\ G(\tau, x) &= e^{\tau/2} e^{i\omega\tau} x(Q_1(x) + iQ_2(x)). \end{aligned} \quad (5.51)$$

It is possible to have standing waves in the field variables that will produce a static spacetime so, we account for this freedom by introducing the periodic τ dependence above. The extra factor of x is introduced to cast our equations in a more convenient form. With these definitions we find:

$$P_1' = \frac{1}{x + \alpha/a} \left[-\frac{1}{2}P_1 - \omega P_2 - \frac{1}{2} \frac{\alpha}{a} \left(\frac{a^2 + 1}{x} \right) P_1 + 2\alpha P_1(P_1 Q_1 + P_2 Q_2) + \frac{\alpha}{x} Q_2 \right] \quad (5.52)$$

$$P_2' = \frac{1}{x + \alpha/a} \left[-\frac{1}{2}P_2 + \omega P_1 - \frac{1}{2} \frac{\alpha}{a} \left(\frac{a^2 + 1}{x} \right) P_2 + 2\alpha P_2(P_1 Q_1 + P_2 Q_2) - \frac{\alpha}{x} Q_1 \right] \quad (5.53)$$

$$Q_1' = \frac{1}{x - \alpha/a} \left[-\frac{1}{2}Q_1 - \omega Q_2 + \frac{1}{2} \frac{\alpha}{a} \left(\frac{a^2 + 1}{x} \right) Q_1 - 2\alpha Q_1(P_1 Q_1 + P_2 Q_2) + \frac{\alpha}{x} P_2 \right] \quad (5.54)$$

$$Q_2' = \frac{1}{x - \alpha/a} \left[-\frac{1}{2}Q_2 + \omega Q_1 + \frac{1}{2} \frac{\alpha}{a} \left(\frac{a^2 + 1}{x} \right) Q_2 - 2\alpha Q_2(P_1 Q_1 + P_2 Q_2) - \frac{\alpha}{x} P_1 \right] \quad (5.55)$$

$$\frac{a'}{a} = \frac{1 - a^2}{2x} + 2x (P_1 P_2' - P_1' P_2 + Q_1' Q_2 - Q_1 Q_2') + 4a (P_1 Q_1 + P_2 Q_2) \quad (5.56)$$

$$\frac{\alpha'}{\alpha} = \frac{a^2 - 1}{2x} + 2x (P_1 P_2' - P_1' P_2 + Q_1' Q_2 - Q_1 Q_2'). \quad (5.57)$$

Before integration of this system, the Dirac equation (5.52)-(5.55) is used to replace the derivatives of P and Q on the right hand side of the equations for a (5.56) and α (5.57).

5.5 Shooting Method and Results

Now that we have rewritten our equations in a coordinate system adapted to the symmetry of self-similarity, we are ready to solve our ODEs. Following Hirschmann and Eardley in [17], we use a shooting method to integrate the equations.

Notice that our system has singularities at $x = 0$ and at $x = x_2 = \alpha/a$ (the similarity horizon). Of the many solutions to our ODEs, the one which is analytic at both of these points is the one which corresponds to the self-similar solution found in the PDEs. We do not know the values of all of the fields at the origin and we do not know the value of x_2 (the position of the similarity horizon). We therefore adopt a shooting method. We shoot outwards from $x = 0$ and inwards from $x_2 = \alpha/a$, then compare the solutions

at some intermediate point x_1 . This process is automated by using Newton's method to determine the shooting parameters for the subsequent iterations. The function we use to determine the goodness of fit is the square of the differences of the values of the functions and their derivatives at this midpoint.

At $x = 0$ we have the following conditions:

$$P_1(0) = 0$$

$$P_2(0) = -Q_0$$

$$Q_1(0) = Q_0$$

$$Q_2(0) = 0$$

$$\alpha(0) = 1$$

$$a(0) = 1.$$

Regularity at the origin gives $P_1 = Q_2$ and $P_2 = -Q_1$. We use the global $U(1)$ invariance of our system (5.52)-(5.57) to set $P_1 = 0$. This leaves Q_0 as a shooting parameter.

As noted previously, the location of the similarity horizon (outer boundary of the integration domain) x_2 is itself a shooting parameter. The outer boundary is itself a shooting parameter and is defined to be $x = x_2$ where $x_2 = \alpha/a$. In the limit $x \rightarrow x_2$ we have the following:

$$P_1(x_2) = \frac{1}{2a^2} (-4\alpha Q_2^3 \omega - 4\alpha Q_1^2 Q_2 \omega + 2a\omega Q_1 + Q_2 a^3)$$

$$P_2(x_2) = \frac{1}{2a^2} (4\alpha Q_1 Q_2^2 \omega + 4\alpha Q_1^3 \omega + 2a\omega Q_2 - Q_1 a^3)$$

$$Q_1(x_2) = Q_1$$

$$Q_2(x_2) = Q_2$$

$$\alpha(x_2) = x_2 a$$

$$a(x_2) = a.$$

The shooting parameters at the outer boundary are: x_2 , $Q_1(x_2)$, $Q_2(x_2)$, and $a(x_2)$. The final shooting parameter is the frequency, ω , which gives us a total of six.

The final results are:

$$x_2 = 5.6740230 \pm 0.0000004$$

$$\omega = 4.698839 \pm 0.000001$$

$$Q_1(0) = 0.747912623 \pm 0.000000006$$

$$Q_1(x_2) = 0.00151341532 \pm 0.00000000007$$

$$Q_2(x_2) = 0.01103266083 \pm 0.00000000005$$

$$a(x_2) = 1.1183631604 \pm 0.00000000009$$

where the quoted uncertainty was estimated by solving the system for different values of x_1 many times and noting the changes in the above quantities.

5.6 Comparisons of Solutions

We compare the solutions of the ODEs to the solutions of the PDEs in the (t, r) coordinate system. For the case of $a(t, r)$, we use the ODE solution as a fitting function for the PDE data, where t^* is the fitting parameter. This is done by making a 2-dimensional solution surface in t and r and using Newton's method to adjust the fitting parameter. The goodness of fit is defined to be the least squares of the two solutions. Once t^* is found, the l_2 -norm of the difference of the two solutions is 0.00159. We express the solutions as an evolution in Fig. 5.3.

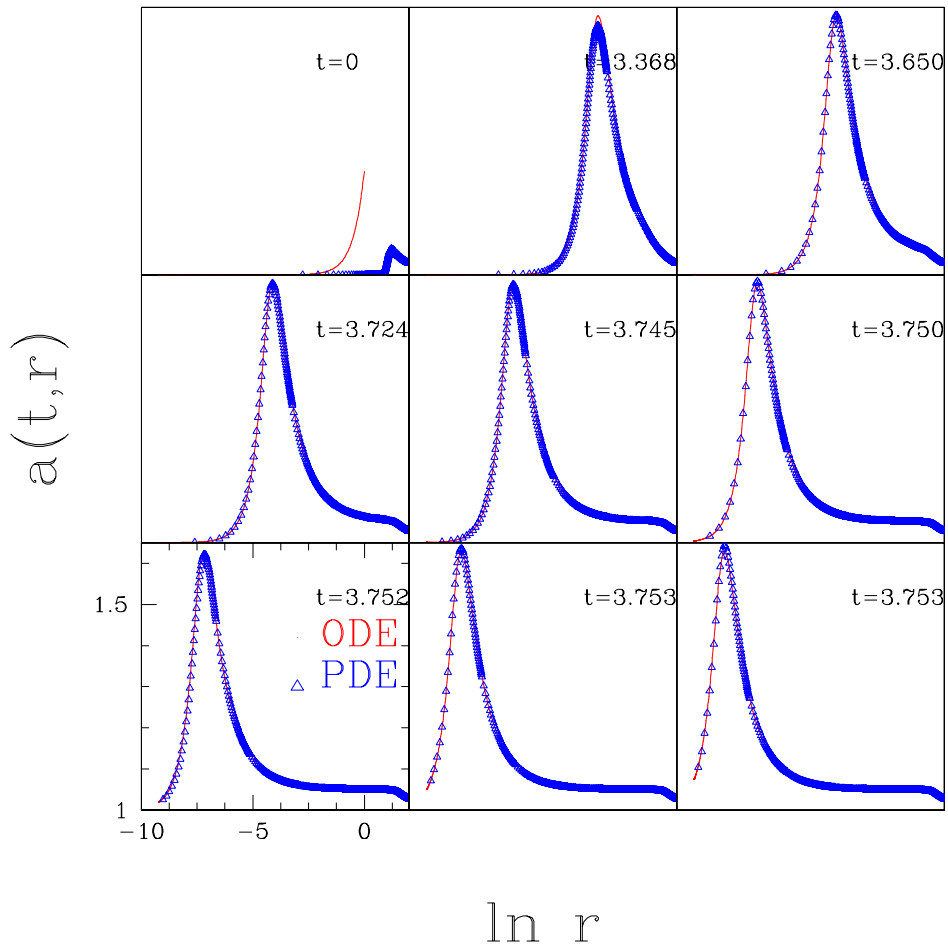


Figure 5.3: The metric variable, $a(t,r)$, for a slightly supercritical evolution overlaid with the solution to the ODEs vs. $\ln(r)$. The frames are output logarithmically in central proper time. The function's peak reaches a value of approximately 1.6 and remains there as the solution continuously repeats itself on smaller and smaller scales.

Comparing the Dirac fields is a little more involved since there are a number of unspecified parameters and phases that must be determined. The Dirac fields are:

$$\begin{aligned}
F_1(t, r) &= \frac{rA_1}{(t^* - t)^{\frac{1}{2}}} [P_1(t, r) \cos(\omega \ln(t^* - t) + \phi_1) - P_2(t, r) \sin(\omega \ln(t^* - t) + \phi_1)] \\
F_2(t, r) &= \frac{rA_2}{(t^* - t)^{\frac{1}{2}}} [P_1(t, r) \sin(\omega \ln(t^* - t) + \phi_2) + P_2(t, r) \cos(\omega \ln(t^* - t) + \phi_2)] \\
G_1(t, r) &= \frac{rA_2}{(t^* - t)^{\frac{1}{2}}} [Q_1(t, r) \cos(\omega \ln(t^* - t) + \phi_2) - Q_2(t, r) \sin(\omega \ln(t^* - t) + \phi_2)] \\
G_2(t, r) &= \frac{rA_1}{(t^* - t)^{\frac{1}{2}}} [Q_1(t, r) \sin(\omega \ln(t^* - t) + \phi_1) + Q_2(t, r) \cos(\omega \ln(t^* - t) + \phi_1)].
\end{aligned} \tag{5.58}$$

Notice that F_1 and G_2 have the same phase, ϕ_1 . The pair F_2 and G_1 have the same phase ϕ_2 . This is expected from the coupling of (5.29)-(5.32). The equations of motion may be invariant under changes of these phases, but (5.37) and (5.39) are not. In order to have the entire system be invariant under changes in the phases, we must have:

$$A_1 A_2 = \frac{1}{\cos(\phi_1 - \phi_2)}$$

We see that the amplitudes of the fields must change only if the *relative* phase, $\phi_1 - \phi_2$, changes. The comparison of the fields as found from the PDEs and ODEs is carried out in much the same way as it is done for the metric variable, $a(t, r)$. The goodness of fit is again defined to be the least squares of the two solutions but this time, the parameter t^* is kept fixed and the phase ϕ_j and amplitude A_j are used as fitting parameters ($j = 1, 2$). The l_2 -norm of the difference of the solutions for F_1 is 0.000195 with $A_1 = 1.0450$ and $\phi_1 = 0.6846$. The l_2 -norm of the difference of the solutions for G_1 is 0.00024 with $A_2 = 1.5780$ and $\phi_2 = 6.0427$. We express the ODE and PDE solutions of F_1 as evolutions in Fig. 5.4.

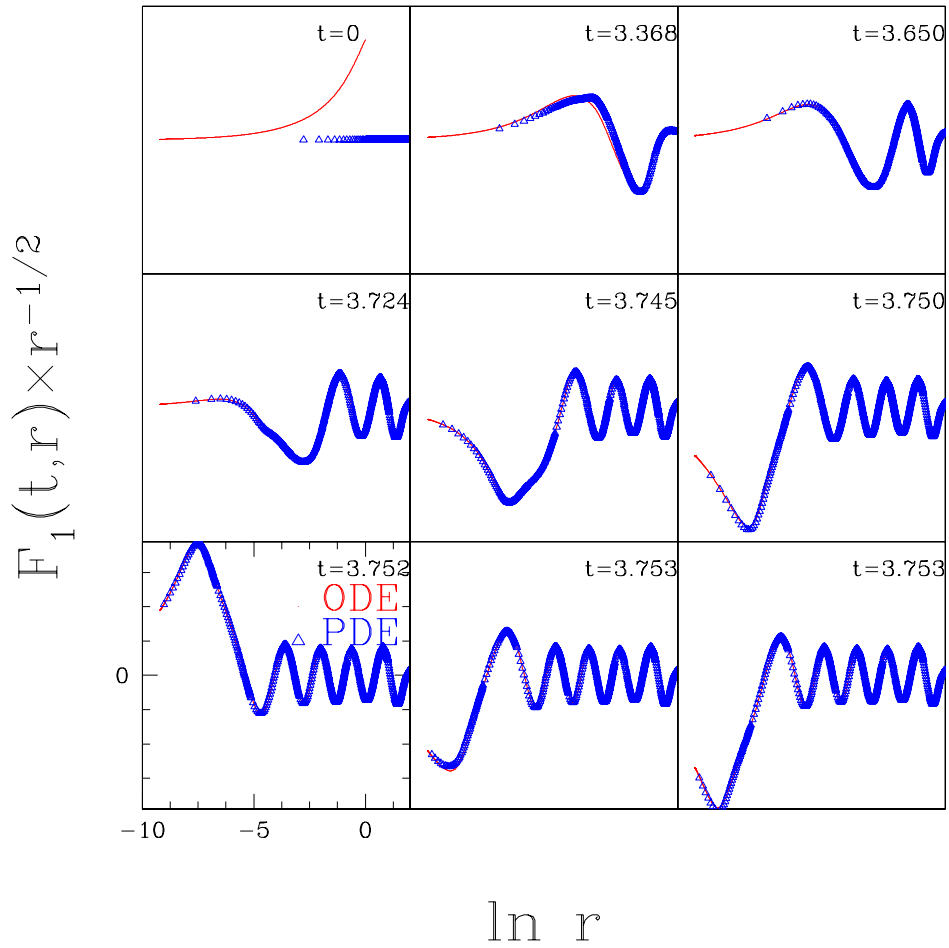


Figure 5.4: The quantity $F_1(t, r)$ for a slightly supercritical evolution and the solution found from the ODEs vs. $\ln(r)$. The frames are output logarithmically in central proper time. The function oscillates and discretely repeats itself on smaller and smaller scales. A factor of $1/\sqrt{r}$ has been introduced to remove the scale dependence.

5.7 Conclusions

We have investigated the spherically symmetric Einstein-massless-Dirac system at the threshold of black hole formation. We find that there is a mass scaling law with a universal exponent indicative of a Type II critical solution. The solution exhibits continuous self-similarity in the geometric variables and discrete self-similarity in the components of the Dirac fields. Using a self-similar ansatz, we reduced our system to a set of ODEs whose solution was in very good agreement with the critical solution obtained from the original PDEs.

Chapter 6

Einstein-Massless-Dirac System for any l

6.1 Introduction

In Chapter 5 we rederived our system for the massless case from first principles using the idea of an incoherent sum of the stress-tensors of the individual spinors (5.19). The spin- $\frac{1}{2}$ fields' individual spin-angular momenta combined to form a spherically symmetric system with no net spin. That system is constructed from spinors with spin-angular momentum quantum number of $l = \frac{1}{2}$. One benefit of this rederivation is that we can now extend this procedure to include other values of l .

In this chapter, we construct the massless, spherically symmetric system so that it has an explicit dependence on l that can be adjusted as a parameter of the model. As l is increased, the number of shells of counter spin is increased. This has the effect of increasing the strength of the “spin-angular momentum barrier”.

6.1.1 Equations of Motion for any l

The new, l -dependent equations of motion take the form

$$\dot{F}_1 = -\sqrt{\frac{\alpha}{a}} \partial_r \left(\sqrt{\frac{\alpha}{a}} F_1 \right) + \frac{\alpha}{r} \left(l + \frac{1}{2} \right) G_2 \quad (6.1)$$

$$\dot{G}_1 = \sqrt{\frac{\alpha}{a}} \partial_r \left(\sqrt{\frac{\alpha}{a}} G_1 \right) + \frac{\alpha}{r} \left(l + \frac{1}{2} \right) F_2 \quad (6.2)$$

$$\dot{F}_2 = -\sqrt{\frac{\alpha}{a}}\partial_r\left(\sqrt{\frac{\alpha}{a}}F_2\right) - \frac{\alpha}{r}\left(l + \frac{1}{2}\right)G_1 \quad (6.3)$$

$$\dot{G}_2 = \sqrt{\frac{\alpha}{a}}\partial_r\left(\sqrt{\frac{\alpha}{a}}G_2\right) - \frac{\alpha}{r}\left(l + \frac{1}{2}\right)F_1. \quad (6.4)$$

These were found by acting the angular raising and lowering operators $\bar{\partial}$ (eth) and $\bar{\partial}$ (ethbar) on the spin weighted spherical harmonics of general l (5.22-5.23).

6.1.2 Geometry for any l

The spherically symmetric stress-energy tensor for general l was found by induction. The same procedure that was used for the $l = \frac{1}{2}$ case in Chapter 5 was used for $l = \frac{3}{2}$ and $\frac{5}{2}$. The resulting stress-energy tensors were compared to determine what the l -dependent terms were. We find that the spherically symmetric stress-energy tensor for general l takes the form:

$$\begin{aligned} T_{tt} &= \frac{\alpha(l + \frac{1}{2})}{2\pi r^2 a} \left(\dot{F}_1 F_2 - F_1 \dot{F}_2 + \dot{G}_1 G_2 - G_1 \dot{G}_2 \right) \\ T_{tr} &= \frac{(l + \frac{1}{2})}{4\pi r^2} \left[F_1 \dot{F}_2 - \dot{F}_1 F_2 + \dot{G}_1 G_2 - G_1 \dot{G}_2 + \frac{\alpha}{a} (F_1' F_2 - F_1 F_2' + G_1' G_2 - G_1 G_2') \right] \\ T_{rr} &= \frac{(l + \frac{1}{2})}{2\pi r^2} (F_1 F_2' - F_1' F_2 + G_1' G_2 - G_1 G_2') \\ T_{\theta\theta} &= \frac{(l + \frac{1}{2})^2}{2\pi r a} (F_1 G_1 + F_2 G_2) \\ T_{\phi\phi} &= \sin^2 \theta \frac{(l + \frac{1}{2})^2}{2\pi r a} (F_1 G_1 + F_2 G_2). \end{aligned} \quad (6.5)$$

However the l dependent prefactors which appear explicitly above can be disregarded for this problem (i.e. the same expressions for the stress-energy tensor which were used in Chapter 5 — without l could be used here). This is because the only components of the stress-energy tensor used in this spherically

symmetric system are T_{tt} , T_{tr} , and T_{rr} which all have the same prefactors. The components of the spinors can always be rescaled so that these factors become unity. There is, however, an *implicit* dependence on l which can't be scaled away. It is the dependence which comes from the equations of motion (6.1)-(6.4) when they are substituted into the expression for T_{tt} to replace the time derivatives of the F 's and G 's. Thus the only geometric equation which changes is the *Hamiltonian constraint*:

$$\frac{a'}{a} + \frac{a^2 - 1}{2r} = \frac{2}{r^2} \left[2 \left(l + \frac{1}{2} \right) a F_1 G_1 + 2 \left(l + \frac{1}{2} \right) a F_2 G_2 \right. \quad (6.6)$$

$$\left. + r F_1 F_2' - r F_1' F_2 + r G_1' G_2 - r G_1 G_2' \right]. \quad (6.7)$$

The other equations for our geometric variables remain unchanged, but we restate them here for completeness. They are the *momentum constraint*:

$$\dot{a} = \frac{2\alpha}{r} (F_1' F_2 - F_1 F_2' + G_1' G_2 - G_1 G_2'). \quad (6.8)$$

and the slicing equation for α , the lapse

$$\frac{\alpha'}{\alpha} - \frac{a^2 - 1}{2r} = \frac{2}{r} (F_1 F_2' - F_1' F_2 + G_1' G_2 - G_1 G_2'). \quad (6.9)$$

6.2 Numerics and Results

We again solve the above equations of motion using an iterative Crank-Nicholson update scheme, standard $O(h^2)$ spatial derivatives, and Kreiss-Oliger style dissipation [19]. This time, however, adaptive mesh refinement was not always required. In particular, we only used AMR for $l = \frac{3}{2}$, $l = \frac{5}{2}$, $l = \frac{7}{2}$, and $l = \frac{9}{2}$. The reason for this will be explained shortly. At $r = 0$, the

following regularity conditions were enforced:

$$\begin{aligned}
 F_1(t, 0) &= 0 \\
 F_2(t, 0) &= 0 \\
 G_1(t, 0) &= 0 \\
 G_2(t, 0) &= 0.
 \end{aligned}
 \tag{6.10}$$

We again set $a(t, 0) = 1$ and choose $\alpha(t, \infty) = 1$.

Investigation of the threshold of black hole formation is carried out as was done previously. The end state of the evolution is controlled by a single tuning parameter, p , (we used the amplitude of the initial gaussian pulse). Either the value of p would be super-critical and $2M/r$ would become arbitrarily close to 1 (we usually used 0.99) at some value of r signalling the formation of a black hole, or the tuning parameter would be sub-critical and $2M/r$ would reach some maximum value before decreasing as the field dissipated to spatial infinity. In this way we tuned p to some critical value representing the threshold of black hole formation. We found Type II, CSS solutions for $l = \frac{3}{2}$ and $l = \frac{5}{2}$ which required the use of AMR as the solutions continuously repeated themselves on smaller and smaller spatial and temporal scales. As Type II solutions, they have a mass scaling law (5.43) which can be seen in Fig. 6.1 along side the black hole mass scaling plot for $l = \frac{1}{2}$. The y -intercepts of the plots were adjusted so the data could be displayed more easily.

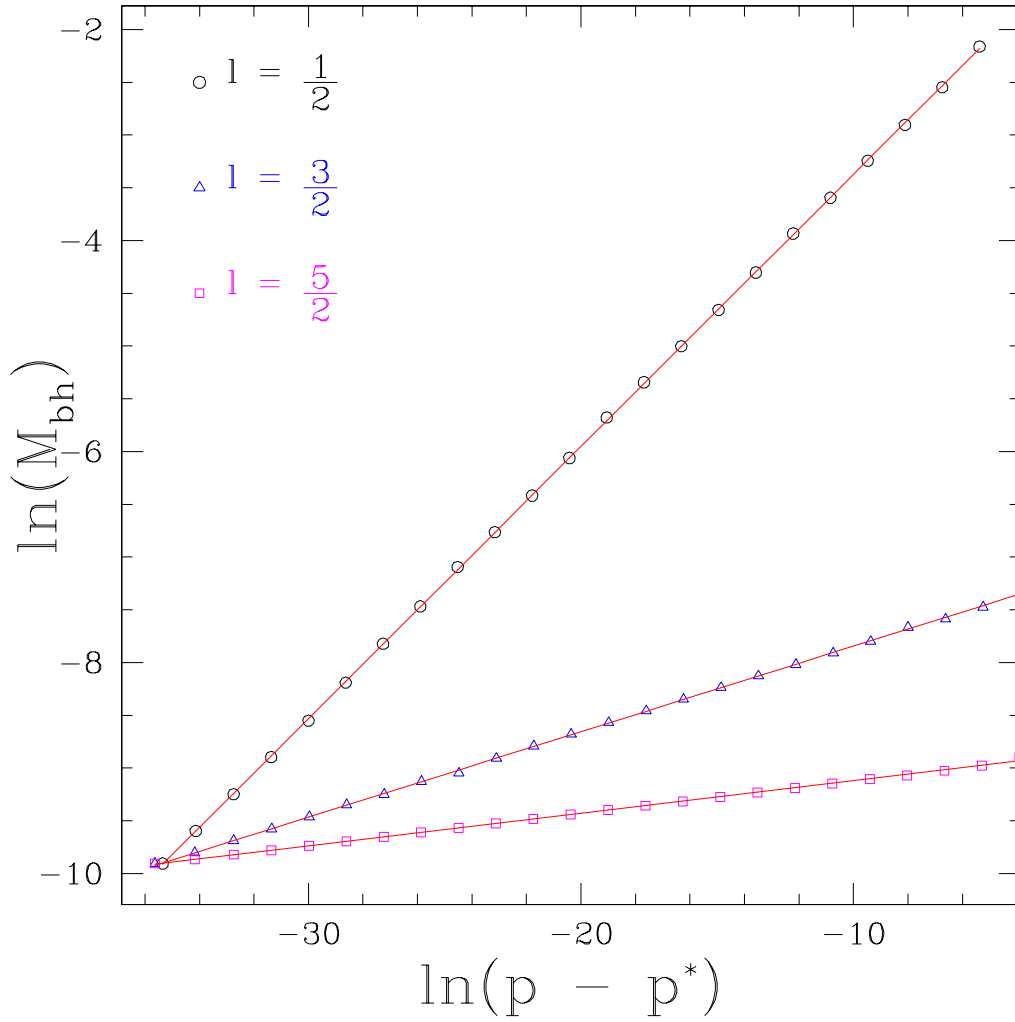


Figure 6.1: Plot of the \ln of black hole mass vs. the \ln of $(p - p^*)$ for $l = 1/2$, $l = 3/2$, and $l = 5/2$. The scaling exponents are $\lambda = 0.257$, 0.081 , and 0.03 , respectively. As one tunes arbitrarily close to the critical parameter, p^* , a black hole of arbitrarily small mass is formed indicative of a Type II critical solution. All of these solutions display continuous self-similarity. The y -intercepts have been adjusted so that all three lines can be plotted together.

Although the spinor harmonics that are used for the angular parts of the spinors are only defined for half-odd integer values of l , there is no reason why the field equations can't be solved for arbitrary values (i.e. integer values). We find Type II behavior for $l = 1$ and 2 . As we increase l we have difficulty finding Type II behavior until we reach $l = \frac{11}{2}$. The reason for this is not clear and will require further study. These values of l between $\frac{5}{2}$ and $\frac{11}{2}$ do not display self-similarity nor do they spend a long time in a slightly oscillating configuration as does $l = \frac{11}{2}$ and $\frac{13}{2}$ (discussed below). The natural log of the scaling exponents, λ , for the cases that *do* display Type II behavior can be plotted against the spin-angular momentum quantum number, l , as seen in Fig. 6.2. These results are very preliminary and the fit line used in the plot is not meant to suggest a linear relationship. A linear fit of the data yields a slope of -0.9 (the uncertainty represents uncertainty in the linear fit). However, the results at this stage are too preliminary to draw any conclusions. The value of the scaling exponent does decrease as l is increased, but the precise functional relationship has yet to be determined. Most importantly if this trend exists then there should be Type II solutions for $l = \frac{7}{2}$, and $\frac{9}{2}$. This has not yet been seen.

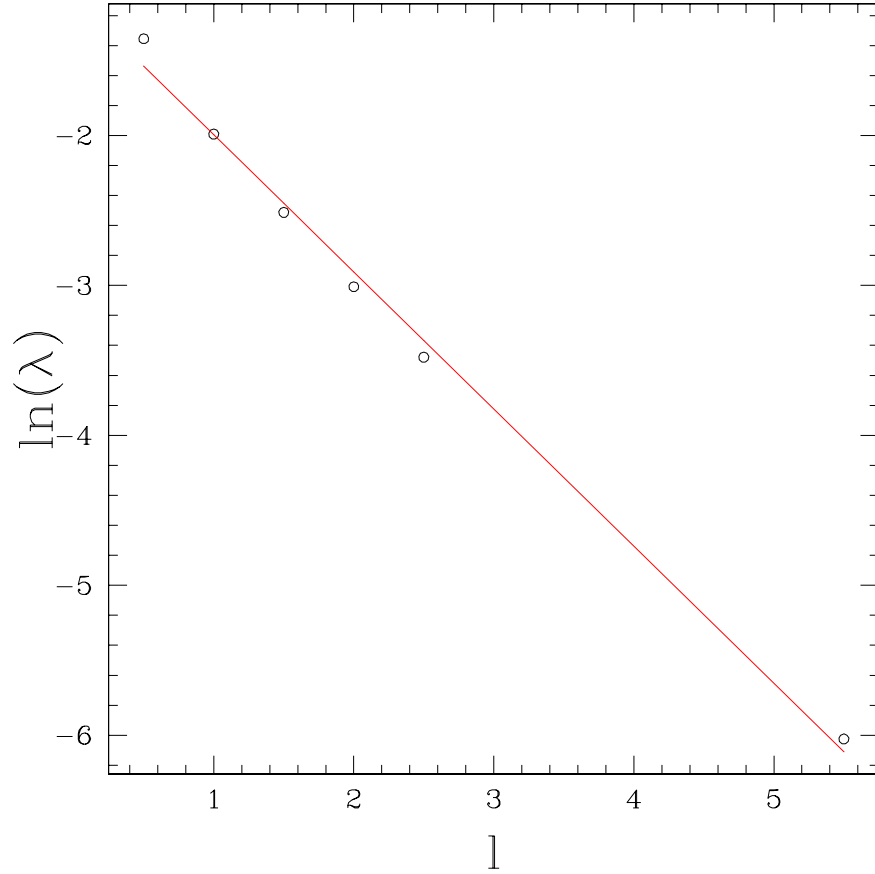


Figure 6.2: Plot of the \ln of black hole mass scaling exponent, λ , vs. the spin-angular momentum quantum number l . We have used the half-odd integer values $l = 1/2, 3/2, 5/2$, and $11/2$. In addition to these, we have also used the *integer* values $l = 1$ and 2 . Although the spinor harmonics which are used for the angular parts of the spinors are only defined for half-odd integer values of l , there is no reason why the field equations cannot be solved for arbitrary values. A linear fit of the data yields a slope of -0.9 ± 0.008 (the uncertainty represents uncertainty in the linear fit). However, the results at this stage are too preliminary to draw any conclusions. The value of the scaling exponent does decrease as l is increased, but the precise functional relationship has yet to be determined.

As l is increased to $\frac{7}{2}$, the spin-angular momentum barrier appears to have sufficient strength to prevent the fields from progressing very far towards the origin. Self-similarity was not evident as the pulse imploded to a value of r where it remained for a short time before either forming a black hole or dispersing. The slightly super-critical evolution of $2M/r$ for $l = \frac{7}{2}, \frac{9}{2}$, and $\frac{11}{2}$ can be seen in Fig. 6.3. The time of delay for $l = \frac{7}{2}, \frac{9}{2}$ is slight but the delay time for $\frac{11}{2}$ is much more pronounced. As l is increased to $\frac{13}{2}$, the threshold solution has a value of $2M/r$ which persists at approximately 0.79 for $t = 33$ to $t = 220$ before ultimately collapsing towards black hole formation (see Fig. 6.4). For $l = \frac{11}{2}$ and $\frac{13}{2}$ we see a logarithmic scaling of the time to form a black hole as p is tuned closer to criticality as seen in Fig. 6.5.

Table 6.1: Results for various values of l .

<i>Value of l</i>	<i>Method of solution</i>	<i>Behavior</i>	λ
1/2	AMR	CSS/Type II	0.257
1	AMR	CSS/Type II	0.136
3/2	AMR	CSS/Type II	0.081
2	AMR	CSS/Type II	0.049
5/2	AMR	CSS/Type II	0.03
7/2	AMR	?	?
9/2	AMR	?	?
11/2	Unigrid	Type II	0.002
13/2	Unigrid	?	?

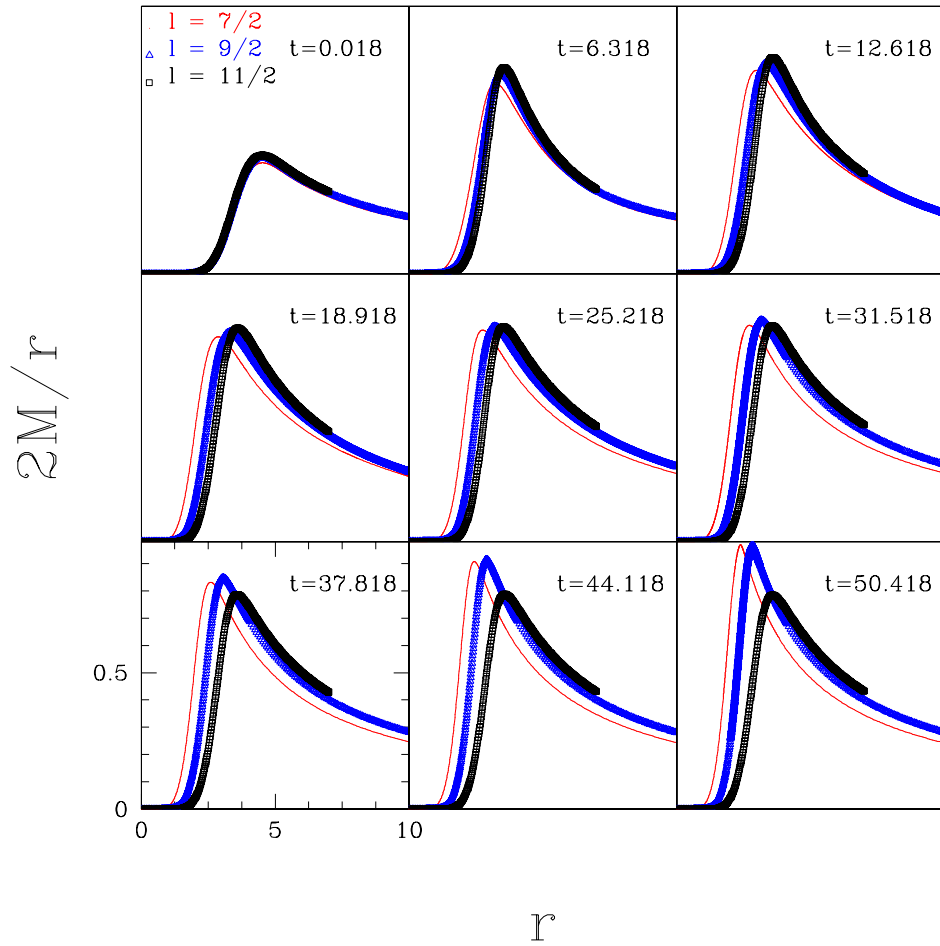


Figure 6.3: A comparison of $2M/r$ for three slightly supercritical evolutions. From left to right the solutions correspond to $l = 7/2$, $9/2$, and $11/2$. In each case, the solution begins an inward implosion which is delayed for a time by the spin-angular momentum barrier. Systems with higher l have a stronger barrier which increases the time of delay before collapse.

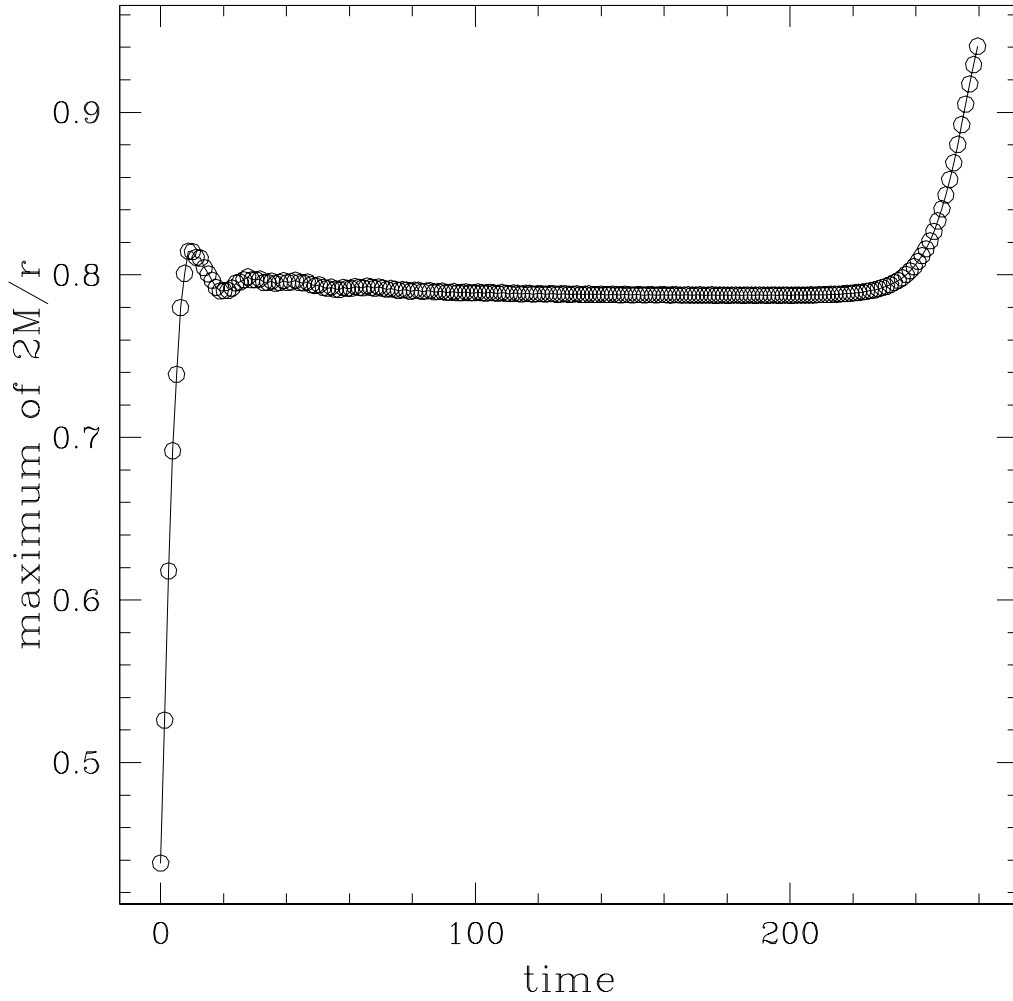


Figure 6.4: Plot of $2M/r$ for a slightly super-critical evolution with $l = 13/2$. The value of $2M/r$ persists at approximately 0.79 from $t = 33$ to $t = 220$ before ultimately collapsing towards black hole formation. The amplitude is not constant but oscillates about 0.79 at the order of 10^{-3} .

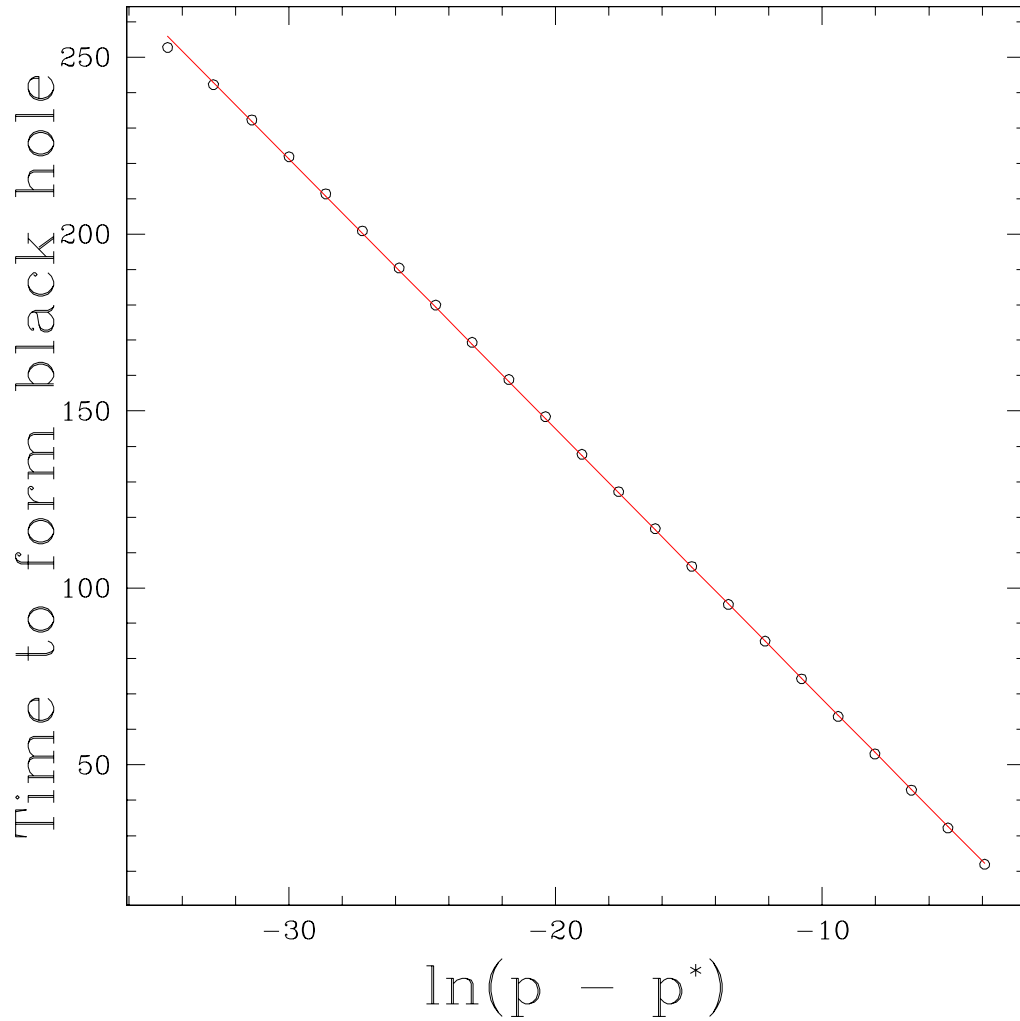


Figure 6.5: Plot of the time to form a black hole vs. the \ln of $(p - p^*)$ for $l = 13/2$. The slope is -7.63 . As one tunes arbitrarily close to the critical parameter, p^* , it takes longer and longer to form a black hole.

6.3 Conclusions

As the spin-angular momentum quantum number, l , increases, so does the strength of the “spin-angular momentum barrier”. We find that as this happens, the scaling exponents for the cases which display Type II behavior decrease. Preliminary evidence implies that there may be a linear relationship between the natural log of the scaling exponent and l . However further study will be necessary to determine if this is indeed the case. In particular, Type II behavior would have to be seen for $l = \frac{7}{2}$ and $\frac{9}{2}$ and the scaling exponents for these cases would have to support the linear relationship mentioned above. It is possible that finding Type II behavior for very high values of l will not be possible since the value of the scaling exponent may be too small to be measured accurately but no such impediment should exist to prevent finding it for $l = \frac{7}{2}$ and $\frac{9}{2}$. In those cases the difficulty may be in the numerics.

Chapter 7

Harmonic Coordinates and the Axisymmetric Einstein Equations

In this chapter we will discuss work on a 2 dimensional, axisymmetric code to solve Einstein's equations. Instead of using the ADM 3+1 formulation, harmonic coordinates are employed. The resulting system of nonlinear PDEs is solved numerically using Chebyshev pseudospectral collocation. Currently the code which solves the evolution equations for the components of the spatial metric is unstable. The elliptic solver is working, however, and is used for finding initial data.

7.1 Harmonic Coordinates

Harmonic coordinates have often been employed by mathematical relativists but have not been widely used in numerical relativity. Some recent work has been done by Garfinkle [13] in this area. Harmonic coordinates are coordinates that obey the wave equation (this is sometimes called de Donder gauge). This general wave equation is

$$g^{\lambda\sigma}\nabla_\lambda\nabla_\sigma x^\mu = 0. \tag{7.1}$$

The index, μ , is not a tensor index, but is merely a label for the different coordinates. A source can be added to the right hand side of the equation to

yield

$$g^{\lambda\sigma}\nabla_\lambda\nabla_\sigma x^\mu = H^\mu. \quad (7.2)$$

Evaluating (7.2) gives a condition for the metric components:

$$g^{\lambda\sigma}\Gamma^\mu_{\lambda\sigma} = -H^\mu. \quad (7.3)$$

The reason for using such a coordinate system may not yet seem clear. Since our ultimate goal is to solve Einstein's equations, let us apply the harmonic coordinate condition (7.3) to the Ricci tensor. The result is:

$$\begin{aligned} R_{\mu\nu} = & -\frac{1}{2}g^{\lambda\sigma}\partial_\lambda\partial_\sigma g_{\mu\nu} - \Gamma^\lambda_{\alpha\mu}\Gamma^\alpha_{\lambda\nu} + \Gamma^\lambda_{\mu\nu}H_\lambda - \partial_{(\mu}H_{\nu)} \\ & + \frac{1}{2}g^{\alpha\lambda}g^{\beta\sigma}(\partial_\mu g_{\alpha\beta})(\partial_\lambda g_{\nu\sigma}) + \frac{1}{2}g^{\alpha\lambda}g^{\beta\sigma}(\partial_\nu g_{\alpha\beta})(\partial_\lambda g_{\mu\sigma}) \end{aligned} \quad (7.4)$$

This yields the so called *reduced* Einstein's equations which look more like a set of wave equations than the general Einstein's equations (particularly the first term on the right hand side of (7.4)). We note that Einstein's equations

$$G_{\mu\nu} = R_{\mu\nu} - \frac{1}{2}Rg_{\mu\nu} = 8\pi T_{\mu\nu} \quad (7.5)$$

can be rewritten in terms of the Ricci tensor as

$$R_{\mu\nu} = 8\pi \left(T_{\mu\nu} - \frac{1}{2}Tg_{\mu\nu} \right) \quad (7.6)$$

where

$$T = g^{\mu\nu}T_{\mu\nu} \quad (7.7)$$

and this is the form we will use below.

7.2 Solving the System

We will restrict ourselves to axisymmetry and will work in cylindrical coordinates (t, ρ, z, ϕ) . The flat spacetime metric in these coordinates is:

$$g_{\mu\nu} = \begin{pmatrix} -1 & 0 & 0 & 0 \\ 0 & 1 & 0 & 0 \\ 0 & 0 & 1 & 0 \\ 0 & 0 & 0 & \rho^2 \end{pmatrix} \quad (7.8)$$

We put Einstein's equations into first order form (in time) by defining:

$$P_{\mu\nu} \equiv \partial_t g_{\mu\nu}. \quad (7.9)$$

Unlike the previous systems studied in this thesis which used constrained evolution, the approach we take here is a free evolution. This means that we solve our constraints only at the initial time to determine our initial data. This data is then evolved in time using the evolution equations given by (7.4).

We find initial data by first choosing $g_{ij} = h_{ij}$, $g_{i0} = g_{0i} = 0$, $g_{00} = -1$, and $P_{ij} = -2K_{ij}$ at the initial time. The $P_{0\nu}$ components are found from (7.3). The spatial part of the metric at the initial time will be:

$$h_{ij} = \begin{pmatrix} g_{\rho\rho} & 0 & 0 \\ 0 & 1 & 0 \\ 0 & 0 & \rho^2 \end{pmatrix} \quad (7.10)$$

We also take the spatial components $P_{ij} = 0$.

The Hamiltonian constraint for this initial data is:

$$\mathcal{R} = 16\pi\rho_m \quad (7.11)$$

where ρ_m is the local energy density for the matter. Evaluating the Ricci scalar for the initial, spacelike hypersurface gives the final form of the Hamiltonian constraint:

$$\frac{\partial_\rho g_{\rho\rho}}{\rho} - (\partial_z^2 g_{\rho\rho})g_{\rho\rho} + \frac{1}{2}(\partial_z g_{\rho\rho})^2 = 16\pi\rho_m g_{\rho\rho}^2. \quad (7.12)$$

As a matter model we have used a massive scalar field whose stress-energy tensor is given by:

$$T_{\mu\nu} = \nabla_\mu\Phi\nabla_\nu\Phi - \frac{1}{2}g_{\mu\nu}(g^{\alpha\beta}\nabla_\alpha\Phi\nabla_\beta\Phi - m^2\Phi). \quad (7.13)$$

We solve (7.12) for $g_{\rho\rho}$ using the Newton-Kantorovich linearization procedure and pseudospectral relaxation described in [5]. An initial guess is specified for $g_{\rho\rho}$ then the linearized equation is solved for the update to the guess. This iteration procedure is continued, and converges to the solution efficiently. A plot of the natural log of the l_2 -norm of the difference of the pre-iterate and post-iterate values versus the iteration number is shown in Fig. 7.1. We find the solution efficiently but this can certainly be improved. Perhaps the best way to improve the efficiency is to use domain decomposition to split the domain of our problem into several smaller subdomains [5].

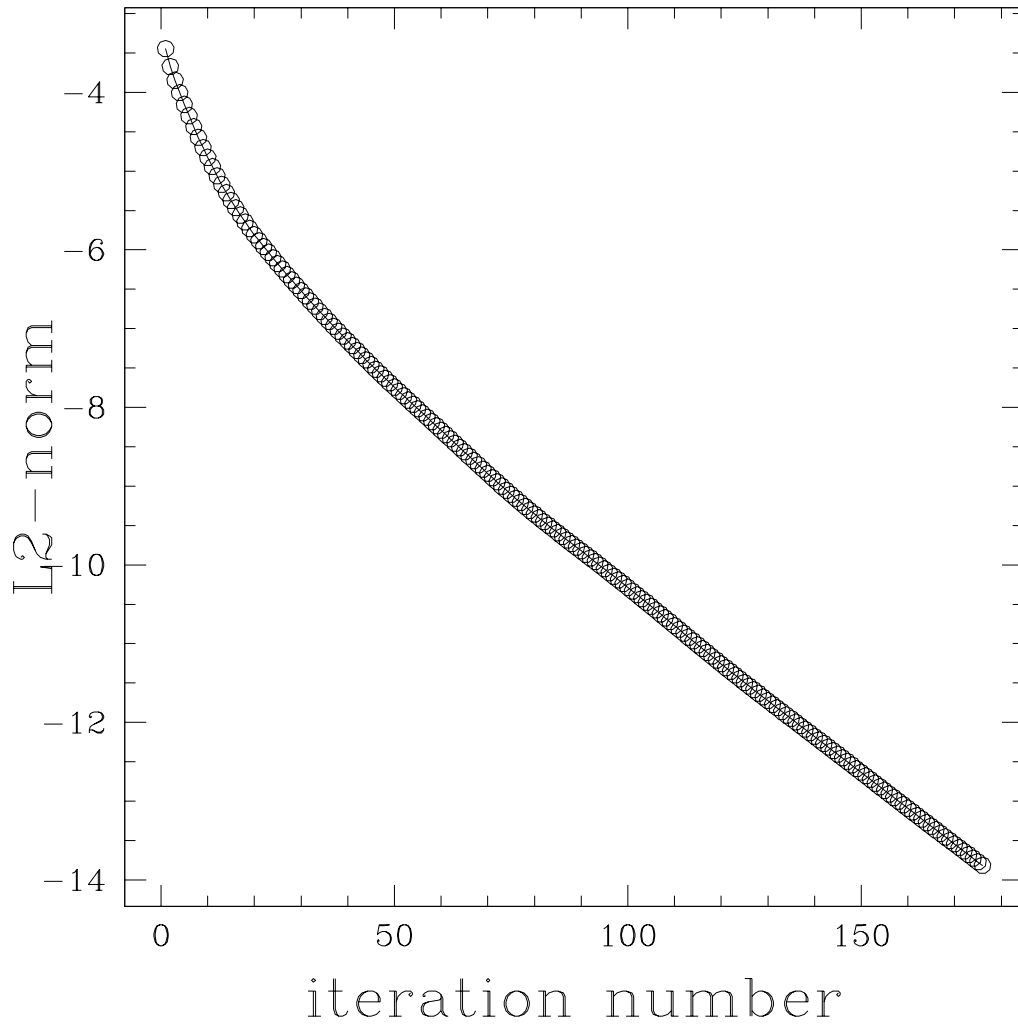


Figure 7.1: A plot of the natural log of the l_2 -norm of the difference of the pre-iterate and post-iterate values vs. the iteration number for the pseudospectral constraint solver.

At the current time, only the constraint can be solved. We have an “operational” evolution code to solve Einstein’s equations for this system, but it is currently unstable. This is almost certainly a result of our choice of H^μ . We are trying to resolve this problem and hope to have results shortly.

Chapter 8

Conclusions

The primary focus of this thesis is the study of spin- $\frac{1}{2}$ fields coupled to gravity in spherical symmetry (Einstein-Dirac system). These systems have a rich phenomenology especially at the threshold of black hole formation.

The *massive* Einstein-Dirac system is investigated in Chapter 4. The spherically symmetric system of massive spin- $\frac{1}{2}$ fields is in a singlet spinor state and is shown to exhibit both unstable and stable solutions. The unstable solutions correspond to the threshold between black hole collapse and dispersal. There is a continuum of stable solutions that are solitonic in nature. These tended to oscillate and approach the stable, static solutions that we find through independent techniques.

In Chapter 5 we give a detailed study of the Einstein-*massless*-Dirac system. A spherically symmetric system is constructed from massless spin- $\frac{1}{2}$ fields (which are inherently *nonspherically* symmetric) by using spinor harmonics for their angular part and taking an incoherent sum of their individual stress tensors. The result is a spherically symmetric system with no net spin-angular momentum. Instead the system feels the effect of a “spin-angular momentum barrier.” In this case, black hole formation occurs at infinitesimal mass (Type II). This new, continuously self-similar solution is found by solving the Einstein-massless-Dirac system of nonlinear partial differential equations. A self-similar ansatz is then taken which reduces the partial differential equa-

tions to a set of ordinary differential equations. These new equations are solved and the two solutions are shown to be in very good agreement.

The strength of this barrier is controlled by the spin-angular momentum quantum number, l . The lowest value of $l = \frac{1}{2}$ corresponds to two counter-rotating shells, $l = \frac{3}{2}$ corresponds to four counter-rotating shells, etc. The Einstein-massless-Dirac system of PDEs is then solved for many values of l . As l is increased, the scaling exponent, λ for the Type II solutions is shown to decrease. The results suggest that there may in fact be a power-law scaling relationship for the individual scaling exponents as a function of l , but further study is required to ascertain this.

The final chapter describes a new two-dimensional, axisymmetric code which uses a combination of harmonic coordinates and Chebyshev pseudospectral collocation methods to solve Einstein's equations. This evolution code is a hybrid of finite-difference and spectral techniques—the temporal derivatives are approximated by finite-difference operators while the spatial derivatives are found using spectral methods. The constraint equations are solved using a purely spectral nonlinear elliptic solver which uses the Newton-Kantorovich method. Our constraint solver is successful in solving the Hamiltonian constraint at the initial time for our free evolution, but the evolution code is still unstable. We are continuing work on this and hope to have positive results shortly.

Appendix

Appendix A

Numerical Implementation

A.1 Computer implementation

We implemented the equations of motion discussed above in an RNPL (Rapid Numerical Prototyping Language) program, which generated FORTRAN 77 code to solve these equations. We also created FORTRAN “include” files to manually update and initialize the geometric variables.

The presentation of the numerical implementation given here is for the system described in Chapter 4. The other spherically symmetric systems contained in this thesis use different equations of motion but the general framework outlined below is the same.

A.1.1 Finite differences

To evolve the matter-field equations, we used iterative Crank-Nicholson (CN) differencing. This is an explicit update scheme which is second-order in both space and time. In this differencing scheme, the second-order time difference is centered about a virtual grid point, $t^{n+1/2}$, and the second-order spatial difference is also centered about $t^{n+1/2}$ via an averaging procedure.

Hence, our discrete form for the matter field evolution equations is

$$\begin{aligned}
\frac{(\widehat{\text{Re}}z_1)_j^{n+1} - (\widehat{\text{Re}}z_1)_j^n}{\Delta t} &= \frac{\hat{e}_j^{n+1} + \hat{e}_j^n}{2} \\
\frac{(\widehat{\text{Im}}z_1)_j^{n+1} - (\widehat{\text{Im}}z_1)_j^n}{\Delta t} &= \frac{\hat{f}_j^{n+1} + \hat{f}_j^n}{2} \\
\frac{(\widehat{\text{Re}}z_2)_j^{n+1} - (\widehat{\text{Re}}z_2)_j^n}{\Delta t} &= \frac{\hat{g}_j^{n+1} + \hat{g}_j^n}{2} \\
\frac{(\widehat{\text{Im}}z_2)_j^{n+1} - (\widehat{\text{Im}}z_2)_j^n}{\Delta t} &= \frac{\hat{h}_j^{n+1} + \hat{h}_j^n}{2},
\end{aligned} \tag{A.1}$$

where

$$\begin{aligned}
\hat{e}_j^n &\equiv \sqrt{\frac{\hat{\alpha}_j^n}{\hat{a}_j^n}} \left(\frac{1}{2\Delta r} \left(\sqrt{\frac{\hat{\alpha}_{j+1}^n}{\hat{a}_{j+1}^n}} (\text{Im}\hat{z}_2)_{j+1}^n - \sqrt{\frac{\hat{\alpha}_{j-1}^n}{\hat{a}_{j-1}^n}} (\text{Im}\hat{z}_2)_{j-1}^n \right) \right) \\
&\quad + \frac{\hat{\alpha}_j^n}{r_j} (\text{Im}\hat{z}_2)_j^n + m\hat{\alpha}_j^n (\text{Im}\hat{z}_1)_j^n \\
\hat{f}_j^n &\equiv -\sqrt{\frac{\hat{\alpha}_j^n}{\hat{a}_j^n}} \left(\frac{1}{2\Delta r} \left(\sqrt{\frac{\hat{\alpha}_{j+1}^n}{\hat{a}_{j+1}^n}} (\text{Re}\hat{z}_2)_{j+1}^n - \sqrt{\frac{\hat{\alpha}_{j-1}^n}{\hat{a}_{j-1}^n}} (\text{Re}\hat{z}_2)_{j-1}^n \right) \right) \\
&\quad - \frac{\hat{\alpha}_j^n}{r_j} (\text{Re}\hat{z}_2)_j^n - m\hat{\alpha}_j^n (\text{Re}\hat{z}_1)_j^n \\
\hat{g}_j^n &\equiv -\sqrt{\frac{\hat{\alpha}_j^n}{\hat{a}_j^n}} \left(\frac{1}{2\Delta r} \left(\sqrt{\frac{\hat{\alpha}_{j+1}^n}{\hat{a}_{j+1}^n}} (\text{Im}\hat{z}_1)_{j+1}^n - \sqrt{\frac{\hat{\alpha}_{j-1}^n}{\hat{a}_{j-1}^n}} (\text{Im}\hat{z}_1)_{j-1}^n \right) \right) \\
&\quad + \frac{\hat{\alpha}_j^n}{r_j} (\text{Im}\hat{z}_1)_j^n - m\hat{\alpha}_j^n (\text{Im}\hat{z}_2)_j^n \\
\hat{h}_j^n &\equiv \sqrt{\frac{\hat{\alpha}_j^n}{\hat{a}_j^n}} \left(\frac{1}{2\Delta r} \left(\sqrt{\frac{\hat{\alpha}_{j+1}^n}{\hat{a}_{j+1}^n}} (\text{Re}\hat{z}_1)_{j+1}^n - \sqrt{\frac{\hat{\alpha}_{j-1}^n}{\hat{a}_{j-1}^n}} (\text{Re}\hat{z}_1)_{j-1}^n \right) \right) \\
&\quad - \frac{\hat{\alpha}_j^n}{r_j} (\text{Re}\hat{z}_1)_j^n + m\hat{\alpha}_j^n (\text{Re}\hat{z}_2)_j^n
\end{aligned} \tag{A.2}$$

(Here, $(\hat{\text{Re}}z_1)_j^n$ is the finite-difference approximation for $\text{Re}z_1(r_j, t^n)$.) The boundary conditions applied to the matter variables z_b ($b = 1, 2$) are given by

$$\begin{aligned}
(\hat{z}_b)_1^{n+1} &= 0 \\
\frac{(\hat{z}_b)_{\text{NR}}^{n+1} - (\hat{z}_b)_{\text{NR}}^n}{\Delta t} + \frac{1}{2} &\left(\frac{3(\hat{z}_b)_{\text{NR}}^{n+1} - 4(\hat{z}_b)_{\text{NR}-1}^{n+1} + (\hat{z}_b)_{\text{NR}-2}^{n+1}}{2\Delta r} \right. \\
&\left. + \frac{3(\hat{z}_b)_{\text{NR}}^n - 4(\hat{z}_b)_{\text{NR}-1}^n + (\hat{z}_b)_{\text{NR}-2}^n}{2\Delta r} \right) = 0,
\end{aligned} \tag{A.3}$$

where $r_1 = 0$, and $r_{\text{NR}} = R$ is the maximum radius used in the simulation. Forcing the matter variables to zero at the inner boundary is a consequence of the regularity conditions (4.63). At the outer boundary, we have used second-order backward differences in space and a second-order time difference centered about $t^{n+1/2}$, again by averaging the spatial differences at the two time levels t^{n+1} and t^n .

The Hamiltonian constraint was applied by requiring that $\hat{a}_1^{n+1} = 1$, and repeatedly applying the constraint equation (4.26) and solving for \hat{a}_{j+1}^{n+1} using Newton's method. The derivative in r is implemented at each step using a second-order forward difference in r , centered at $r_{j+1/2}$. At the outer boundary, we apply the flat-space condition $\hat{\alpha}_{\text{NR}}^{n+1} = 1/\hat{a}_{\text{NR}}^{n+1}$. Then the slicing condition (4.30) is applied using a second-order backward difference in r , centered at $r_{j-1/2}$, and solved explicitly for $\hat{\alpha}_{j-1}^{n+1}$. Also, when solving these equations, we used the variable $A \equiv \ln a$ instead of a itself, to improve the accuracy of the simulation.

We also implemented Kreiss-Oliger dissipation in the code, where the

matter variables are subjected to the additional update

$$(\hat{z}_b)_j^{n+1} \equiv (\hat{z}_b)_j^{n+1} - \frac{\epsilon}{16} \left((\hat{z}_b)_{j+2}^{n-1} - 4(\hat{z}_b)_{j+1}^{n-1} + 6(\hat{z}_b)_j^{n-1} - 4(\hat{z}_b)_{j-1}^{n-1} + (\hat{z}_b)_{j-2}^{n-1} \right). \quad (\text{A.4})$$

This update is applied only for $3 < j < \text{NR} - 2$, and no dissipation is applied at or next to the boundaries. The parameter ϵ is set > 0 for dissipation and < 1 for stability. For the data that we present here, we typically used $\epsilon = 0.5$.

Bibliography

- [1] R. Bartnik and J. McKinnon. *Rev. Rev. Lett.*, 61:141, 1988.
- [2] M. Berger and J. Olinger. *J. Comp. Phys.*, 53:484, 1984.
- [3] N. D. Birrell and P. C. W. Davies. *Quantum Fields in Curved Space*. Cambridge University Press, 1982.
- [4] J. D. Bjorken and S. D. Drell. *Relativistic Quantum Mechanics*. McGraw-Hill, New York, 1964.
- [5] J. Boyd. *Chebyshev and Fourier Spectral Methods*. Springer Verlag, Berlin., 1989.
- [6] D. R. Brill and J. A. Wheeler. *Rev. Mod. Phys.*, 29:465–479, 1957.
- [7] J. A. Wheeler C. W. Misner, K. S. Thorne. *Gravitation*. W. H. Freeman, San Francisco, 1973.
- [8] M. W. Choptuik. *Phys. Rev. Lett.*, 70:9–12, 1993.
- [9] M. W. Choptuik. The 3+1 einstein equations, 1998.
- [10] M. W. Choptuik. Finite difference methods, 1998.
- [11] C. Canuto et al. *Spectral Methods in Fluid Dynamics*. Springer Verlag, New York., 1988.
- [12] F. Finster, J. Smoller, and S. Yau.

- [13] D. Garfinkle. *Phys. Rev. D.*, 65:044029, 2002.
- [14] J. N. Goldberg, A. J. MacFarlane, E. T. Newman, and F. Rohrlich. *J. Math. Phys.*, 8:2155–2161, 1967.
- [15] D. Gottlieb and S. Orszag. *Numerical Analysis of Spectral Methods: Theory and Applications*. SIAM, Philadelphia., 1977.
- [16] C. Gundlach. *Adv. Theor. Math. Phys.*, 2:1–49, 1998.
- [17] E. W. Hirschmann and D. M. Eardley. *Phys. Rev. D*, 51:4198–4207, 1995.
- [18] L. E. Kidder and L. S. Finn. Spectral methods for numerical relativity. the initial data problem. *Phys. Rev. D*, 62:084026, 2000.
- [19] H. Kreiss and J. Oliger. Methods for the approximate solution of time dependent problems. *Global Atmospheric Research Programme, Publications Series No. 10*, 51:4198–4207, 1973.
- [20] I. Olabarrieta and M. W. Choptuik. Critical phenomena at the threshold of black hole formation for collisionless matter in spherical symmetry. *Phys. Rev. D*, 65:024007, 2002.
- [21] R. Penrose and W. Rindler. *Spinors and Space-time*. Cambridge University Press, 1984.
- [22] C. W. Misner R. Arnowitt, S. Deser. *The Dynamics of General Relativity; Gravitation: An introduction to current research*. John Wiley, New York, 1962.
- [23] J. J. Sakurai. *Advanced Quantum Mechanics*. Addison-Wesley, 1967.

- [24] W. G. Unruh. personal communication.
- [25] W. G. Unruh. *Phys. Rev. D*, 10:3194–3204, 1974.
- [26] R. M. Wald. *General Relativity*. University of Chicago Press, 1984.
- [27] J. W. York. *Kinematics and Dynamics of General Relativity, (in Sources of Gravitational Radiation; ed. L. Smarr)*. Cambridge University Press, 1979.

Vita

Jason F. Ventrella was born in Tunkhannock, Pennsylvania on February 1, 1974, the son of John M. Ventrella and Judy A. Ventrella. He received the Bachelor of Science degree in Physics from the Massachusetts Institute of Technology in 1996. He applied to the University of Texas at Austin for enrollment in their physics program and was accepted. He started graduate studies in August, 1996. After graduation, Jason will continue a career in numerical relativity as a Postdoctoral Fellow at the Louisiana State University.

Permanent address: 1372 Ultramarine Lane
Punta Gorda, FL 33983

This dissertation was typeset with \LaTeX^\dagger by the author.

[†] \LaTeX is a document preparation system developed by Leslie Lamport as a special version of Donald Knuth's \TeX Program.